Propositions

1. In the age of omics, we need models to guide collection, curation and interpretation of experimental data.
   (this thesis)

2. The network motif approach is highly effective in gaining mechanistic understanding of complex genetic regulation.
   (this thesis)

3. The extension of biology from a field that focuses on natural organisms, to one that encompasses synthetic organisms will alter the way scientists address fundamental biological questions.

4. Most published research findings cannot be verified independently.

5. There is very little hope that humanity will respond effectively to the threat of global warming, mainly because global warming lacks features that the human brain has evolved to recognize and respond to as a threat.

6. Nuclear power is currently the only non-greenhouse gas emitting option for effective replacement of fossil fuels on a global scale.

Propositions belonging to the thesis, entitled:

'Modeling spatial pattern formation in Plant development'.

Milad Adibi
Wageningen, 12 September 2017.

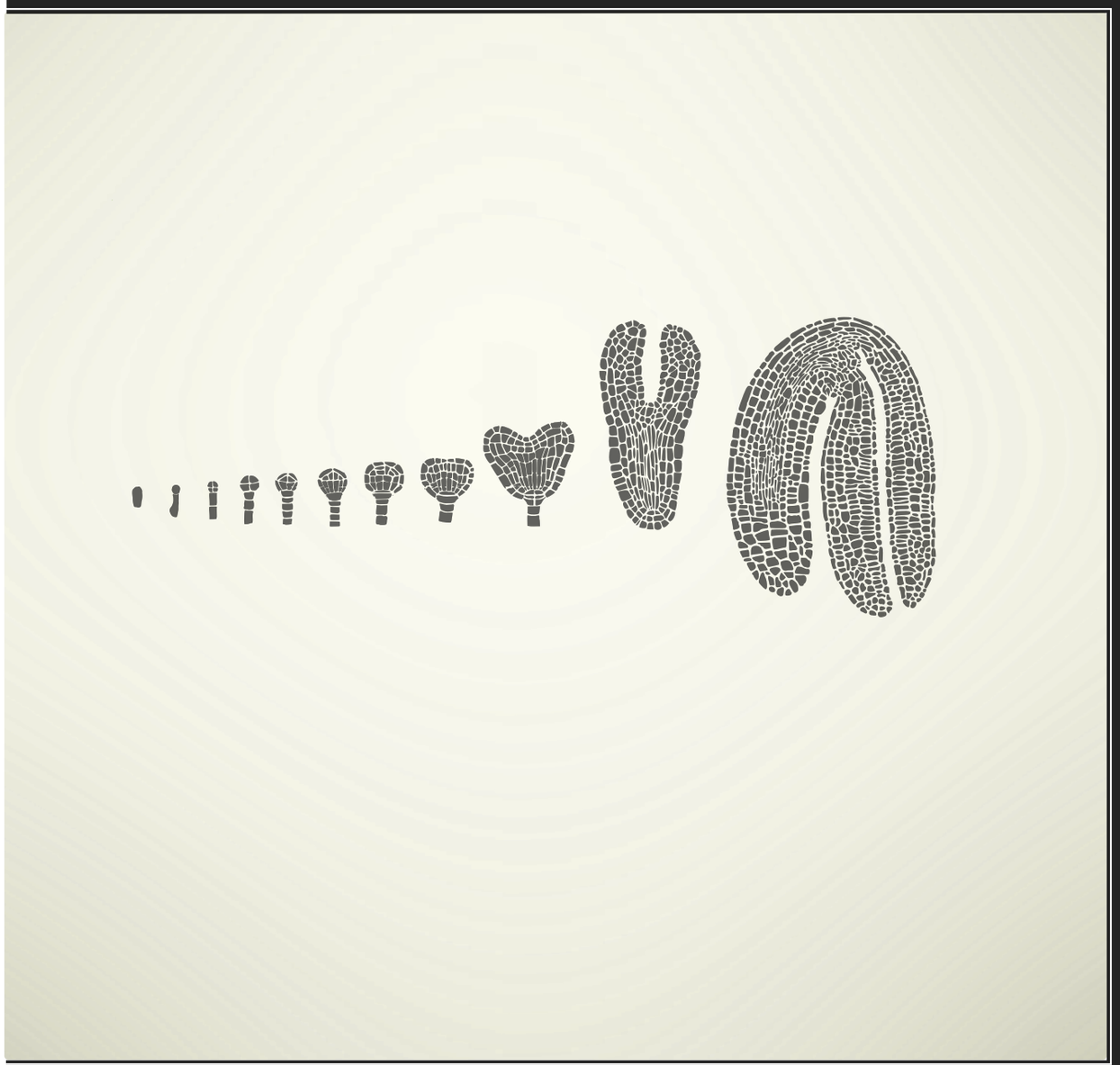

Modeling Spatial Patternformation in Plant Development Milad Adibi 2017

Modeling Spatial Pattern Formation in Plant Development

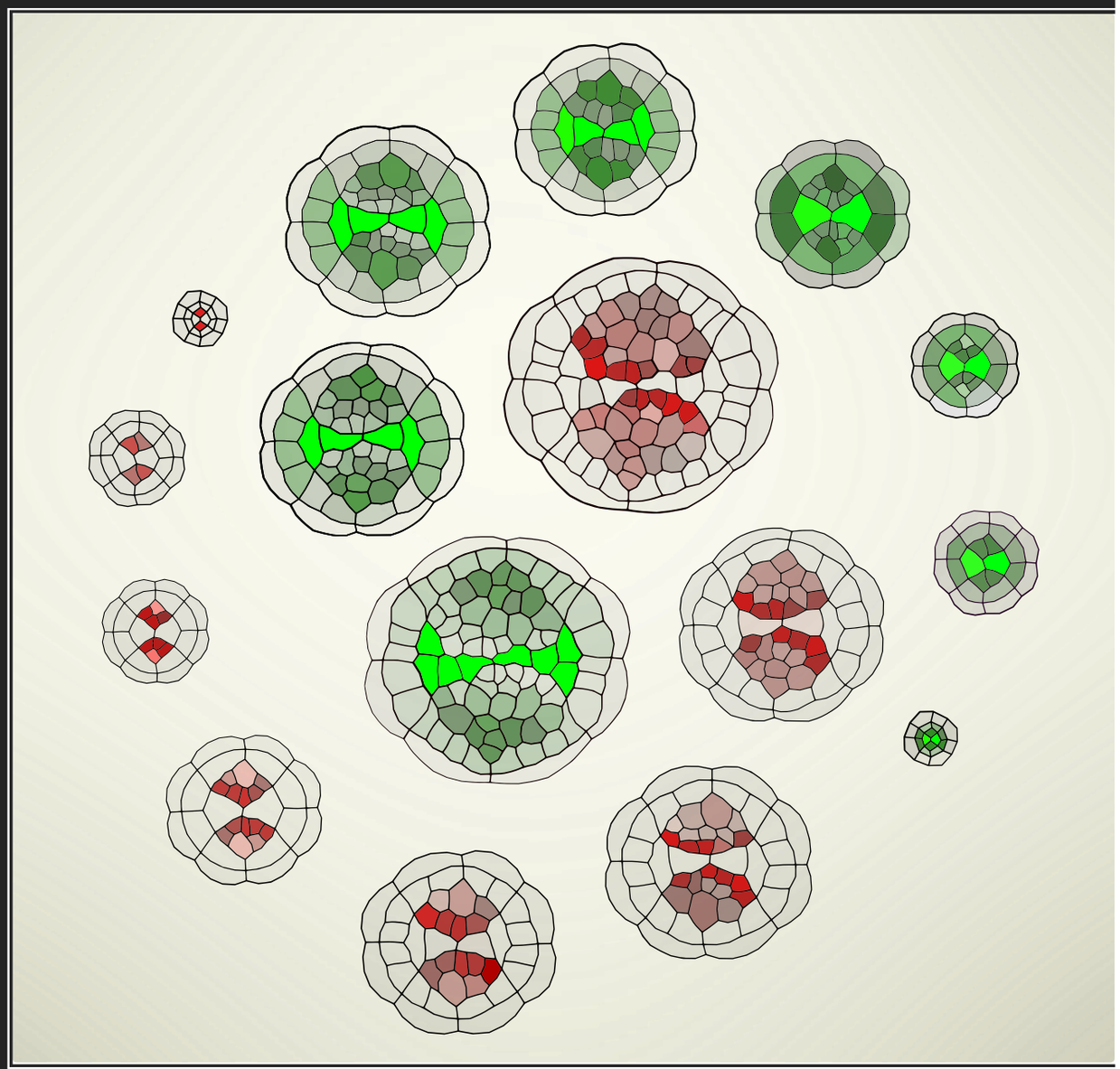

Milad Adibi

Modeling Spatial Pattern formation in Plant Development

Milad Adibi

Thesis committee

Promotor:
Prof. Dr Vitor dos Santos
Professor of Systems and Synthetic Biology
Wageningen University & Research

Co-promotors:
Dr. Christian Fleck
Associate Professor of Systems and Synthetic Biology
Wageningen University & Research

Prof. Dr Dolf Weijers
Professor of Biochemistry
Wageningen University & Research

Other members:
Prof. Dr Ben J.G. Scheres, Wageningen University & Research
Prof. Dr Roeland M.H. Merks, Leiden University
Prof. Dr Martin Hülskamp, University of Cologne, Germany
Prof. Dr Jaap Molenaar, Wageningen University & Research

This research was conducted under the auspices of the Graduate School of Experimental Plant Sciences

Modeling spatial pattern formation in plant development

Milad Adibi

Thesis
submitted in fulfilment of the requirements for the degree of doctor at
Wageningen University
by the authority of the Rector Magnificus
Prof. Dr A.P.J. Mol,
in the presence of the
Thesis Committee appointed by the Academic Board
to be defended in public
on September 12^{st} 2017 defense
at 11 a.m. in the Aula.

Milad Adibi
Modeling spatial pattern formation in plant development
190 pages.

PhD thesis, Wageningen University, Wageningen, NL (2017)
With references, with summary in English

ISBN 9789462956896
DOI: https://doi.org/10.18174/421015

Contents

Summary

Modern biological research is accumulating an ever-increasing amount of information on genes and their functions. It is apparent that biological functions can very rarely be attributed to a single genes, but rather arise from complex interaction within networks that comprise many genes. A fundamentally important challenge in contemporary biology is to extract mechanistic understanding about the complex behavior of genetic networks from the available data. The interactions within a genetic network are often exceedingly complex and no-linear in nature, and thus are not open to intuitive understanding. This situation has given rise to a host of mathematical and computational approaches aimed at in-depth analysis of genetic network topologies and dynamics. In particular these approaches focus on system level proprieties of these networks, not directly derivable from their constituent components. To a large extent the power of these theoretical approaches rely on meaningful reduction in complexity by utilizing justified simplifications and abstractions. The underlying principle is that in order to comprehend a mechanism, it is not necessary to take into account all the available information about the mechanism. Given this, Computational models that follow this approach focus on incorporating core components that are essential in answering a specific biological question, while simplifying/omitting the less relevant processes. A fundamental question is this regard is what simplifying concept should be employed when developing a theoretical model of a genetic network.

A successful approach to address this question is the notion of network motif analysis. This approach is based on the core idea that most genetic networks are not arbitrary nor unique, instead they can be categorized into common network dynamics and topologies that perform core functions. Analogous to components of an electric circuit (resistors, capacitor, etc) these network motifs have distinct properties that are independent of the network that they are embedded in. Therefore analysis of genetic networks in terms of their constituent motifs can potentially be an effective mean in obtaining mechanistic understanding about them.

In this thesis the network motif approach is utilized to study two instances of pattern formation in plant tissues. The first study focuses on organization of stem cells within the shoot

apical meristem of the model plant, *Arabidopsis thaliana*. The results demonstrate that three interconnected network motifs can account for a range of experimental observations regarding this system. Furthermore through an exhaustive exploration of the available data, candidate genes and interactions corresponding to these motifs are outlined, thus paving the way for future interdisciplinary investigations.

The second study explores the development of vasculature during arabidopsis embryogenesis. In contrast to shoot apical mersitem in mature plant, the cell number and arrangement of vasculature in highly dynamic during its embryonic development. To account for this feature,a computational framework was utilized that is capable of capturing the interplay between genes and cell growth and division. The outcome revealed that two interlocking networks motifs dynamically control both patterning and growth of the vascular tissue. The study revealed novel spatial features of a motif previously studies exclusively in non-spatial settings. Furthermore the study resulted in a compelling example of model-driven discovery, where theoretical analysis predicted a specific cellular arrangement to be crucial for the correct development of vasculature. Subsequent analysis of experimental data confirmed the existence of this cellular arrangement in the embryo.

the projects presented in this thesis exemplify successful applications of the network motif approach in studying spatial genetic network. In both cases the networks were successfully examined in terms of their constituent motifs, which subsequently lead to increased mechanistic understanding of them. Ultimately the work presented in this thesis demonstrates the effectiveness of studying genetic networks by a combination of careful examination of available biological data and a reductionist modeling approach guided by the concept of network motifs.

CHAPTER 1

Introduction and thesis outline

1.1 Computational modeling and developmental biology

Plat organs such as root and shoot develop via generation and regulation of spatio-temporal patterns that regulate cellular behavior. Understanding how such patterns arise is a key aim in developmental biology and is the focus of a substantial body of theoretical and experimental research. Despite our increasing knowledge of genetic networks, genetics alone does not lead to a mechanistic understating of regulatory networks that establish and regulate these patterns. This is because genetic and functional genomics approaches often assume a direct relationship between genes and morphology at the tissue or organism level. To understand the developmental function of genes [1], one must take into account their spatial patterns and roles within genetic networks. Furthermore these networks interact with mechanical and geometrical processes, often in complex and non-linear manners [2]. Natural intuition is not sufficient for understanding this level of complexity. Mathematical modeling has proven to be an effective tool in providing insights into the dynamic and complex mechanisms of development.

1.2 Models of biological pattern formation

Mechanisms of pattern formation in developmental biology can be categorized into *pre-pattern* and *emergent pattern* models. In the former group initial biases in cellular properties and/or morphogen concentrations drive formation of new patterns. In contrast in the latter group patterns spontaneously emerge from spatially homogeneous initial states. Many models of biological pattern formation employ mechanisms from both of these groups.

The emergent pattern models are concerned with a defining feature of multi-celluar organisms, the ability to create spatial patterns from a previously non-patterned state. To date, only a handful of mechanisms have been identified that can account for such spontaneous pattern formation. The most prominent among these is the mechanism put forward by Turing [3], he proposed a set of reactions between two diffusing chemicals that result in development

of spatially heterogeneous distributions, from an initially near-homogeneous state. Turing's reaction-diffusion (RD) model has intrigued researchers since its introduction, as it provides a clear explanation for how spatial patterns can be encoded in chemicals interactions. A growing body of observed patterns both in plants and animals can be successfully reproduced using Turing's model. However a persistent challenge has been to experimentally prove the existence of this patterning mechanism in biology. Another prime example of a successful group of models of emergent patterning comes from the field of plant development. These models are focused on interactions between plant hormone Auxin and its membrane-bound transporters, PIN FORMED (PIN) proteins [4]. In these models feedback from auxin on PIN induces a polar localization of PIN at cell membranes. The result is a variety of heterogeneous spatial patterns of auxin distribution [5]. Some of these models predate the discovery of PINs and provide an excellent example of how modeling can provide insight and direct experimental research. Several groups of auxin-PIN models exist where each group is capable of reproducing specific observed patterns of auxin distribution [5–7]. As with the Turing model, these mechanisms have not been conclusively shown to exist in plants. Some of the existing models propose divergent mechanisms of PIN regulation via auxin and to date have not resulted in formulation of a unified model which account for all observed auxin patterns.

Models based on above mentioned mechanisms are powerful tools that can explain patterning behaviors of plants even when precise quantitative information is unavailable. Intriguingly these models and all their variants share a same basis: local self-enhancement and long range inhibition. A large and increasing body of observed pattern in plant development can be reproduced by this simple concept.

1.2.1 State-of-the-art models of plant development

Feedback from mechanics and geometry on genes is a crucial component of many developmental systems. Most developmental processes occur within the dynamic template of a developing

tissue or organ, where morphogens affect cell mechanics that in turn feedback on morphogen patterns. As a result many developmental processes cannot be adequately studied without taking this feedback into account. This has led to development of modeling frameworks where chemical signaling networks can be implemented within a dynamic template of cells. These software allows for cellular behavior such as division and growth as well as mechanical properties, to be regulated by morphogen concentrations [8–10]. In recent years these approaches have been effective in advancing our mechanistic understanding of dynamic developemntal processes. These dynamic models represent the state of the art in modeling spatial pattern formation in biology. An increasing variety of models and platforms have been developed aimed at addressing questions in a wide range of fields in developmental biology. The use of a modeling platform rarely goes beyond the research group were it is developed. This complicates contrasting and comparison between different models, even when they aim at answering the same scientific question. With the increasing presence of computational modeling in developmental biology, it is important to develop approaches that facilitate communication in the field.

1.2.2 Current challenges and outlook

The above touches upon some of the main advances and challenges in studying pattern formation in plants. Several well developed theoretical models exist that successfully reproduce a wide range of observed pattern. In most cases, notably the Turing RD model, it has been challenging to relate these models to the available experimental data. This situation restricts the possibility of forming a functional iterative process between theory and experimentation. Therefore it is apparent that there is much to be gained from rigorous interdisciplinary efforts aimed at bridging the gap between experimental and theoretical research in these areas.

Computational modeling of cellular development is advancing rapidly. We are now capable of developing 3D final element models of growing and dividing cells with sub-cellular level implementation of chemical processes. Such approaches employ physical and chemical formulations,

algorithms and assumptions to represent developing biological systems. Unlike experimental biology, no commonly used protocols have been developed for scientific presentation of these models and to facilitate reproducibility of modeling results. This is in part because computational modeling is a relatively new field and by its nature gives rise to diverse and sometimes divergent approaches. As such I think the field can benefit from clear presentation of computational models that provide all information required for thorough understanding and reproduction of modeling results. This is especially important for analysis and development of models by other researchers, since due to the often non-linear nature of these models, the impact of different factors on model functionality is not always readily discernible. As such to understand and assess these models one requires a thorough and detailed description of its components, assumptions, initial conditions etc. Ultimately research in the field can benefit considerably by focusing on development of open-source platforms for modeling. These allow for development of wide array of models, while providing a common base that greatly promote communication and interaction among computational modelers.

1.3 Thesis outline

The **first chapter** of this thesis provides an overview of the current state of spatial patterning models in plant biology. In doing so this chapter also outlines the overall approach to modeling that is applied in the subsequent chapters. Furthermore the chapter includes an overview of the experimental data relevant to work presented in this thesis. Each of the subsequent chapters of this thesis presents a computational modeling effort aimed at answering a specific question in plant developmental biology. For each project my aim was to form an iterative process between modeling and experimentation. Ultimately the goal was not only to explain developmental phenomena but also to provide useful guidelines for future research in the field. As such models were developed in close collaboration with experimental biologists, with a focus on providing predictions that were practical to test experimentally. For each model, I explicitly catalog the

biological facts and assumptions underlying the model and provide a detailed mathematical and computational description, to aid understanding, reproduction and further development of these models.

In **chapter two**, I explore how a genetic network that includes a Turing reaction-diffusion motif, can account for the stem cell organization in *Arabidopsis* shoot apical meristem. Using reaction-diffusion models to account for spatial patterning of shoot apical meristem has a history of more than a decade and several distinct modeling approaches have developed. While providing valuable insight into SAM patterning, these efforts did little to direct experimental research towards identification of genetic players that correspond to components of an reaction-diffusion system. As discussed earlier, this mirrors the situation of almost every modeling effort that employs a Turing reaction-diffusion system, especially in plant developmental biology. My modeling effort aimed at utilizing the available data to identify the potential *in vivo* manifestation of a Turing RD system within the meristem genetic regulatory networks. In close collaboration with experimental biologists, I focused on providing testable prediction, and when possible to devise and perform experiments in that regard.

The project introduced in **chapter three** focuses on studying the development of vascular tissue during early arabidopsis embryogenesis. This developmental system provides an outstanding opportunity for studying cellular level patterning; after a few round of cell division a single cell develops into the basic body shape of a plant, comprised of only a handful of cells. This minimal setting has the potential to uncover core spatial signaling mechanisms that drive plant development. Unlike meristem, embryonic development involves major changes in cell numbers and morphology. To capture the interplay between division, growth and spatial genetic signaling, I used VirtualLeaf. This software modeling platform provides a mean to study genetic networks in the context of the biophysics of growth and patterning. Virtualleaf is computationally efficient and well suited for testing hypothesis via model simulations. Using this software I could avoid substantial investment in time and resources required for in-house development of an equivalent software. This allowed us to focus on hypothesis generation and model analysis. The model in

this chapter adopts a variant of a established auxin-pin model and explores its role in patterning the emerging vasculature. The results in this chapter provide insights into how plant hormones interact to regulate growth, and how the feedback from the emergent tissue architecture impacts development.

Development of vasculature has recently received significant attention from the modeling community. Apart from the work presented in chapter three, it has been the subject of two other modeling projects. Important differences exist between these models, including their scope, modeling platform, template, assumptions and their conclusions. As a result, assessing the overall contribution of these modeling efforts to the field was rather challenging. For the most part this was because, especially to non-modeler members of the research community, there appeared to be three divergent and competing hypotheses driven by each of the computational effort. **Chapter four** presents the result of a collaboration between me and researchers from the other modeling teams, aimed at finding a common ground,to compare and contrast the models and their findings. This collaboration was aimed at drawing biologically meaningful conclusions, by finding the common denominator between models and pointing out the fundamental differences. Ultimately we aimed to highlight experimental inquiries with the most potential to advance our understanding of plant vascular development.

CHAPTER 2

A review of spatial modeling in plant organ and tissue development

2.1 Systems biology and tissue-level modeling

Recent advances in molecular biology have generated a tremendous amount of information about cellular processes and their functions. With the emergence of modern genomics, entire genomes of an increasing number of organisms have been sequenced, and a growing number of these genes have known functions. In the coming years we can expect the assignment and verification of the functions of the majority of genes from the genomes of model organisms [11]. Much less is known about the properties of regulatory networks that the individual genes and interactions are parts of. Understanding the behavior of these networks is a necessity in studying complex cellular processes such as cell growth and division [12]. This has led to the recent interest in the concept of 'emergent' behavior. Simply put, emergence in the context of complex systems means that the properties of the system are not equal to the sum of properties of the components, these properties cannot be predicted even with a full knowledge of the components. In other words, system level properties are not derivable from the properties of constituent parts, but arises from the interlinked, nonlinear and dynamic relationship between its components. Consequently studying such properties involves application of holistic approaches as opposed to the classical reductionist approach that has dominated modern science since its beginning [13–15]. The following quote adequately highlights this distinction:

> "The reductionist approach has successfully identified most of the components and many of the interactions but, unfortunately, offers no convincing concepts or methods to understand how system properties emerge...the pluralism of causes and effects in biological networks is better addressed by observing, through quantitative measures, multiple components simultaneously and by rigorous data integration with mathematical models [16]."

Mathematical models with explicitly defined interactions are effective tools in analysis of systemic behavior of complex developmental mechanisms in biology. Such models provide a powerful and inexpensive tool for *in silico* testing of new hypotheses as well as discriminating among alternative hypotheses. These systems biology approaches transform the classical box and arrow network descriptions into explicit and informative network models [11,17,18]. A large

portion of system biology focuses on dynamics inside single cells. Mathematical formulations of single cell networks do not take into account any spatial component. Arguably, the spatial properties of a single cell can have an effect on the chemical processes occurring inside the cell, nevertheless majority of gene/protein interactions within a cell can be approximated, to a reasonable accuracy, without considering the spatial aspects [19, 20].

With a few exceptions, all cells within a multi-cellular organism have the same genetic code. As such, Spatiotemporal variations in gene expression play a critical role in the generation and diversification of cell types and development of organs and tissues. These variations are often regulated by dynamic and complex interplay between spatial gene expression domains. Consequently many important developmental processes in multi-cellular organisms cannot be studied without taking into account the spatial medium within which genes and proteins interact. Embryonic development, disease progression, tumour progression and tissue regeneration are among key events that manifest at the tissue and organ level and cannot be adequately studied at the level of single cells. Therefore it is important to develop systems biology approaches that take into account the multicellular context in which cell exist and function [21, 22].

Organ and tissue level modeling is an relatively new field that aims to integrate intracellular and intercellular interactions within the mechanical and geometrical context of tissue and organs. Recently, computational models of multicellular systems have been successfully utilized in a wide range of fields in both animal and plant studies [23–25].

2.1.1 The reductionist approach in modeling

The reductionist approach in the context of computational biology is not equivalent or analogous to the classical reductionism in biological research discussed above. The underlying philosophy is that a model is constructed to answer a specific biological question. As such, it should only contain components which are highly relevant in addressing the question in hand, i.e. the model should be as simple as possible and not aim at incorporating all the information

available about the system under study. This is in contrast to all-encompassing approaches such as whole-genome metabolic networks that take into account all available data about the network. For example the production of a protein from its encoding gene principally involves promoter binding, transcription, translation and post transnational modifications. In a model where the focus is on cell signaling via molecules that are exchanged between cells, the intricate details of the intracellular process of protein productions can be summed up by assuming the production rate of the protein is directly dependent on the concentration of the promoter. At the same time the intercellular process of protein transport can be captured in detail by taking into account diffusion and active transport via various influx and efflux carriers. As such, the 'scope' of the model would be set appropriately to address the biological question.

Keeping a model as simple as possible greatly aids with analysis and understanding. In addition, even with simple networks with spatial components, the computational expenses can be significantly high. Therefore the development, implementation and simulation of a spatial model can be greatly aided by simplification.

2.1.2 Biological network motifs

For the most part, the behavior of cellular networks, possesses a complex and unintuitive nature which is not easy to understand and analyze. A successful theoretical approach that has emerged to address this problem is to view biological networks as an interconnected system of network motifs. The available data suggests that biological networks are constructed in a similar manner to electrical circuits: while they are extremely diverse, they are made up of a limited number of subunits. [1, 26]. A These small and recurring functional subunit of a biological network are called biological network motifs. Some network motifs are identified using their recurring feature: biological networks are compared to randomized networks with the same number of edges and nodes. The basic concept is that if a pattern occurs significantly more in real networks compared to randomized ones, then it must have been selected because of an advantage that it

confers to the organism. In absence of such an advantage the motif is expected to occur at a similar rate in randomized networks and the real networks [27].

These building blocks, perform information processing functions that are independent from the network that they are embedded in. Studying biological network motifs is akin to attempting to understand an electrical circuit by studying its constituent subunits: resistors, capacitors etc. While such functional subunits are a feature of man-made circuits, there is an increasing body of evidence that shows the concept is useful when utilized to dissect genetic networks [1, 26]. Once motifs have been identified in a network, the behavior of the network as a whole can then be analyzed in terms of relationship between these subunits [27]. This approach holds a great potential to improve our understanding of network functionality, evolution and dynamic behavior. Analogous to electronic components, networks motifs are not specific to a network or a developmental context but are universal components of genetic regulation. Thus, studying these motifs provides insight beyond their role in a particular biological process. In this section we will review two classes of network motifs that feature prominently in computational models of plant development in general, and in this thesis specifically.

2.1.3 Self-organized motifs in patterning

Development can be seen as progression of patterns, where new structures develop on the ground of previously established patterns. When the result of this progression is a simple linear mapping of the previous patterns, it can be said that intrinsically, new patterns have not been established. In contrast when a developmental process involves the establishment of complex patterns from a state of lesser complexity, via internal interactions, the process is said to exhibit self-organized patterning [28]. This complexity is an emergent property of the system of interactions and not determined by external influence. While development of many patterns in biology can be understood as propagation and manipulation of pre-existing patterns, some core patterns must be generated spontaneously in biological systems via cellular networks. Such self-organizing patter

formation is a fascinating feature of development because it mean that spatial patterns of organs and tissues are encoded in chemical interactions between genes and proteins. Self-organizing patterning models are among the earliest and most successful computational models on origins of biological form [28, 29].

Reaction Diffusion systems

Alan Turing's Reaction-Diffusion (RD) model is a seminal example of a self-organized patterning motif. In 1952 Turing published his landmark paper, 'The chemical basis of morphogenesis' [3]. The paper proposed that patterns seen during the development of multi-cellular organisms can arise from the pattern of underlying chemicals, which he termed morphogens. In this theory the spatial pattern of chemicals leads to cellular differentiation in a concentration dependent manner. Turing considered a system of two diffusing interacting morphogenes. Assuming that in absence of diffusion the system reaches a stable steady-state resistant to homogeneous perturbations. He showed mathematically that for a specific type of interactions, the system is turned unstable via diffusion. This can lead to the amplification of initial spatial perturbations into a periodic heterogeneous steady state. [3]. Thus the system can be said to self-organize; regular spatial patterns can arise from small initial perturbations in an otherwise homogeneous state. Hence he demonstrated, for the first time, how spatial non-uniformity may arise naturally out of a homogeneous, uniform state. This is an striking outcome, since it shows that diffusion, generally regarded as a stabilizing process, results in instability.

Mathematically, RD systems take the form of semi-linear parabolic partial differential equations. In its basic form a RD system can be written as following.

$$\begin{aligned} \frac{\partial \vec{A}}{\partial t} &= D_A \vec{A} \nabla^2 + F(A) \\ \frac{\partial \vec{B}}{\partial t} &= D_B \vec{B} \nabla^2 + G(B) \end{aligned} \tag{2.1}$$

$\vec{A}$ and $\vec{B}$ are concentrations of the two morphogens, D_A and D_B are matrices of diffusion constants and $F(A)$ and $G(B)$ describe the reaction kinetics. The conditions under which such a system can produce a pattern, can be mathematically driven. Therefore RD systems have been subject of detailed mathematical studies and various extension of the basic system exist. RD systems produce a wide array of solutions, including the formation of wave fronts and wave-like phenomena, space-dependent stationary solutions, such as spots, stripes, hexagons and more intricate structure like dissipative solitons [30].

Initially RD systems did not attract much attention. The invariability of output for a given set of parameters was found at odds with developmental processes that adjust in response to intrinsic and extrinsic perturbations. The early analysis of reaction-diffusion systems determined that they are too sensitive to initial conditions and noise. As Turing himself admitted, the chemical reactions he proposed in his model were uninformative and strange [31]. RD systems did not attract much attention as a biological patterning mechanism until more feasible formulations emerged.

Gierer-Meinhardt Model

In 1972, Alfred Gierer and Hans Meinhardt revived the concept of RD by coherent extension of its terminology and by carefully studying its implication and variations [32]. They demonstrated that pattern regulation can be achieved via manipulations of interaction rates of a morphogen. In addition, Gierer and Meinhardt put forward a biochemically plausible realization of a reaction-diffusion system, see Fig. 2.1.A [26]. The Gierer-Meinhardt system also termed activator-inhibitor system, produces patterns where the activator and the inhibitor have overlapping extrema, i.e. the two waves are in phase, as shown in Fig. 2.1.B.

Since the initial publication by Gierer and Meinhardt, their formulation of a Turing system has attracted considerable attention as a core mechanisms for pattern formation in biology. To

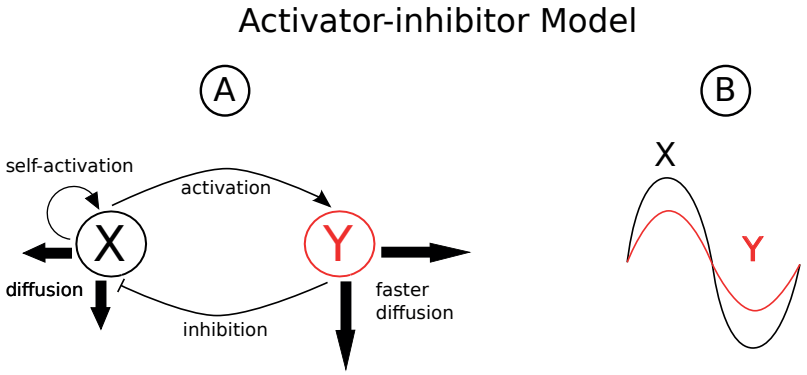

Figure 2.1: Activator inhibitor model Schematic representation of Geier-Meinhardt model, a combination of local self-activation and long distance inhibition produces overlapping peaks of concentration (B).

this date, reaction diffusion systems remain as one of the few models in developmental biology that account for spontaneous formation of pattern. RD models are utilized to explain various patterns, from animal coat patterns [33] to trichome distribution in plant leaves [34].

While RD systems reproduce many biological patterns, the biological proof that such patterns are produced via a biological RD system is largely lacking. Only recently publications have emerged where strong candidates for the activator, the inhibitor and the necessary network interactions have been identified [35], [36]. For a given system of reaction diffusion, there are often multiple stable solution; Small variations in initial conditions can lead to formation of different patterns. Moreover, for a typical system, the subset of parameters that satisfy conditions in (2.1) is small and hence the patterning capability of the model depends on precise parametrization. Small deviation in parameters can lead to the loss of pattern, thus the system can be non-robust to perturbations. Another issue is that the resulting patterns are scale dependent. This is in contrast to the 'scale-invariance' that many biological patterning systems posses. However certain variants of the Turing's model do not suffer from this limitation [37, 38].

Many decades have passed since the introduction of Turing's model and it has been the subject of ever-increasing interest from theoretical biologists. New variations of Turing's model are

regularly published, while these models reproduce many biological patterns. Only recently publications have emerged where both the activator and the inhibitor along with the necessary interaction have been identified [35], [36]. In [35], a variant of activator-inhibitor model is implemented in a growing domain, in combination with other gradient-based morphogens. The resulting model, reproduces digit patterning in wildtype and various non-wildtype settings. Moreover the work provides some of the most convincing experimental evidence for the existence of reaction-diffusion system in biology. The work suggests that the biological manifestation of RD systems often does not correspond to the minimal theoretical definition of these systems, and that they function in conjunction with other spatial network motifs. This work highlights the effectiveness of interdisciplinary approaches that combines theoretical analysis with careful probing and examination of the available data.

Polar Auxin transport models

Models concerned with transport of plant hormone Auxin are another successful group of models that spontaneously generate spatial patterns. Auxin is the most well studied plant hormone and is involved in many aspects of plant growth and development. auxin functions as the coordinator of development; it is synthesized in specific sites in the plant and transported to target tissues where is initiates a signaling pathway resulting in developmental responses [39]. Hence the spatiotemporal patterns of auxin distribution are strictly regulated [5]. Unlike other plant hormones auxin is actively and directionally transported (active transport is speculated for other plant hormones but has not been experimentally established yet). In general auxin concentration is not determined by local synthesis and degradation but rather the long distance transport and accumulation of auxin [40].

Several influx and efflux carriers of auxin have been identified. AUXIN-RESISTANT1 (AUX1) localizes to the plasma membrane and has been shown to function as an auxin influx carrier. With some notable exceptions AUX1 shows uniform localization to plasma membranes of

cell [41,42]. Furthermore its localization is not affected by local auxin distribution and flux [42]. Evidence points towards the role of Aux1 as a general facilitator of auxin movement that does not play a significant role in establishment of polar auxin transport (PAT) [43].

Members of the PIN-FORMED (PIN) family of proteins are an important group of auxin efflux carriers. In contrast to Aux1, most family members exhibit strong polar localization at the plasma membrane and are known to strongly regulate the long distance transport of auxin as well as establishment of peaks of auxin concentration [4, 5]. PIN proteins continuously cycle between endosomes and plasma membrane. Auxin has been shown to affect PIN levels at the plasma membrane by inhibiting the internalization of PIN in the endosomes [44, 45]. The constant shuttling of PINs and the feedback loops between PINs and auxin constitute an exceptionally dynamic mechanism of PIN localization capable of rapid redirection of auxin flow and re-positioning of auxin peaks. These aspects of auxin transport are associated with important developmental stages as well as responses to environmental changes [46].

An interesting feature of PAT is that the polarity of PINs with regard to auxin distribution varies among the members of the family. In general, PIN polarity comes in two from; PIN localization pointing toward a maxima of auxin concentration, e.g. in epidermal layer of shoot meristem PIN localization points towards the auxin maxima that mark the incipient primordia [5,47]. Another instance of PIN localization comes in the form of canalization; long distance orientation of PINs away from a maxima of auxin concentration, as seen in inner cell layers below incipient primordia, where auxin forms strands radiating away from the auxin maxima [5]. With such intriguing features in mind, and the difficulty of measuring auxin concentration qualitatively, computational modeling has emerged as a useful approach to formulate and test hypothesis regarding the inner-working of auxin transport. PAT has been the subject of various modeling approaches even before the discovery of PINs [7,48].

Despite the recent advances made in understanding of the inner workings of PAT, a comprehensive mechanistic understanding of cellular perception of auxin and subsequent PIN regulation is currently lacking [5, 49]. As a result, the existing models of PAT focus on

reproducing the experimental observations, combining aspects of the current knowledge with assumptions regarding the feedback mechanism to reproduce auxin and PIN distributions in different tissues [5]. PAT models can generally be divided into two groups, concentration-based and fluxed-based models:

Flux-based models: Early models by Mitchison are based on Sach's canalization hypothesis; auxin flux within a cell increases the capacity of the cell to transport auxin in the direction of the flux [7]. In early model this effect was represented by increase in membrane permeability in the direction of the flux. Later models ([6, 50]) and later by PIN levels at the plasma membrane. These models can reproduce various auxin canalization pattern and typically require an auxin source and a sink for canalization to occur. Various models of this group can produce results consistent with observations of vein formation in developing leaves. Two mechanisms have been postulated for the flux-based feedback; enhanced polar transport and diffusion. The first hypothesis suggests enhanced PIN localization in the direction of flux, while the second is based on enhanced diffusion irrespective of flux direction. Currently conclusive experimental evidence for both scenarios is lacking.

Up the gradient models: These models are build around the hypothesis that the amount of PIN on a membrane is proportional to the auxin level in the neighboring cell facing that membrane. Up the gradient models are commonly utilized to study developmental processes involving the formation of auxin maxima, namely phyllotaxis [51, 52]. This is achieved by amplification of differences in auxin concentration and the formation of periodic auxin maxima. These models require non-linear dependency of wall PIN levels on the concentration of auxin in adjacent cells (Smith *et al* used an exponential relation and Joensson *et al* employed one based on a hill function). In both cases the models are capable of producing approximately equidistant peaks.

The temporal and spatial dynamics of PAT via PINs exemplify non-linear processes that are too complex to be studied via classical biological approaches alone. Despite this, PAT remains

as a major focal point in studying plant development. This is to a large part due to theoretical studies of PAT, that are a prime example of the contribution that computational and mathematical approaches can make in biological studies. Mathematical models of PAT predate and anticipated the discovery of PIN proteins and can reproduce variety of observed PIN and auxin patterns. While concrete biological evidence for computational PAT models is lacking, these models have been instrumental in understanding the possible mechanisms of PIN-auxin interactions. Nevertheless, a major challenge in computational modeling of PAT is to capture the two major PAT processes: maxima formation and canalization, with a unified PAT model. Despite some efforts [53] a unified model of PAT that can reproduce the relevant biological observations has not been put forward.

2.1.4 Feed-forward loop network motif

Arguably one of the most significant and well-studied genetic network motif is the feedforward loop (FFL). This motif has been shown to be the most widely occurring genetic network motif in yeast and E.coli [27]. The motif is comprised of three genes, where one gene regulates another, both directly and via a third intermediate, as shown in Fig. 2.2. Thus a FFL loop comprises three interaction, each of which can be positive (activation) or negative (inhibition). These give rise to eight possible FFL configuration, see Fig. 2.2. Coherent FFLs are the four configuration in which the direct and indirect interactions have the same sign, as shown in Fig. 2.2.A, the incoherent group (IFFL) comprises the other four in which the two interactions have opposite signs, Fig. 2.2.B. The type 1 coherent FFLs are the most common in real networks [27].

The properties of various types of FFLs have been determined using mathematical analyses based on deterministic rate equation approach [27]. Studies of FFls focus on their role as temporal signal processors, in non-spatial settings. Coherent FFLs are shown to function as sign sensitive delay elements in signal processing; sign sensitive delay means the response time to step-like stimuli is asymmetric. The response time is rapid in one direction (ON to

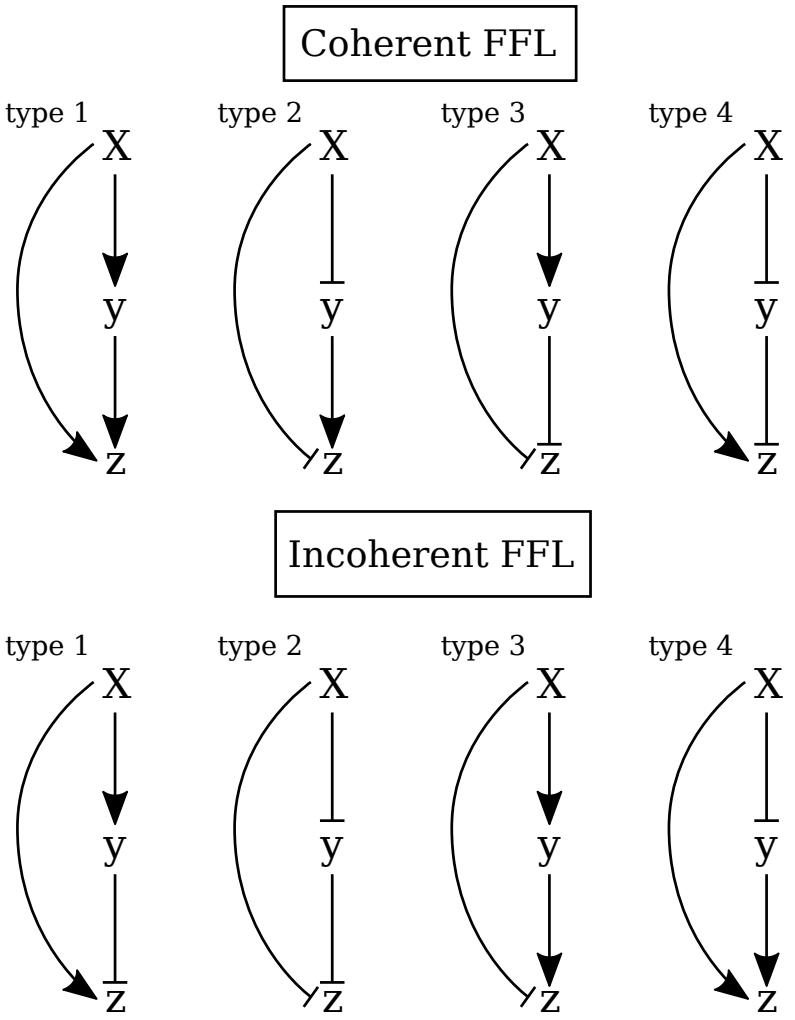

Figure 2.2: FFL network motif. There are eight different types of FFLs which are subdivided into coherent and incoherent FFLs. In coherent FFLs the direct and indirect regulation of z by x are of the same nature (activation or inhibition), while in incoherent FFLs these regulation are of opposite nature.

OFF) and delayed in the other (OFF to ON) [54]. Consequently when X is transiently activated, activation of z is minimal. Activation of z only occurs when x is activated for a sufficiently long time. Once x is deactivated, z expression is rapidly turned off, Fig. 2.2. In this capacity coherent FFLs act as noise buffers, filtering out transient fluctuations of the input signal. This is thought to be the reason that type-1 coherent FFLs are the most common type of FFLs in genetic

networks. The role of coherent FFLs as sign-sensitive delay elements has been experimentally confirmed [54]. The incoherent FFLs exhibit several interesting properties among which are: acting as sign-sensitive accelerators that speed up signal in one direction (OFF to ON) [55], fold-change detection in gene regulation [56], and generation of non-monotonic input functions for genes [57].

FFLs studies serve as an excellent example of network motif approach in studying biological networks. It shows how network motifs can be detected, studied and understood as independent signal processing units embedded within genetic networks. An important aspect of the research concerning FFLs in genetic networks is its interdisciplinary nature. Theoretical studies of FFLs are almost always coupled with experimental investigation of the properties determined via mathematical analysis. This has served to further our understanding of the complex dynamics of genetic networks and has demonstrated the strength and effectiveness of network motif studies to the molecular biology community.

2.2 Cell-centered modeling of tissue

Modeling tissues and organ level processes have been of great interest recently. Often modeling a tissues involves interconnecting various detailed models of sub-cellular and inter-cellular processes. Arguably such approaches can result in accumulated complexity and therefore potentially suffer from the same problems as their *in vivo* counter parts when it comes to understanding the systemic behavior of interest. Biological systems are inherently stochastic and often overwhelmingly complex. To a large extend the effectiveness of models in advancing our understanding comes from their power to reduce the complexity in a manner that is helpful in addressing a specific question. Therefore a model should not aim at producing an *in silico* replica of a biological system, but rather aim at capturing behavior at the appropriate level via well-justified simplified abstractions. This concept is effectively illustrated via an analogy in [21]; One can construct a car from LEGO bricks using a step-by-step manual. Such a replica

is an accurate representation of the actual car but does not necessarily provide an insight into how a car functions. One can gain insights by focusing on functional components (e.g. engine and differentials) and their interactions while setting aside arbitrary properties such as paint, number of pistons etc.

2.2.1 Spatial modeling of plant developmental processes

When it comes to modeling the role of signaling networks in plant tissue development, cells provide a natural level of abstraction. Plant cells are building blocks of the plant that semi-autonomously interact with their direct environment and compartmentalize the signaling networks that govern their growth, division and differentiation. Moreover, from a developmental point of view, the complexity at the plant cellular level is rather limited [26]. Cells can grow, divide, differentiate, retain their size, secrete and absorb molecules etc. Therefore in modeling plant tissue formation the focus is on how cells grow and divide and respond to signaling molecules that are transported between cells [21]. Consequently, any cell-centered model of plant tissue formation has to first extract rules about cell behavior from experimental observations. This constitutes a descriptive single-cell model. The single cell-behavior is integrated at the tissue level via a cell signaling network. The model assumptions regarding the cell behavior and the signaling network are then tested by the ability of the model to match existing experimental data (mutant and overexpression phenotypes, etc.) and its ability to make accurate testable predictions. Through iteration between experiments and modeling one can deduce the minimal set of cell behaviors that are sufficient to reproduce the tissue level behavior of interest. Ultimately this can leads to understanding of the role of the genetic regulatory networks that integrate single-cell behavior into tissue level phenomena.

Despite the advances made in formulating and executing complex computational simulations, modeling even the simplest tissue forming processes, can be a challenging endeavor. Therefore developmental systems with inherently simple architecture and dynamics serve as a good testbed

to generate and develop interdisciplinary research methods to study tissue/organ dynamics. In the remainder of this chapter I review specific plant tissues, and developmental stages that are the subject to theoretical studies in this thesis.

2.2.2 Shoot apical meristem

Shoot apical meristem (SAM) is a population of cells at the tip of the shoot apex that give rise to the aerial parts of the plant. SAMs are remarkably organized and stable structures that can retain functionality during the lifetime of a plant. This is despite the continual division, growth and differentiation of its constituent cells.

Daughter cells of the stem cells that remain at center of SAM replenish the stem cell pool, whereas daughter cells that are placed towards the peripheral zone (PZ), which is marked by a higher cell division rate, enter differentiation and form organ primordia. The shape and the domain structure of the SAM are kept unchanged, although all cells continuously divide and differentiating stem cell daughters leave the meristem. Cell tracking and ablation experiments demonstrate that the fate of each cell is determined by its current position and not by lineage specific heritage, highlighting the importance of cell-cell communication [58–60]. Due to its changing cellular context, pattern formation of the shoot meristem does not rely on a stable point of reference, but rather occurs in a self organized manner [61]. Current data demonstrates that the feedback loop between *CLAVATA3* gene (*CLV3*), expressed in the stem cell niche, and *WUSCHEL* gene which is expressed in organizing center (CZ) (*WUS*) plays a central role in SAM organization [62]. For a more detailed description of meristem zones and WUS and CLV3 interactions see chapter 3.

The strong evidence for self-organization, limited cell differentiation and relatively simple geometry of the SAM constitute an optimal setting for investigation of self-organized patterning in plants.

Previous computational models of SAM

The presence of cell lineage-independent self-organization suggests that the internal structure is maintained by a network of signals that interact with each other and can create stable isolated peaks of concentration [62]. Activator-inhibitor models have been the main approach in modeling the self-organized pattern formation in the SAM. Jönsson *et al.* in 2005 [63] were the first to model the stem cell regulation in the SAM using an activator-inhibitor model. This was followed by a model by Hohm *et al.* [64] which could not only reproduce the expression patterns observed in the wildtype SAM, but also some mutants and gene up and down-regulation phenotypes, further demonstrating the capability of activator-inhibitor models in accounting for SAM organization. The activator-inhibitor based models can account for some fundamental aspects of stem cell regulation within the SAM, albeit lack of data has led to various assumptions, particularly regarding the CLV3-independent regulation of WUS. The *clv3* mutant phenotype can be reproduced by assuming a molecule that inhibits WUS through a reaction-diffusion system. Published activator-inhibitor based models of SAM regulation incorporate such a hypothetical factor into their models in order to explain the CLV3 independent confinement of WUS expression. Additionally, often restricted zones of expression/activation of WUS, CLV3 or other molecules are incorporated in order to account for the specific geometry of gene expression in the SAM.

Mathematical models of pattern formation in the SAM, like other spatial models of cellular development, have restrictions regarding the level of detail and the scope of the model. Often it is unavoidable to consider the input of other processes as pre-patterns. At the same time it can be argued that when the WUS/CLV3 patterns are essentially pre-defined, the resulting model does not exhibit self-organizing properties. In this regard the current modeling efforts can be divided in two groups: models that focus on the emergence of CLV3 and WUS patterns via the interaction of network components [63–65] and others that investigate the role of such stable pattern in SAM organization [66–68].

Models in both groups include pre-patterns. For instance a signaling molecule that established an apical basal axis is a common factor in many of these models. Arguably such an assumption does not undermine the self-organizational aspects of the model (i.e. when the new pattern is not a simple and linear mapping of pre-pattern). However when such pre-patterns dictate WUS and/or CLV3 expression/activation zones, the resulting patterns are not self-organized. While the first group of models point towards pattern formation via an activator-inhibitor system, several of the models in the second group, have demonstrated the interaction between the WUS/CLV3 patterns and Ck signaling/perception network [66–68]. For instance, Yadav *et al.* [66] investigate a model that relates Ck perception via AHK4 receptor to pattern formation in the SAM. In this model, Ck is induced by an AHK4/Ck signal, which is produced at the center of OC. The expression zones (i.e. binary expression templates) of WUS, CLV3, and KAN1 are restricted to the center of the SAM, OC, and the peripherial zone (PZ), respectively. Given these inputs the model can robustly establish the spatial patterns of WUS, CLV3 and KANDI1. Furthermore, these patterns can withstand perturbations caused by cell growth and division. In the aforementioned work the localized expression of AHK4 at the center of the OC is fundamental for correct patterning of WUS. This suggests that the patterning of OC takes place at the level of Ck reception and signaling. Consequently, this implies that the self-organizing properties of the OC, arise from the underlying Ck signaling/perception pattern.

2.2.3 Plant embryo

Arguably the ideal developmental stage to study pattern formation is embryogenesis. During embryogenesis, both in plants and animals, the organism develops from several equivalent cells to an intricate collection of cell types and gene expression patterns. In animal embryonic development, cell movement and migration play a crucial role. In contrast, in plant embryo, due to the fused cell walls no cell movement/migration occurs, therefore precise control of cell growth and division is essential in correct development of plant embryo [69]. During plant

embryogenesis dynamic spatial patterns of diffusing morphogens carry information that regulate organism-scale development [69, 70]. The development of a plant can thus be described as the accumulations of successive patterns of gene expression and subsequent cell-fate determination. In very early embryonic development, this fewer established patterns exist and relatively few morphogens have to be taken into account. Moreover, after only a few rounds of cell division the embryo forms all vegetative tissues that are present in the mature plant. In other words by the mid-heart stage the fundamental tissues that constitute a plant are established [71]. Compared to the mature plant, these tissues are less complex; There are fewer cell types and in general and less differentiation events have occurred [71]. Furthermore during early embryogenesis, patterning in terms of cell geometry and gene expression are in place, while cell differentiation does not occur until later [72]. This provides an excellent opportunity to study the mechanism of pattern formation without having to take into account the extra complexity added by the process of differentiation. In Chapter three, this situation is exploited to study vascular pattern formation in embryo. In summary plant embryo development offers a minimal and simple platform for modeling and analysis of spatial genetic patterns that govern development.

CHAPTER 3

Centering the organizing center in Arabidopsis meristem

Adopted form the publication in plose one, Feb 2016
DOI: 10.1371/journal.pone.0147830

Milad Adibi[1,a,*], Saiko Yoshida[2,b], Dolf Weijers[2], and Christian Fleck[1,*]

[1] *Laboratory of Systems and Synthetic Biology, Wageningen University, the Netherlands.*

[2] *Laboratory of Biochemistry, Wageningen University, the Netherlands.*

[a] *Current address: Max Planck institute for plant breeding research, Cologne, Germany.*

[b] *Current address: Institute of Science and Technology (IST) Austria, 3400 Klosterneuburg, Austria.*

[*] *adibi@mpipz.mpg.de (MA); christian.fleck@wur.nl (CF)*

3.1 Introduction

Genetic studies mainly in *Arabidopsis* reveal that the WUSCHEL (WUS) and CLAVATA3 (CLV3) feedback loop is a pivotal regulator of stem cell number [59, 62, 73]. A small cell group underneath the stem cells named organizing center (OC) expresses the transcription factor WUS that maintains the stem cell in two ways. First, WUS protein moves into the stem cells, presumably through intercellular plasmatic bridges, called plasmodesmata [74]. In the stem cells, WUS directly binds to the promoter of *CLV3* and promotes transcription, in addition to maintaining pluripotency through a yet unidentified mechanism [62]. *CLV3* encode a small extracellular signal peptide that binds to receptor kinase complexes, including CLV1, and triggers an intracellular signal cascade that downregulates *WUS* transcription [62, 75]. This negative feedback loop between OC and stem cells provides a mechanistic framework to keep the number of stem cells constant [62], see Fig. 3-1A. Second, in the OC cells, WUS directly represses transcription of *ARABIDOPSIS RESPONSE REGULATOR 7* (*ARR7*) and 15 (*ARR15*) genes [76], which encodes intracellular inhibitors of response to the plant hormone Cytokinin (CK), thereby promoting cellular CK response [77]. Hence, the question of how WUS expressions is centered and restricted within the SAM, becomes a key question in studying the stem cell homeostasis in the SAM.

Several lines of evidence further indicate that CK is an important factor in shoot meristem regulation: first, mutants deficient in CK biosynthesis, reception, or overexpressing CK degrading enzymes, have a reduced SAM size [73, 79, 80]. Second, the CK receptor, arabidopsis histidine kinase 4 (AHK4), is expressed in the meristem center, overlapping with the OC in its distal part [67]. The receptor is involved in the upregulation of WUS expression via exogenously supplied CK at relatively high levels, and it has been assumed to confer WUS regulation also at endogenous CK levels. CK response, measured by the reporter pTCS, peaks at the OC [68], in agreement with WUS enhancing CK response in these cells. Based on the expression pattern of the transcription factor SHOOTMERISTEMLESS (STM) that promotes expression of the CK

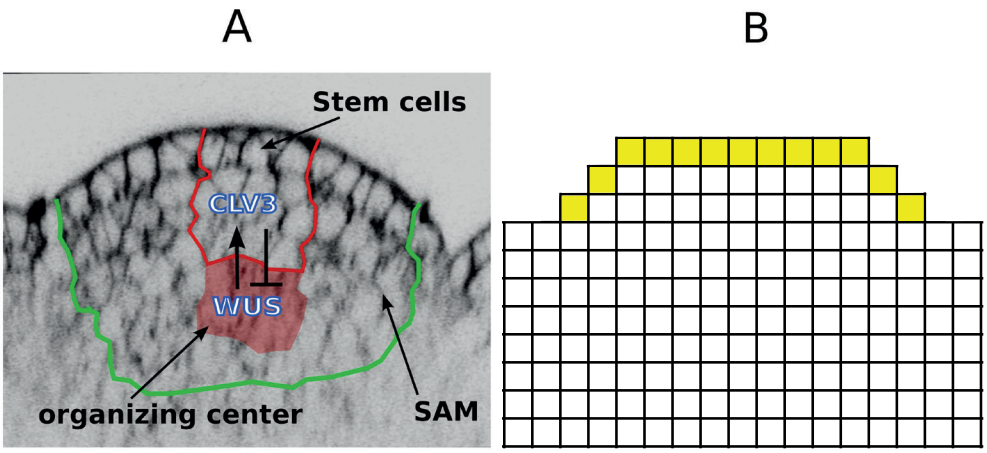

Figure 3-1: SAM architecture and its representation in the model. (A) An image of the SAM and the immediate surrounding area. The regions of interest are marked with colored boundaries. Modified with permission from [78]. (B) Schematic representation of WUS and CLV domains; The three dimensional SAM consisting of cells of various shapes and sizes is modeled by a two dimensional grid consisting of identical blocks representing cells. The enclosed cells represent the direction in which the field of cells extends (basal and lateral directions).

synthesis gene *ISOPENTENYL TRANSFERASE* 7 (*IPT7*), CK is probably produced broadly throughout the shoot meristem, although direct evidence is still missing [81]. Furthermore, immunodetection of CKs suggest a rather broad and uniform distribution throughout the shoot meristem in *Sinapsis alba* [82]. Recent findings in rice indicate that activation of CK (clipping of a ribose residue) by the LONELY GUY (LOG) enzyme is confined to the 2-3 outermost cell layers of the shoot meristem, and it has been discussed whether active CK is locally produced in the shoot meristem and moves from the top downwards [73, 83]. In arabidopsis, there are eight LOG homologs. One of them, LOG4 is specifically expressed in the L1 layer, but the expression patterns of the other *LOG* genes are unknown and at least some of the other LOG genes seem to be also expressed in the shoot meristem [58, 67].

3.2 Aim of this study

The capability of activator-inhibitor networks in accounting for SAM patterning has been already demonstrated. In general, the experimental identification of network components has been a

major challenge in application of reaction-diffusion models in biology. Particularly in the plant field, it remains a major challenge to demonstrate the existence of reaction diffusion networks experimentally.

In our context this highlights the importance of motivating the pre-patterns of a model by known biological knowledge as much as possible; when pre-patterns are abstract and cannot be directly linked to the known biological mechanisms, the task of experimental identification of network components is complicated. In contrast, when these assumptions are motivated by experimental observations, they can be more readily investigated via experimentation. As discussed earlier, theoretical and experimental data point towards CK signaling and perception as a fundamental factor in patterning of the SAM [66–68]. Here we aim to expand upon the current state of research and avoid incorporation of abstract assumptions in our model, by utilizing the available data as much as possible. Our model links WUS/CLV3 feedback loop to an activator-inhibitor system based on CK signaling. We demonstrate that these components function together to position WUS expression at the OC.

3.3 The Model

In order to investigate the apical-basal position and the lateral extension of the OC within the shoot meristem, we chose a two dimensional model of a longitudinal section. In our model, mobile signals are free to diffuse out of the SAM and into the surrounding cells, (Fig. 3-1). The system is described by a set of coupled non-linear ordinary differential equations on a discrete grid, where the grid points represent the individual cells. Hence, cells are assumed to be spatially uniform and intracellular concentration gradients are not taken into account, which is considered a reasonable simplification due to the difference in timescale between cytosolic mobility (fast) and the actual pattern formation process, i.e., gene expression (slow). Therefore, we use the term diffusion not in its actual physical but rather in an effective sense, meaning unbiased bi-directional spread of molecules between cells through special openings termed

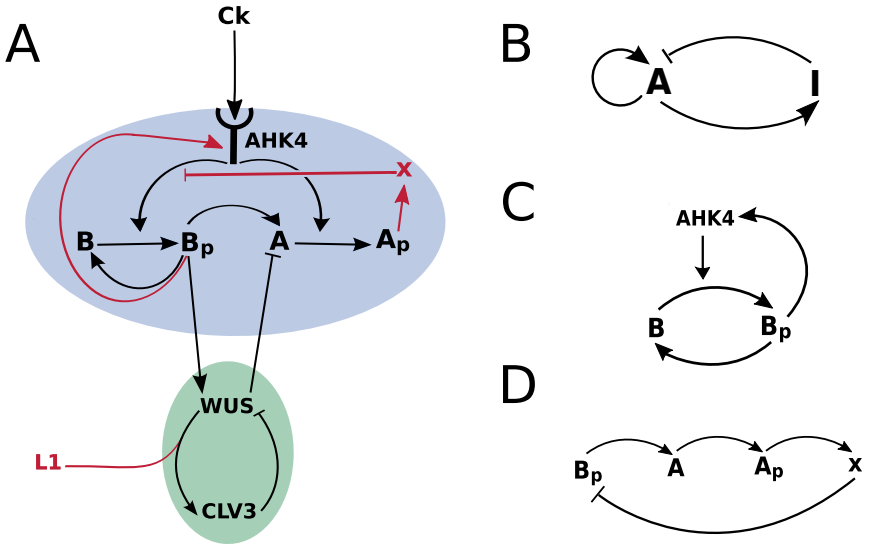

Figure 3-2: Two coupled sub-networks and boundary information define WUS and CLV3 expression domains in the SAM. A and B stand for type-b and type-A ARRs. A_p and B_p denote phosphorylated type-B and type-B ARRs. (a) The model can be divided into the CK signaling and WUS/CLV3 sub-networks. The former determines the position of the WUS domain via a self-organizing system while the latter specifies the CLV3 domain, taking the WUS domain as an input. Parts of the CK signaling sub-network correspond to the components of the (b) classical activator/inhibitor system; (c) the the network component corresponding to the autocatalytic activator and (d) to the activation/inhibition interactions.

plasmodesmata or via the apoplast. Moreover, for simplicity, we assume that the dynamics of the WUS/CLV3 regulatory system arising from the assumed reaction-diffusion system are sufficiently faster than the cell division rate in the SAM. Therefore, the essential features of the patterning process of the aforementioned system can be well described by a static model that does not incorporate cell division or growth.

3.3.1 Facts and assumptions underlying the model

The proposed model is based on the following published results:

- CK binds to the AHK4 receptor, which in turn causes phosphorylation of both type-A and type-B ARRs via arabidopsis histedine phosphotranfer proteins (AHPs) [84]. In absence of CK the receptor functions as a phosphatase [85, 86].

- Type-B ARRs are transcription factors that activate transcription of CK response genes, including type-A ARRs [87].
- Type-A inhibit type-B ARR function, the precise mechanisms has yet to be determined [77, 88]. Evidence suggests that type-A ARRs inhibit type-B ARRs via repression of upstream CK signaling. In addition it has been proposed that type-B repress type-A via competition for phosphate molecules [89].
- There is a feedback loop between *WUS* and *CLV3* genes, where WUS moves from the OC into the stem cells and activates the transcription of the *CVL3* gene. The CLV3 peptide is mobile and inhibits the expression of WUS [62, 90].
- Expression of WUS is activated by CK signaling [67], presumably via canonical type-B ARRs effector genes. Additionally WUS represses the expression of type-A ARRs [76], thus promoting CK signaling.

In addition, our model incorporates the following assumptions:

- The SAM consists of equivalent cells that have the potential to express all genes included in the model. The exception is the epidermis (L1 layer), which is assumed to be different from the rest of the cells in the SAM. This means that in our model the identity of the L1 cell layer is not determined via the proposed self-organizing mechanism.
- We hypothesize a molecule (L1 signal) that is supplied by the uppermost cell layer (L1) and diffuses downward, establishing a gradient. The presence of this molecule is necessary for the cells to be able to respond to WUS signal by producing CLV3. Such a molecule has been identified by Knauer *et al.*, who charactrized a microRNA, miR394, that is produced at the L1 layer and is required for establishment of CLV3 expression. In our model the L1 signal is necessary for cells to be able to respond to WUS and establish stem cell identity [91].

- A diffusing inhibitor and a self-activating component are essential parts of pattern forming activator-inhibitor mechanisms [92]. Currently there is no evidence of such an inhibitor involved in SAM patterning; our trials show that several molecules within the model can be assumed to act as an inhibitor or to induce an inhibitor. For example, type-A ARRs appear as a plausible candidate for the role of the inhibitor. It is known that type-A ARRs inhibit CK signaling [77]. In the model the inhibitor is assumed to be downstream of the type-A ARRs. This is because to fulfill the role of the inhibitor within an activator-inhibitor system, type-A ARRs have to be highly mobile signals. In absence of evidence regarding the mobility of these molecules, we assumed that the inhibitory function is conveyed via a highly mobile intermediate, factor X. Thus in our model two mechanisms exist for inhibition of type-B by type-A ARRs, via phosphate competition and via factor X.

- We assume that type-B ARRs promote CK signaling via direct induction of AHK4. Experimental results presented on Arabidopsis eFP browser [93], (data from AtGenExpress project [94]) show that application of Zeatin leads to significant up-regulation of AHK4 levels. For the model, this assumed interaction constitutes the autocatalytic loop of the activator-inhibitor subnetwork.

- In our reductionist approach, we do not distinguish between mRNA and protein of the genes unless it is essential in addressing the question at hand. Considering the expression pattern of *CLV3* mRNA [62] and its demonstrated inhibitory effect at the OC, it becomes apparent that CLV3 elicits a signal that travels further than its mRNA. This is reflected in the model by distinguishing CLV3 mRNA and protein. The mRNA is assumed to be immobile while the protein is able to diffuse.

- In the model we assume that phophotransfer from the receptor to the ARRs are sufficiently fast processes compared to gene expression. Therefore the phosphotransfer is implemented using a quasi-steady-state assumption. See details in discussion.

Reaction-diffusion modeling of the SAM has a history of more than a decade and the model presented in this work is inspired and motivated by earlier modeling efforts. It utilizes concepts and components (experimentally verified as well as hypothetical) put forward in earlier works. In particular, factor X is a universal component of activator-inhibitor models of the SAM [63–65, 95]. As the inhibitor in an activator-inhibitor systems, models consistently predict it to be a fast diffusing molecule with an expression pattern centered around OC. To date evidence for a molecule that fulfills the role of such inhibitor and matches its predicted expression pattern has not emerged. Similarly the concept of L1 signal was first established by Joensson *et al.* in [95]. In later works this was utilized as a signal defining the lateral expression of WUS [96], as well as in an apical-basal setting, as a cofactor that along with WUS is required for production of CLV3, in both two-dimensional [74], and three-dimensional settings [66]. In our model the L1 signal is essentially the same as the in latter; an apical basal signal required for CLV3 induction in response to WUS. As already pointed out in [66], the strongest evidence for the existence of such a signal comes from the observation that in *pCLV3::WUS* both *WUS* and*CLV3* are expressed in the uppermost three cell layers of the SAM [97].

3.3.2 Model equations

Integrating the above stated experimental observations and hypothetical assumptions in a mathematical model, we arrive at the following system of non-dimensionalized coupled ordinary

differential equations:

$$\frac{dB_{ij}}{dt} = \frac{k_1\Gamma_{ij}B_{ij}}{(1+k_6X_{ij})} - k_7B_{ij} + \hat{D}B_{ij} \tag{3.2}$$

$$\frac{dA_{ij}}{dt} = \frac{k_8\Gamma_{ij}B_{ij}}{(1+k_6X_{ij})(1+k_9W_{ij})} - k_{10}A_{ij} + d_1\hat{D}A_{ij} \tag{3.3}$$

$$\frac{dR_{ij}}{dt} = \frac{k_{11}\Gamma_{ij}B_{ij}}{1+k_6X_{ij}+k_{12}\Gamma_{ij}B_{ij}} - k_{13}R_{ij} + d_2\hat{D}R_{ij} \tag{3.4}$$

$$\frac{dX_{ij}}{dt} = k_{14}\Gamma_{ij}A_{ij} - k_{15}X_{ij} + d_3\hat{D}X_{ij} \tag{3.5}$$

$$\frac{dW_{ij}}{dt} = \frac{k_{16}\Gamma_{ij}B_{ij}}{(1+k_6X_{ij})(1+k_{17}Cs_{ij})} - W_{ij} + d_4\hat{D}W_{ij} \tag{3.6}$$

$$\frac{dC_{ij}}{dt} = \frac{k_{18}L_{ij}W_{ij}}{1+k_{19}W_{ij}} - k_{20}C_{ij} \tag{3.7}$$

$$\frac{dCs_{ij}}{dt} = k_{21}C_{ij} - k_{22}Cs_{ij} + d_5\hat{D}Cs_{ij} \tag{3.8}$$

where we defined:

$A :=$ [type-A ARR]; $B :=$ [type-B ARR]

$C :=$ [CLV3 mRNA]; $Ck :=$ [Ck]

$Cs :=$ [CLV3 peptide]; $R :=$ [AHK4]

$W :=$ [WUS]; $X :=$ [Inhibitor]

$L :=$ [L1 signal]

$$\Gamma_{ij} := \frac{Ck_{ij}R_{ij}}{(1+k_2Ck_{ij}+k_3R_{ij})(1+k_4A_{ij}+k_5B_{ij})}. \tag{3.9}$$

The subscript ij denotes the position $x = x_{ij}$ on the grid and L_{ij} and Ck_{ij} refer to the L1 signal and the CK expression profiles. These profiles are each independent of other molecules in the model and can be determined analytically, as described in the next section. The spatial coupling between the grid points is achieved by the diffusion operator $\hat{D}$ operating on the square grid index is defined by:

$$\hat{D}C_{ij} = C_{i-1j} + C_{i+1j} + C_{ij+1} + C_{ij-1} - 4C_{ij}.$$

We use reflecting boundary conditions for the apical side. The basal and lateral boundary is not well defined; we use boundary conditions which are, for simulation purposes, equivalent with using an infinite domain for the apical-basal dimension; in the numerical simulations the grid is extended in basal and lateral directions until the concentrations decay to almost zero; this makes the boundary condition at the basal and lateral end of the grid irrelevant and provides a good approximation for the *in vivo* SAM. We close the domain basally and laterally using reflecting boundary conditions. All simulations, unless stated otherwise, were carried out in a cell grid where the first three staggered rows capture the domes-shaped architecture of the SAM (Fig. 3-1A). Parameters were chosen from the biological and physical relevant ranges and adjusted to maximally approximate the available data. All simulation where carried out with arbitrary initial concentrations of all the molecules in the model, within the [0,0.5] range. Simulations were continued until the steady state was reached. We always checked that the grid is large enough to approximate an infinite domain in the described manner. In figures that display model outputs, the area of the grid that contains no information has been cropped. For examples of models out put in an uncropped template see Fig. 3-4. For a list of parameters used in model simulations see appendix A.1.

3.3.3 Derivation of phosphate transfer function

The AHK4 receptor exhibits the interesting feature that it works as a kinase as well as a phosphatase depending on whether CK is bound to it or not [98]. The other interesting feature is that phosphorylation of the type-A and type-B ARRs is not directly but through phosphotransfer proteins, the AHP family. For simplicity we assume in the following derivation of the transfer function that the CK signaling, i.e., binding of CK to AHK4, binding of AHP to AHK4, phosphorylation of AHP, phosphorylation of the ARRs are sufficiently fast processes compared to the time scale of gene expression. Moreover, we consider the extracellular binding of CK to AHK4 as being independent of the intracellular binding of AHP. Using the quasi-steady state

assumption and suppressing for notational simplicity the spatial index on the concentrations we find for the amount of receptors occupied by CK: $R_b = \alpha Ck R(1+\alpha Ck)^{-1}$ and for the unoccupied receptors: $R_f = R(1+\alpha Ck)^{-1}$, where Ck denotes the CK concentration (we neglect the depletion of the free CK by binding to AHK4), R is the concentration of AHK4, and α is the corresponding inverse K_d value of the binding reaction. Assuming further a surplus of AHP phosphotransfer proteins compared to the amount amount of AHK4 receptors, the abundance H_p of phosphorylated AHPs is given by: $H_p = \gamma R_b(1+\beta R_f)^{-1}$, where γ and β describe the kinase and phosphatase activity of the receptor, respectively. The phosphorylated AHP (H_p) can bind either to type-A (A) or type-B ARR (B), hence A and B compete with each other for H_p. Using again the quasi steady-state assumption we find for the fraction of phosphorylated A:

$$\frac{A_p}{A} = \sigma_A \frac{H_p}{1+\sigma_A A + \sigma_B B}.$$

Here σ_A and σ_B are the inverse K_d values for the binding reactions for A and B, respectively. Inserting the above results for H_p, R_b, and R_f we arrive at:

$$\frac{A_p}{A} = \sigma_A \alpha \gamma \frac{CkR}{(1+\alpha Ck+\beta R)(1+\sigma_A A+\sigma_B B)}.$$

To obtain non-dimensional quantities we rescale all concentrations with the half-maximal concentration $W_{\frac{1}{2}}$ of the CLV3 activation by WUS, Eq. (3.7). Defining: $k_2 := \alpha W_{\frac{1}{2}}$, $k_3 := \beta W_{\frac{1}{2}}$, $k_4 := \sigma_A W_{\frac{1}{2}}$, $k_5 := \sigma_B W_{\frac{1}{2}}$ yields:

$$\frac{A_p}{A} \sim \Gamma.$$

where Γ is the transfer function for describing the two-step phosphorelay given in Eq. (3.9). Following the suggestion in the literature [98] that the phosphotransfer to the type-B ARR is inhibited by phosporylated type-A ARR, we assume that a non cell-autonomous inhibitor X, which is activated by A_p, inhibits the phosphorelay to type-B ARR non-competitively:

$$\frac{B_p}{B} =\sim \frac{\Gamma}{1+k_6 X}.$$

Rescaling time with the inverse degradation rate of WUS, the other terms in Eqs. (3.2) - (3.8) follow directly from the assumptions described above.

L1 signal and CK profile

For both the L1 signal and CK the problem can be described as diffusion in one-dimensional semi-infinite space with finite production regime. We approach the problem by dividing the space into two section, a region where the signaling molecule is produced, and a region where the production of the signaling molecule does not occur.

For simplicity we treat space as continuous; the corresponding partial differential equation for the concentration ϕ of a diffusing molecule in steady state reads:

$$\begin{aligned}
D\frac{\partial^2\phi_<}{\partial x^2} - \lambda\phi_< + \Gamma &= 0: \qquad x \le x_0 \\
D\frac{\partial^2\phi_>}{\partial x^2} - \lambda\phi_> &= 0: \qquad x > x_0 \\
D\left.\frac{\partial\phi_<}{\partial x}\right|_{x=0} &= 0 \\
\phi_<(x_0) &= \phi_>(x_0) \\
D\left.\frac{\partial\phi_<}{\partial x}\right|_{x=x_0} &= D\left.\frac{\partial\phi_>}{\partial x}\right|_{x=x_0} \\
\lim_{x\to\infty}\phi_>(x) &= 0
\end{aligned}$$

In above equations λ is the degradation rate, Γ is the production rate of the signaling molecule in the production domain and D is the diffusion rate. Rescaling the spatial dimension with the typical length scale L for a cell in the SAM tissue, i.e. $\tilde{x} = x/L$, the solution to these equations are given by:

$$\phi_<(\tilde{x}) = \frac{\Gamma}{\lambda}\left(1 - e^{-\frac{n_0}{\tilde{l}}}\cosh\left(\frac{\tilde{x}}{\tilde{l}}\right)\right) \qquad \tilde{x} \le n_0 \tag{3.10}$$

$$\phi_>(\tilde{x}) = \frac{\Gamma}{\lambda}e^{-\frac{\tilde{x}}{\tilde{l}}}\sinh\left(\frac{n_0}{\tilde{l}}\right) \qquad \tilde{x} > n_0 \tag{3.11}$$

where $\tilde{l} := \sqrt{d/(\lambda L^2)}$ and $n_0 = x_0/L$. The L1/CK profile is given by $L1_{ij}/CK_{ij} = \phi(x = i)$. The rescaled profile $\phi/\phi(\tilde{x} = 0)$ is shown in Fig. 3-3 for different values of n_0 and $\tilde{l}$, corresponding to L1 and CK, resp.

We take the observation that CK profile is not observed after the 25th cell layer into account by requiring $CK_{i=25j}/CK_{i=1j} = 1/2$. From this follows:

$$25 - n_0 \quad = \quad \tilde{l} \ln\left(1 + \exp\left(-\frac{n_0}{\tilde{l}}\right)\right)$$

which can only be solved numerically. Rewriting the root of this equation, $\tilde{l} = \tilde{l}(n_0)$, for the inverse degradation rate- $\lambda^{-1} = \tau$, the average lifetime, finally yields the relation between the lifetime, synthesis range and diffusion constant:

$$\tau(n_0, d) = \frac{\tilde{l}^2(n_0)L^2}{d}.$$

In Fig. 3-14 we used $L = 5\mu\mathrm{m}$, taken from [99]. The function Γ is the transfer function for the two step phosphorelay from CK binding to the phosporylation of the ARRs .

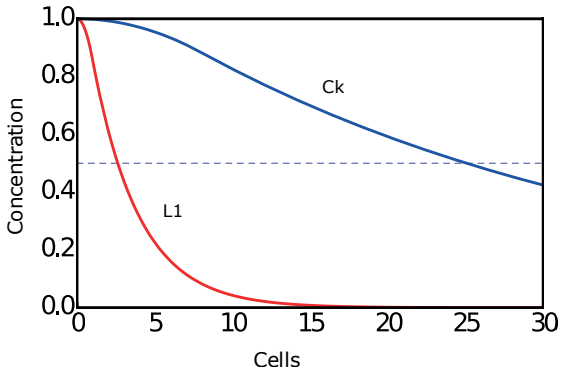

Figure 3-3: Boundary layer profiles. Re-scaled (ϕ/ϕ_0, $\phi_0 = \phi(0)$) concentration profiles as given by Eqs. (3.10) and (3.11) of the L1 (red) signal and CK (blue). The distance from the L1 layer is measured in units of the average cell size within the meristem. Parameters used: $n_0 = 1$, $\tilde{l} = 4$ for L1 and $n_0 = 8$, $\tilde{l} = 30$ for CK concentration profiles.

3.3.4 Mobility of molecules in the model

In a model, the 'assigned' mobility of molecules can occur at the level of any intermediate components that are not explicitly present in the model. Moreover, in such a case, often, mRNA

and protein of a gene are considered a single identity, hence in reality, the assigned mobility can occur at the level of either mRNA or the gene.

The correct patterning of the model depends on mobility of WUS, CLV3 peptide, L1 signal and factor X. WUS needs to me mobile to reach L1 layer and trigger the expression of *CLV3*. The mobility of WUS protein has been demonstrated previously and WUS protein is detected at L1 layer [90]. In order to inhibit WUS at the OC, CLV3 is required to be mobile in the model. Similarly the intercellular movement of CLV3 peptide has been established [75]. As an inhibitor in an activator-inhibitor system, the mobility of factor X is required for model functionality. As mentioned earlier, a feasible candidate for the role of L1 signal is miRNA394, which has been shown to act as a mobile signal. [91]

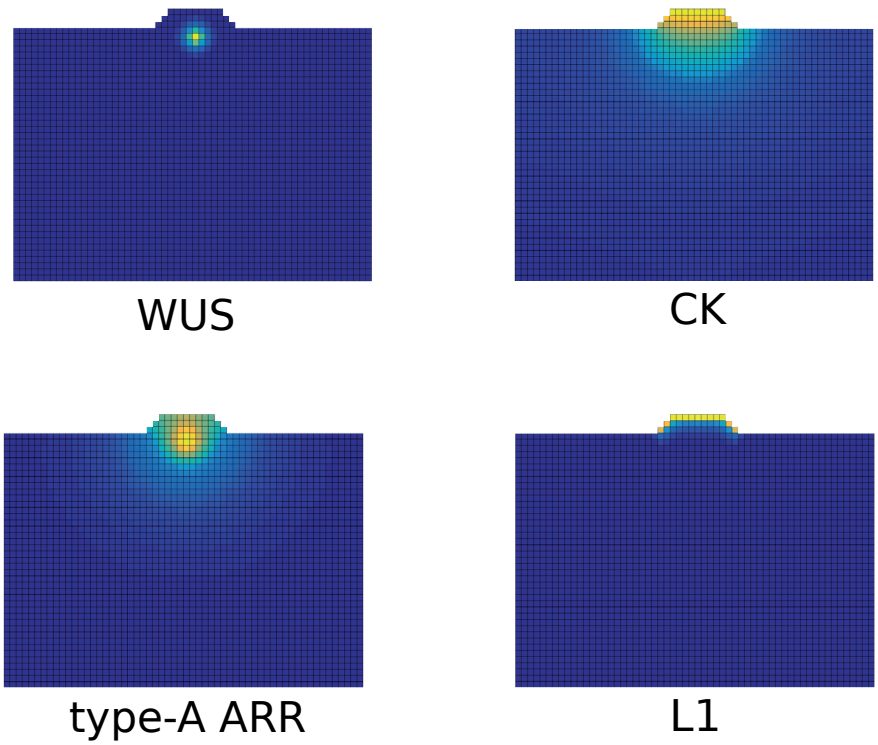

Figure 3-4: Examples of model output on the full simulation grid. The full simulation template constitutes a 45x60 rectangular grid. The concentration of the molecules approaches zero at the template boundary.

3.4 Model analysis

We tested whether the proposed model can account for the observed patterns of CLV3 and WUS in the SAM and whether it can reproduce known experimental results, which are relevant to the patterning process. To this end, we performed numerical experiments: we examined whether the model is capable of reproducing the observed phenotype of wildtype SAM as well as various non-wildtype scenarios including mutants and overexpression lines. Because we use a mechanistic model, we can map experimental manipulations directly to the parameters of the model. Therefore the non-wildtype scenarios can be implemented by changing the model component that corresponds to the specific mutation, overexpression, etc. For instance, a knock-out mutation is implemented by setting the production rate of the affected gene to zero. To simulate the ablation scenarios, the appropriate changes are applied to the wildtype system at the steady sate. Once the system reaches a steady state again, the resulting expression patterns are compared against the experimental observations.

3.4.1 Model subnetwork structure

The model in essence consists of two coupled subnetworks: WUS/CLV3 (Fig. 3-2A, lower part) and the CK signaling (Fig. 3-2A, upper part). In addition boundary information is supplied by CK and the L1 signal (Fig. 3-2A, red arrows; also see Fig. 3-3 for the profiles). Parts of the CK signaling network correspond to components of a classical activator/inhibitor system (Fig. 3-2A). The AHK4/B/B_p part of the network acts as an autocatalytic activator (Fig. 3-2C), while the pathway leading from B_p to X, fulfills the role of induction of the inhibitor by the activator (Fig. 3-2D). The CK gradient confines the domain of pattern formation to the upper part of the meristem. The activator-inhibitor network is coupled to the WUS/CLV3 subnetwork via an incoherent feed-forward loop (B_p/WUS/A) which specifies WUS expression by type-B ARR. The WUS/CLV3 subnetwork generates the expression domain of CLV3. Boundary information

supplied by the L1 signal determines the correct orientation of the CLV3 expression in the apical-basal direction.

3.4.2 Robust reproduction of the wildtype expression patterns of the genes included in the model

The *sine qua non* for the model is of course whether the observed wildtype pattern can be established and maintained. The simulated wildtype pattern is shown in Fig. 3-5. WUS is present in a high concentration in a small region at the center of SAM, which in both lateral and apical basal directions corresponds to the observed experimental pattern [62]. In our model the lateral position of a single WUS peak is always at the center, whereas the apical basal position depends on the region defined by CK. The size of the WUS domain depends on the dynamics of the activator-inhibitor subnetwork as well as inhibition from CLV3.

We investigated the effect of WUS mobility on model output by setting WUS diffusion to zero. This cell-autonomous version of WUS is only detected in the OC and is absent from the upper cell layers of the SAM, Fig. 3-7.A. This results in significant reduction of CLV3 levels and misplacement of its domain, Fig. 3-7.C in comparison to wildtype, Fig. 3-7.B and D. This simulated WUS pattern closely resembles the observed transcriptional pattern of *WUS* in the SAM [90, 100]. In contrast, when WUS mobility is considered in the model the resulting expression extends to the L1 layer, Fig. 3-7.B and D. The predicted patterns of AHK4 and WUS by the model, overlap in the OC. This has been observed experimentally and reproduced by previous models of WUS/CLV3 interactions [68, 101]. Furthermore the model predicts the WUS expression domain to constitute a sub-section of the broader AHK4 domain. This is in agreement with the observed distribution of *WUS::DsRed-N7* in the apical half of the AHK4 receptor domain marked by *AHK4::GFP*, in inflorescence meristem [67]. Patterns of type-A and type-B ARRs, see Fig. 3-5C and Fig. 3-5D, are comparable to the patterns reported by [68].It should be noted that the pattern of type-A ARR expression in the model refer to the

phohporylated portion of these proteins, while the relevant experimental data primarily consists of GUS reporter and transcriptional marker gene expressions [68, 76, 102]. This complicates the comparison of model output in terms of type-A ARR expression against experimental data. Nevertheless the model predicts that WUS expression domain and the domains associated with CK signaling (AHK4, type-A and type-B ARR expression domains), largely overlap. This is in agreement with experimental observations of ARR5 [67] and AHK4 [67, 68]transcriptional reporters in the SAM, as well as with previous models of mutual interactions between CK signaling and WUS in the SAM [67, 68]. *CLV3* (mRNA) expression is limited to the tip of the meristem, with an expression zone that is wider at the apical end and narrows towards basal limit of CLV3 expression, Fig. 3-5E. This is in agreement with the *CLV3* (mRNA) patterns observed experimentally.

We investigated the effects of our choice of representation of meristem and L1 layer on model output. We observed that the model is not dependent on this particular representation; model simulations using several other representations of meristemic geometry and L1 layer, produce the correct output, see Fig. 3-6.

3.4.3 Sensitivity Analysis

In order to analyze the model performance we carried out a parameter survey in which we compared the simulated patterns against experimental observations of WUS and CLV3 pattern in the SAM.

Cost function construction

The first step is to define a quantitative and biologically meaningful criteria to evaluate the model output against experimental observations of WUS and CLV3 pattern in the SAM. In evaluating the model output we are concerned with general patterning capabilities rather than reproduction of experimentally observed patterns in detail. Therefore we focus on essential

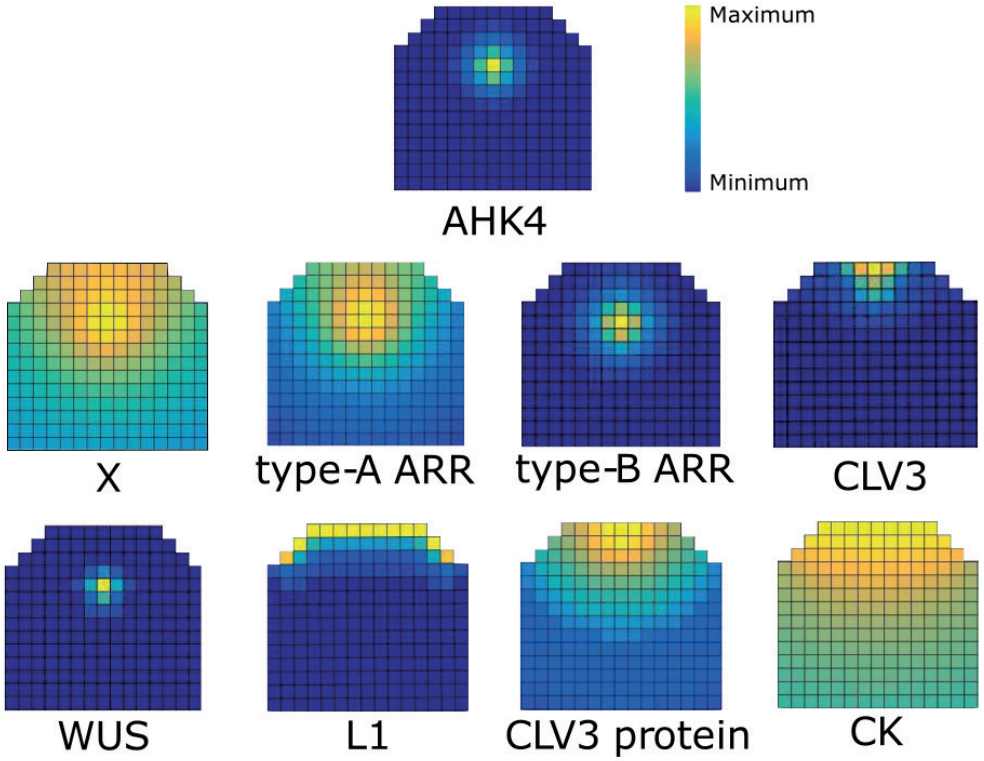

Figure 3-5: Wildtype expression pattern of the molecules in the model. (A) AHK4, (B) X, (C) type-a ARR (D) type-b ARR, (E) CLV3 mRNA, (F) WUS, (G) L1, (H) CLV3 protein, (I) CK. Dark red indicates the highest concentration and dark blue indicates zero concentration. The relative levels in each figure are depicted by a color spectrum shown by the color bar in (A).

features that define the existence of the correct pattern. This allows for variability in model output by not imposing a too strict of a criteria for the correct pattern. The output of the model can be assessed using the WUS and CLV3 concentration distributions. We define the following marginalized distributions:

$$\overline{W}_i(\vec{p}) = \frac{\sum_{j\in\Omega} W_{ij}(\vec{p})}{\|\sum_{j\in\Omega} W_{ij}(\vec{p})\|} \tag{3.12}$$

$$\overline{C}_i(\vec{p}) = \frac{\sum_{j\in\Omega} C_{ij}(\vec{p})}{\|\sum_{j\in\Omega} C_{ij}(\vec{p})\|} \tag{3.13}$$

Where $\|.\|$ denotes the L2 norm. The cell indices i and j are restricted to the integration domain Ω which consists of the uppermost 9 cell layers, encompassing the central region of the meristem; $\Omega = \{(i,j)|3 < i \leq 12; 2 < j \leq 11\}$. These profiles adequately capture the

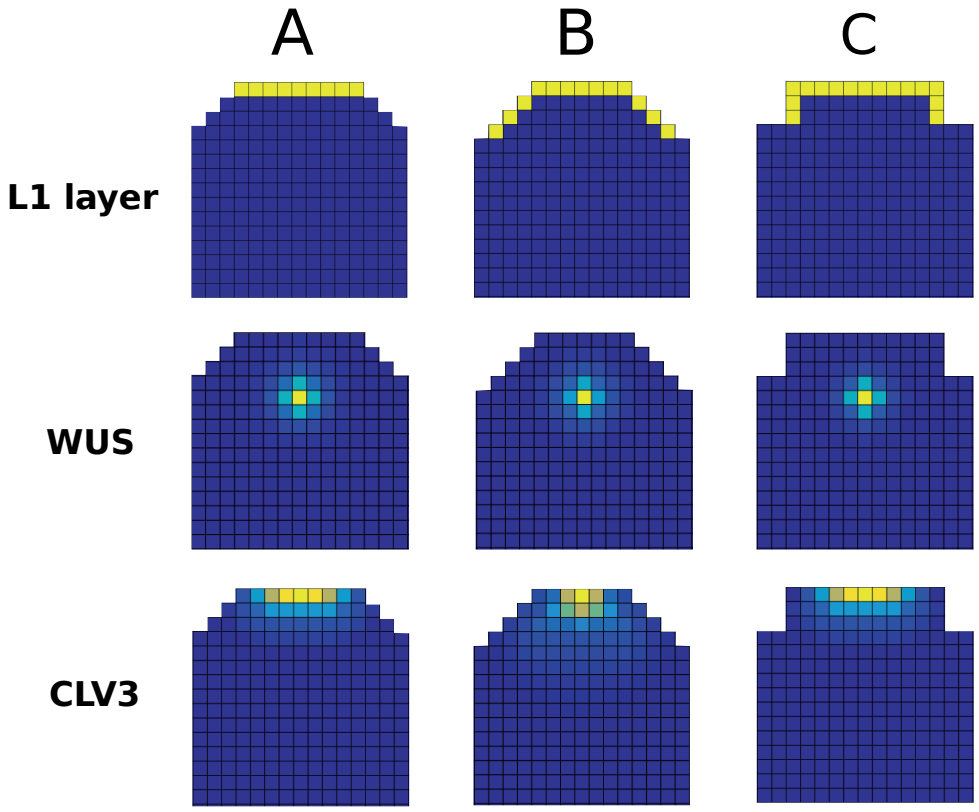

Figure 3-6: Simulation output in alternative templates and L1 layer assignment. WUS and CLV3 patterns resulting from model simulations in alternative templates. are qualitatively unchanged compared to wildtype. (A) The original template coupled with an alternative implementation of L1 layer. (B) Extension of meristem by one cell layer in apical direction.(C) A simple rectangular implementation of the meristemic dome.

distinguishing features of the patterns and can be obtained from the experimental data in the same manner (Fig. 3-8A). GFP intensity is used as a proxy for the concentration of WUS and CLV3 in an apical-basal cross-section of the 3D confocal stacks of SAM in pWUS-n3GFP and pCLV3-n3GFP respectively.

Using the two marginalized distributions given in equations. (3.12) and (3.13), we define two objectives as the distances between the marginalized profiles:

$$d_W(\vec{p}) = \|\overline{W}(\vec{p}) - \overline{W}_{\mathrm{ref}}\|$$

$$d_C(\vec{p}) = \|\overline{C}(\vec{p}) - \overline{C}_{\mathrm{ref}}\|.$$

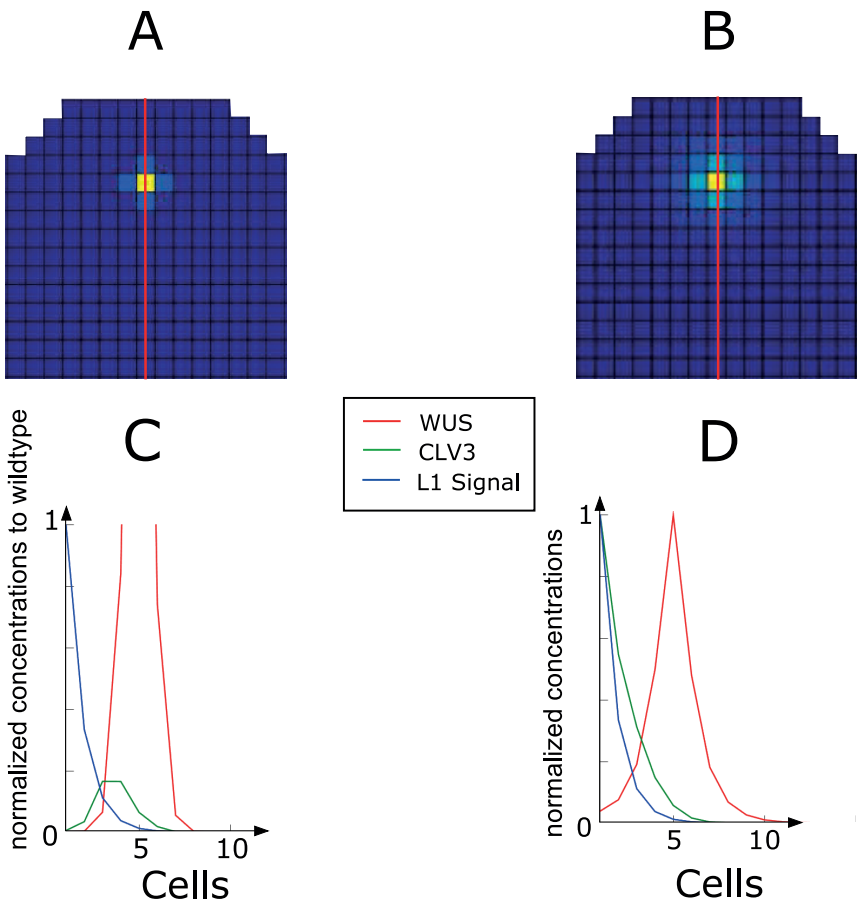

Figure 3-7: WUS mobility is required for correct patterning of WUS. (A) Model simulation of wildtype WUS pattern. (B) Model simulation of WUS pattern when WUS mobility is set to zero in the model. (C) Wildtype WUS, CLV3 and L1 signal profiles along the center-line of the meristem (as shown in (A) and (B)). WUS domain extends to L1 layer. CLV3 pattern has a maximum at L1 layer. (D) Effects of WUS immobility in the model; WUS is not present in the upper cell layers of the SAM and CLV3 domain is severely reduced and misplaced.

$\overline{W}_{\mathrm{ref}}$ and $\overline{C}_{\mathrm{ref}}$ are the experimentally obtained marginalized reference concentration profiles.

We aggregate the two objectives into a single cost function:

$$L(\vec{p}) = d_W(\vec{p}) + d_C(\vec{p}).$$

Next we preformed a parameter survey using the described cost function. Table S1 in appendix A lists the non-dimensionalized parameters used in simulations presented in the main text unless otherwise stated.

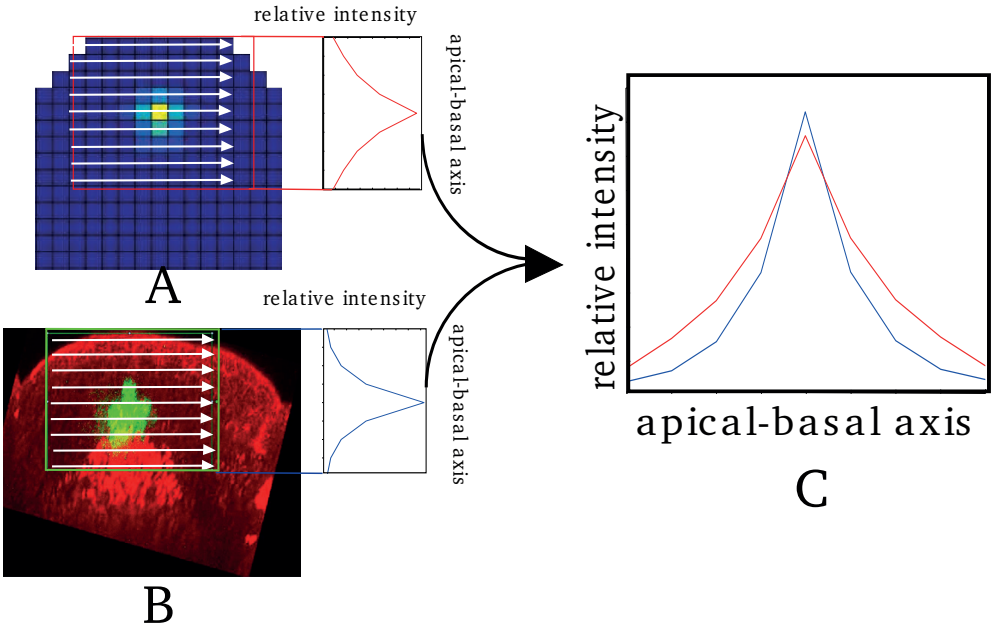

Figure 3-8: Scoring function objectives. (A) The scoring objectives focus on the a region of the cellular grid that corresponds to the stem cell niche and OC. From this a marginalized WUS/CLV3 concentration profile is obtained. (B) A reference WUS/CLV3 concentration is obtained from the experimental data. (C) The comparison of these two profiles provides a measure of the model output against the experimentally observed patterns of WUS/CLV3 in the SAM.

Parameter survey

Focusing on the aforementioned parameter set, $\vec{p}_1$, we define a hypercube Ω on the logarithmic scale, where we extended each parameter one order of magnitude in each direction: $\Omega_p = \Pi_j[p_1^j/10, 10p_1^j]$. Within this hypercube a total of $N = 2.5 \times 10^5$ parameter sets were generated. For each parameter set $\vec{p} \in \{\vec{p}_1, \vec{p}_2, ..., \vec{p}_N\}$ we calculated a score $L(\vec{p})$, as described above. The subset defined by $\omega_p = \{\vec{p} \in \{\vec{p}_1, \vec{p}_2, ..., \vec{p}_N\} | L(\vec{p}) < 0.1\}$ was obtained. Subset ω_p consists of parameter sets whose outputs are consistent with experimental observations. The threshold of 0.1 allows for variation in model output, while it insures the existence of the correct patterns.

For the subset of tested parameters for which the model performed in sufficient agreement with the experimental data we preformed a sensitivity analysis.

Sensitivity calculation

To characterize the effect of perturbations on model output a local sensitivity analysis was carried out. The normalized sensitivity of parameter p_i^j belonging to the parameter point $\vec{p}_i$ is defined by:

$$S_i^j = \frac{p_i^j}{L(\vec{p}_i)} \left| \frac{L(p_i^1, \ldots, p_i^{j-1}, p_i^j + \delta, p_i^{j+1}, \ldots) - L(\vec{p}_i)}{\delta} \right|.$$

From the set of S_i^j we calculated the quartiles as shown in the box-plot 3-9. For the sensitivity analysis $\delta = 0.01$ was used.

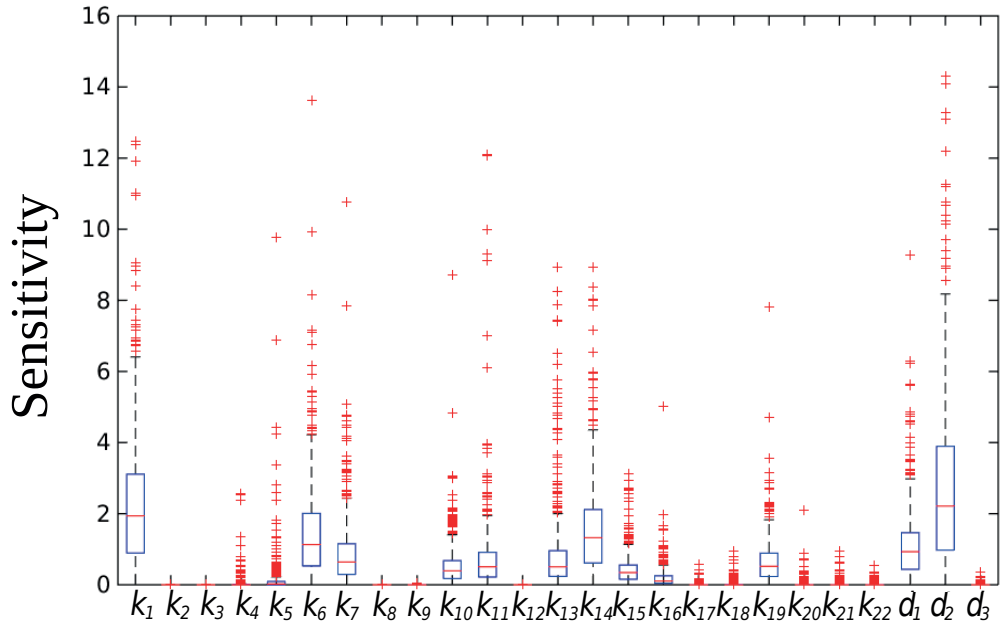

Figure 3-9: Parameter sensitivity. The plot displays the sensitivity of model parameters to small perturbations. Most parameter show little sensitivity, while k_1, k_6, k_{14} and d_2 show highest levels of sensitivity. In each box the central red line is the median. Edges of the box are the 25th and 75th percentiles. The whiskers show the range for data points that are not considered outliers. The red dots outside of this range are individual outliers. The parameter sets generated by the parameter survey and the sensitivity analysis, are all within the Turing space.

The model displays little sensitivity to variations of most of the parameters, demonstrating robustness within the defined parameter sub-space, Fig. 3-9. The model shows high sensitivity to parameters k_1, k_6, k_{14} and d_2, which correspond to production rate of type-B ARRs (k_1),

phosphorelay inhibition by X (k_6), production of the inhibitor X (k_{14}) and the diffusion rate of WUS (d_2). The first three parameters (k_1, k_6, k_{14}) are essential for the correct functioning of the reaction-diffusion system and correspond to the activity of the autocatalytic loop (k_1), inhibitory effect of the inhibitor (k_6) and the production rate of the inhibitor (k_{14}). The model shows the highest sensitivity to the diffusion rate of WUS d_2 which represents the ratio of WUS diffusion to type-B ARR diffusion. The direct effect of d_2 is to influence the width of the WUS expression peak. Additionally WUS diffusion along with L1 signal determines the expression of CLV3. This double effect of the WUS diffusion rate d_2 on both WUS and CLV3 expression domains explains why it is the most sensitive parameter. Other diffusion/degradation rates in the reaction-diffusion subnetwork do not directly affect the expression pattern of CLV3.

3.4.4 The L1 signal has to be confined to a few cell layers

By altering the hypothetical L1 signal we can identify some properties of this signal, which are essential for the correct behavior of the model. This can be used to assess the model hypothesis about the directional signal in the SAM, when a candidate for such a signal is identified. For simulations of the wildtype shown in Fig. 3-5, the L1 signal extends to only a few cell layers below the L1 layer as shown in Fig. 3-5G. We examined the scenario where the L1 signals extend farther down the meristem. This can be achieved either by increasing the diffusion rate of the signal and/or by decreasing its degradation rate. The extension of L1 signal results in enlargement of CLV3 domain and presence of CLV3 in the OC (compare Fig. 3-10A and Fig. 3-10B), which is never reported in wildtype. Therefore, the model predicts that in wildtype the directional signal originating in the L1 layer, is confined to the 3-4 uppermost cell layers, which is in good agreement with the spread detected for miR394 [91].

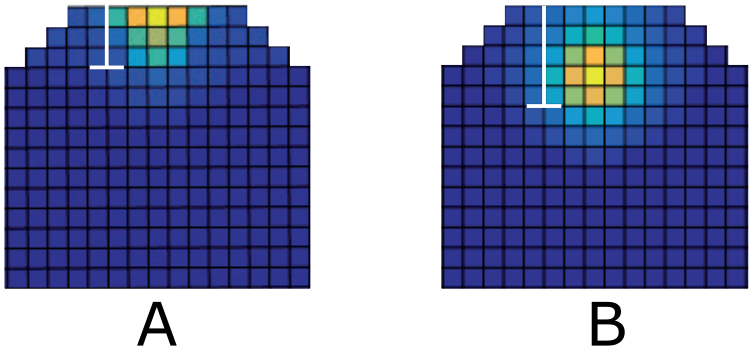

Figure 3-10: Extension of L1 signal beyond the first three cell layers; The white bar in the figures show the distance at which the concentration of the L1 signal drops to half of its initial concentration (a) CLV3 expression in wt. (b) CLV3 expression resulting from the extended L1 signal. the *CLV3* mRNA expression extends to organizing center. This has never been observed experimentally in the wildtype SAM, hence the model predict that L1 signal is confined to the upper three cell layers.

3.4.5 Reproduction of the *clv3* mutant expression patterns

In the *CLV3* mutant the WUS expression domain expands laterally. Additionally the concentration of WUS within its domain increases. The lateral expansion of WUS domain is accompanied by lateral expansion of the meristem as a whole [62]. Wether the WUS domain elongation happens as a result of meristem elongation or is the cause of it, or whether they are independent of each other, is not clear. In our simulations of the *clv3* mutant, the concentration of WUS increases within its domain and the expansion of the domain occurs in all directions, while the upward shifting of the WUS domain does not occur (Fig. 3-11). This could result from the static nature of the model which does not consider cell division and/or elongation.

3.4.6 Reproduction of the effect of laterally extending the meristem size

Graf *et al.* identified *mgol-4* mutant which is defective in shoot meristem development. In mature *mgol-4* plant, the meristem is enlarged and becomes fragmented into multiple apices, each containing a separate stem cell niche. We simulated this effect by laterally doubling the width of the meristem, as shown in Fig. 3-12. *In vivo*, the mutant exhibits other developmental defects and the enlarged SAM does not possess a smooth and uniform edge, but forms a rather

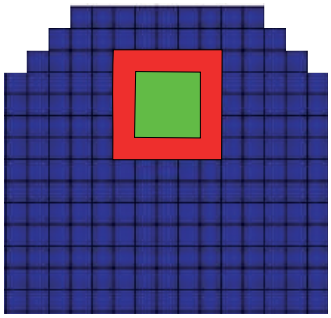

Figure 3-11: The effect of the clv3 mutation on WUS expression; green shows the extent of WUS expression in wildtype, and red shows WUS expression in the clv3 mutant. The expression zones are defined as cells that express WUS at the half maximum level of expression in the mutant or higher. In the mutant the concentration of WUS increases, this means the number of cells that express WUS at a high enough level to be considered within the expression zone, increases.

jagged and disorganized structure [103]. Our aim was to investigate whether the model, in general, is capable of generating multiple WUS centers in a larger domain. When the width of the domain is doubled, two WUS centers appear, the expression of WUS and CLV3 can be seen in Fig. 3-12A,B. This multiplication of the pattern in a larger domain, is a known characteristic of reaction-diffusion systems [104], and further demonstrated the competence of a reaction-diffusion system in modeling the WUS regulation within the SAM. Furthermore, the *jabba-ID* mutant of *Arabidopsis* exhibit enlarged and laterally expanded meristems, in some of which the formation of two distinct WUS centers and the laterally extended CLV3 domain can be observed [105]. These closely resemble our simulations results of CLV3 expression in a laterally extended meristem, shown in Fig. 3-12B.

3.4.7 The model exhibits regenerative ability of the meristem following laser ablation

Experimental observations show that after the removal of the OC and stem cell domain in the SAM of tomato via laser ablation, two new WUS centers form at the opposite sides of the ablation [60]. Starting from a wildtype expression pattern (Fig. 3-13A-B), we eliminated the WUS and CLV3 expressing cells. When the system again reaches a steady state, two new OCs and stem cell niches form at either side of the ablation site in a very similar manner to the

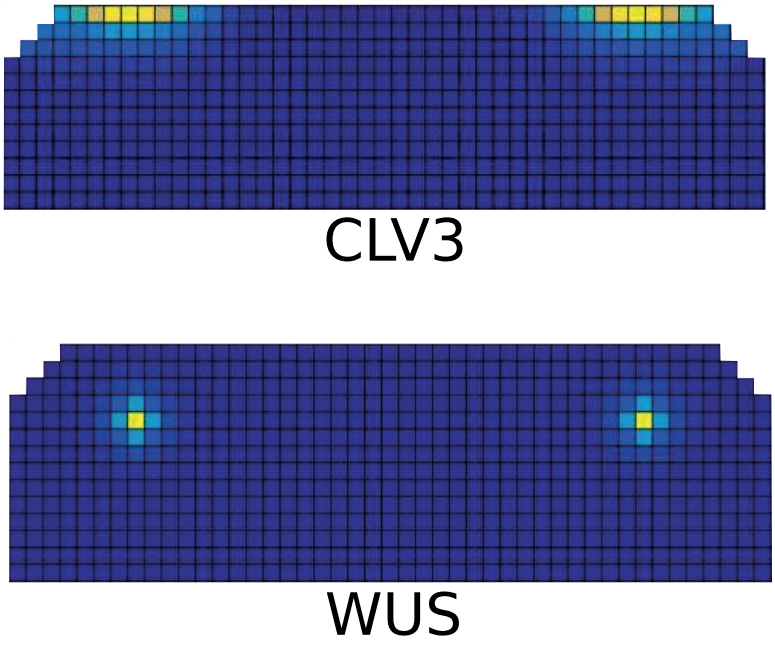

Figure 3-12: Expression of the molecules in the model, when meristem size is doubled laterally; (A) two separate WUS expression centers form, (B) CLV3 expression zones form above each WUS center.

experimental observation (Fig. 3-13C-D). Such regenerative ability is an essential property of the SAM. The model predicts the presence of CK signaling and AHK4 at newly formed WUS expression centers after ablation. To our knowledge the presence of AHK4 expression patterns and CK activity have not been analyzed in the SAM after laser ablation. We therefore performed laser ablation experiments and tested for recovery on the level of CK signaling.

3.4.8 Limitation of the CK response profile

For the proposed model it is only important that CK is limited to the upper 20-30 cell layers of the meristem, the actual process by which this is achieved is not important. As there is no experimental evidence that a diffusion or transport barrier - such as a Casperian strip - in this region exists, we analyze the consequences of the assumption that the CK profile is *not* limited by a physical barrier. Because no evidence for a directed transport of CK in the SAM exists, we consider the mobility of CK as a non-directional diffusion-like process. In this case

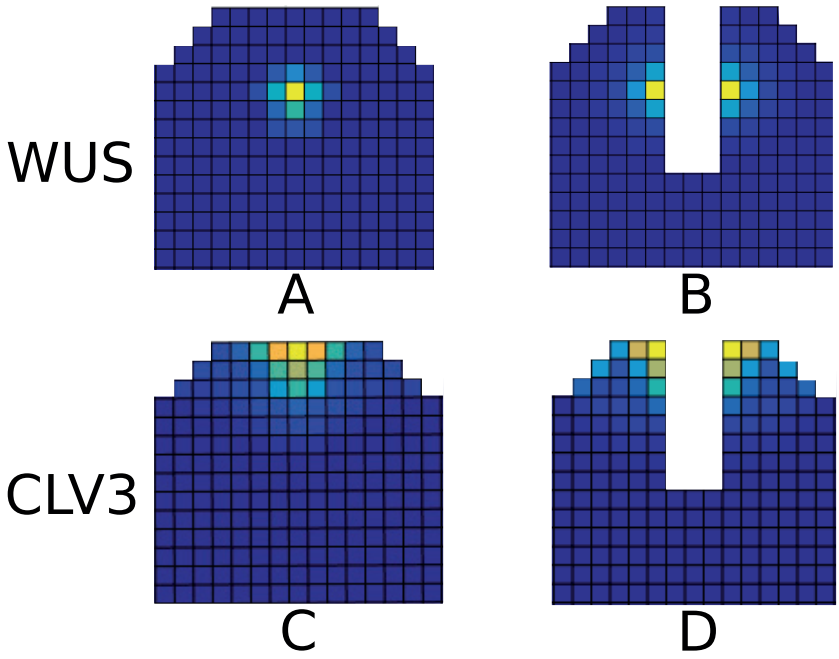

Figure 3-13: WUS and CLV3 expression patterns after *in silico* ablation; (A) and (C): the wildtype expression pattern of WUS and CLV3. (B) and (d): WUS and CLV3 expression patterns that form after ablation of the center of the SAM including the SCD and OC.

the CK profile is governed by three parameters: the size of the synthesis zone n_0, the average lifetime τ of a CK molecule and the effective diffusion rate D_{eff}. Unfortunately, for none of these parameters estimates are available. CK profile was experimentally measured to cover the first 25 cell layers of the meristem [82], i.e., the synthesis regime does not extend beyond this. It seems reasonable to limit it further to the actual meristem [99]. From this follows that $1 \leq n_0 \lessapprox 7$. The long-distance translocation of CKs is mediated by the xylem and the phloem and is experimentally investigated [106]. However, for this study the local short-distance mobility of CK across the plasma membrane and the cell wall is important, for which the mechanisms are not well understood [107]. The purine permease family and the equilibrative nucleoside transporter family have been proposed as candidates for CK transporters. While the first can transport free-base CKs in a proton-coupled manner the latter facilitate diffusion of nucleosides along a concentration gradient [108]. In any case, the mobility of CK in the

SAM is determined by its diffusion in the cytoplasm and the transport/diffusion across the cell boundaries, where the latter is likely to be the limiting process. In order to obtain an estimate for the upper limit for the effective diffusion rate in the SAM tissue we consider the diffusion of a molecule in the cytoplasm. Based on measurements in E. coli, we find as a rough estimate of the diffusion constant in the cytoplasm $D_{\text{eff}}^{>} \approx 241 \mu\text{m}^2\text{s}^{-1}$ [109, 110]. An estimate for the lower limit can be obtained by considering the diffusion of molecules within the cell wall [108]. We obtain for CK as lower limit $D_{\text{eff}}^{<} \approx 42 \mu\text{m}^2\text{s}^{-1}$. The degradation of CK is catalyzed by CK oxidase/dehydrogenase [99]. It appears that degradation is a highly regulated process, which makes it difficult to say something about the rate. To date the degradation rate of CK in the SAM has not been measured. Therefore, no further information is available. However, we can use these considerations to obtain an idea about the average lifetime of a CK molecule. For a given diffusion rate D_{eff} and a range n_0 of the synthesis zone the average degradation rate or life-time τ of CK follows from the limiting the profile to the upper 25 cell layers (see section 3.7.13). The resulting τ as a function of D_{eff} and n_0 is shown in Fig. 3-14. Due to the rough estimates available for the other parameters, there is of course a range for τ, but interestingly the deliberations above point towards a lifetime of CK of the order of a few minutes.

3.4.9 Role of advection

A simple physical picture for the CK transport inside the phloem is that of mass transport due to the bulk motion of a fluid (advection). The phloem starts several cell layers below the meristem [111, 112]. To study this problem we now divide the tissue into three zones: $x \leq x_0$: synthesis regime (synthesis + degradation + diffusion), $x_m \geq x > x_0$: diffusion regime (diffusion + degradation), and $x > x_m$, advection regime (diffusion + advection + degradation).

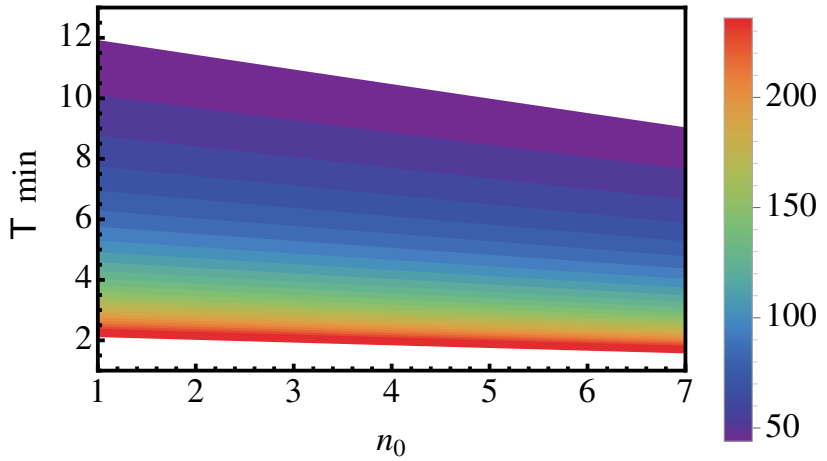

Figure 3-14: CK lifetime as a function of D_{eff} and n_0. The average lifetime τ of CK in minutes in the meristem and the extension n_0 in cell layers of the CK synthesis zone consistent with the observation of a CK profile covering the upper 25 cell layers of the meristem. The colorbar shows the chosen value of the effective diffusion constant of CK in the meristem tissue, ranging from $42\mu\text{m}^2\text{s}^{-1}$ to $241\mu\text{m}^2\text{s}^{-1}$ (see text).

This is in steady state described by the following set of equations:

$$
\begin{aligned}
D\frac{\partial^2\phi_1}{\partial x^2} - \lambda\phi_1 + \Gamma &= 0: \quad x \le x_0 \\
D\frac{\partial^2\phi_2}{\partial x^2} - \lambda\phi_2 &= 0: \quad x_m \ge x > x_0 \\
D\frac{\partial^2\phi_3}{\partial x^2} - v\frac{\partial\phi_3}{\partial x} - \lambda\phi_3 &= 0: \quad x > x_m \\
D\left.\frac{\partial\phi_1}{\partial x}\right|_{x=x_0} &= D\left.\frac{\partial\phi_2}{\partial x}\right|_{x=x_0} \\
D\left.\frac{\partial\phi_2}{\partial x}\right|_{x=x_m} &= D\left.\frac{\partial\phi_3}{\partial x}\right|_{x=x_m} - v\phi_3(x_m)
\end{aligned}
$$

In addition we require that the system is closed at $x = 0$ and that the solution is continuous and vanishes at infinity:

$$
\left.\frac{\partial\phi_1}{\partial x}\right|_{x=0} = 0;\ \phi_1(x_0) = \phi_2(x_0);\ \phi_2(x_m) = \phi_3(x_m);\ \lim_{x\to\infty}\phi_3(x) = 0.
$$

In order to further analyze this, we rescale length again with the typical cell size L. Also, we rescale the concentrations ϕ_i with $\phi_0 = \Gamma/\lambda$ and finally arrive at:

$$\begin{aligned}
l^2\frac{\partial^2\phi_1}{\partial\tilde{x}^2} - \phi_1 + 1 &= 0: \qquad \tilde{x} \le n_0 \\
l^2\frac{\partial^2\phi_2}{\partial\tilde{x}^2} - \phi_2 &= 0: \qquad \tilde{x}_m \ge \tilde{x} > n_0 \\
l^2\frac{\partial^2\phi_3}{\partial\tilde{x}^2} - l_a\frac{\partial\phi_3}{\partial\tilde{x}} - \phi_3 &= 0: \qquad \tilde{x} > \tilde{x}_m \\
\left.\frac{\partial\phi_1}{\partial\tilde{x}}\right|_{\tilde{x}=n_0} &= \left.\frac{\partial\phi_2}{\partial\tilde{x}}\right|_{\tilde{x}=n_0} \\
\left.l^2\,\frac{\partial\phi_2}{\partial\tilde{x}}\right|_{\tilde{x}=\tilde{x}_m} &= \left.l^2\,\frac{\partial\phi_3}{\partial\tilde{x}}\right|_{\tilde{x}=\tilde{x}_m} - l_a\phi_3(\tilde{x}_m)
\end{aligned}$$

with $l_a = v/(L\lambda)$. For large Péclet numbers $l_a/l^2 = vL/D \gg 1$ the flux continuity equation at $\tilde{x} = \tilde{x}_m$ simplifies to $\phi_3(\tilde{x}_m) = 0$ and by using the continuity of the solution we find: $\phi_2(\tilde{x}_m) = 0$, which yields a closed set of equations for $\tilde{x} \le \tilde{x}_m$. For a phloem flux of $v = 50\mu$m/s [113] the Péclet number would be roughly in the range $6 > l_a/l^2 > 1$. Using the approximation for large Péclet numbers, we find:

$$\begin{aligned}
\phi_1(\tilde{x}) &= 1 - \cosh\left(\frac{\tilde{x}}{l}\right)\frac{\cosh\left(\frac{\tilde{x}_m - n_0}{l}\right)}{\cosh\left(\frac{\tilde{x}_m}{l}\right)} && \tilde{x} \le n_0 \\
\phi_2(\tilde{x}) &= \sinh\left(\frac{\tilde{x}_m - \tilde{x}}{l}\right)\frac{\sinh\left(\frac{n_0}{l}\right)}{\cosh\left(\frac{\tilde{x}_m}{l}\right)} && \tilde{x}_m \ge \tilde{x} > n_0 \\
\phi_3(\tilde{x}) &= 0 && \tilde{x} > \tilde{x}_m
\end{aligned}$$

In adult plants the closest distance to the phloem was measured to be roughly $220\,\mu$m [111, 112], which translates to $\tilde{x}_m \approx 44$. Corrections to the estimate of the lifetime of CK are of the order $\mathcal{O}(e^{-2\tilde{x}_m/l_0})$, where l_0 is the root of the equation $Ck_{i=25j}/Ck_{i=1j} = 1/2$ without advection, i.e., $l_a = 0$. Using $\tilde{x}_m \approx 44$ and $l_0 \approx 32$ we find $e^{-2\tilde{x}_m/l_0} \approx 0.06$. Taken together the results suggests that advection via phloem, at a distance of roughly $220\,\mu$m, hardly affects the CK profile in the meristemic zone, which is rather defined by the diffusion length scale. However, in young plants the situation is quite different. Unless the the diffusion length is modified during the growth process, the meristemic zone defined by the CK profile would be unrealistically

large. The close proximity of the phloem to the meristemic region (from $0 - 10\,\mu$m for a mature embryo [114] to about $80\,\mu$m for a 11 days old seedling [111] suggests that advection via the phloem can dictate the length scale of the CK profile and hence the size of the meristemic region in a young plant.

3.4.10 Microsurgical and laser ablation experiments

The model assumptions presented here suggest that the WUS expression in the OC is maintained via a reaction-diffusion network at the CK expression level. Laser ablation and microsurgical studies have shown that upon removing the WUS expressing cells the WUS expression is regenerated [60]. Our model further predicts that this recovery takes place at the level of CK signaling. In order to test this hypothesis, we performed microsurgical and laser ablation experiments, where we removed the cells within meristem that express the GFP under the *TCS* marker gene. We also performed the same experiment with GFP expressed under *WUS* promoter. In our initial trials, we observed that the expression of TCS fades away following the dissection of the meristem. This could be due to the lack of CK supply through the stem to the meristem. In order to compensate for the lack CK supply via the stem and to aid the visualization of the expression of TCS in the days following the dissection, we cultured the meristems after dissection in a CK containing medium. Our results demonstrate that the CK signaling domain within the meristem regenerates within 1-2 days following microsurgical ablation as shown Fig. 3-15A-C, in a similar manner and time-frame as WUS expression, Fig. 3-15D-F. Furthermore, we carried out ablation experiments on plants expressing *pclv3*-GFP. Upon removing the organizing center and the CLV3 expressing cells, it was observed that CLV3 becomes visible 3 days after the ablation, Fig. 3-15G-I. The time-frame of recovery of CLV3 compared to WUS and TCS is in agreement with the model assumptions.

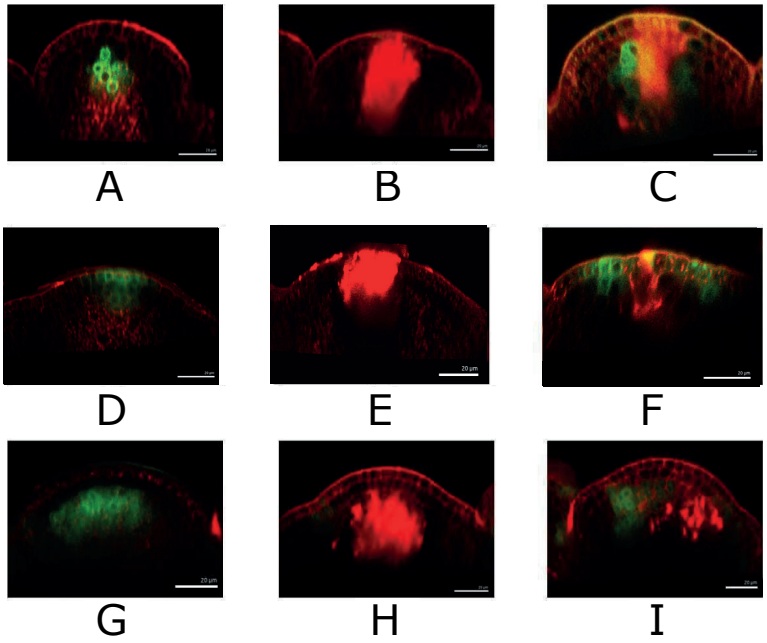

Figure 3-15: Laser ablation of WUS, TCS and CLV3; WUS-GFP promoter fusion expression before (A), just after (B) and 1 d after (C) laser ablation. TCS expression before (D), just after (E) and 1 d after (F) laser ablation. CLV3 expression before (G), just after (H) and 2 d (I) after laser ablation. The green signal is WUS-GFP in a, b, c, TCS-GFP in d, e, f, CLV3 in g, h, i. Red signal is propidium-iodide (PI)-stained cell wall or laser ablated cells.

3.5 Discussion

WUS is a major component of SAM development and stem cell homeostasis. Recent experimental evidence has revealed a diverse and extensive network comprising genes and hormones that contribute towards regulation of the SAM. Despite these findings, and several modeling efforts, it is still unclear how the WUS expression domain is restricted and centered within the SAM. We argue that the patterning and regulation of WUS within the SAM cannot be well understood without addressing the cell lineage-independent nature of it. The current knowledge, puts CK forward as a major factor in positioning and patterning of the SAM. We developed a model strictly based on the known mechanism of CK reception and signaling via the AHK4 receptor. Our experimental results, in agreement with earlier findings, show that upon laser ablation of OC and stem cell niche, the meristem is able to regenerate the WUS expressing cells as well as

stem cells. In addition we demonstrate that the CK signaling domain within the SAM shows similar regenerative capabilities. Considering the time-frame of the recovery of WUS and TCS expression after ablation and the current understanding of the role of CK signaling in regulating the SAM activity, the experimental results suggest that the CK signaling could be the basis of the regenerative ability of the SAM as a whole. The time-frame of the regeneration of CLV3 compared to WUS and TCS, demonstrated that the recovery of CK signaling and subsequently the WUS expression is sufficient for the recovery of stem cell population.

Concepts such as L1 and factor X have been consistent features of activator-inhibitor-based modeling of SAM and their role in the work presented here is in principle same as earlier works. The main contribution of this work lies in the observation that some known components of CK signaling network have the capability of functioning as an activator-inhibitor system. By incorporating our assumptions of a diffusing inhibitor, a feedback loop involving the type-B ARRs and AHK4 and L1 signal, we demonstrate the potential of the CK signaling network in generating patterns within the SAM, in close agreement with the experimental observations. In addition our experimental results suggest that specification of OC including its self-organizing properties can arise, at least in part, via CK signaling. If type-A ARRs are assumed to be highly mobile, the intermediate factor X is not required and the model can function with type-A ARRs directly inhibiting the phosphorylation of type-B ARRs. We explicitly tested this scenario and observed, with adjustment of parameters the model is capable of producing the same patterns. In case the type-A ARRs do not fulfill the requirements, the proposed intermediate factor X is necessary. To our knowledge the studies focused on genetic regulation of the SAM do not put forward a candidate for factor X. While inhibiting type-B ARRs, factor X is predicted to have an overlapping peak and expression domain with type-B ARRs. At first sight, AHP6, a well-known inhibitor of CK signaling [101] appears as a likely candidate. However its expression pattern does not match the predicted pattern for factor X [115, 116]. In the model factor X has a higher diffusion rate than other molecules, including the small CLV3 peptide. This hints at factor X being an even smaller molecule, perhaps a micro-RNA (miRNA). miRNA165/166, are mobile

signaling molecules that suppress CK signaling via inhibition of CK production [117, 118]. However the expression pattern of these molecules is very different from the predicted expression of factor X [119]. It remains to be seen whether the new and active area of research on the role of miRNAs in plant genetic regulation would identify an experimental counterpart for this hypothetical molecule.

The inhibition of upstream CK signaling via type-A ARRs is essential for correct model output. This is because the aforementioned interaction constitutes a part of the core activator-inhibitor motif. In contrast the type-A ARR inhibition of type-Bs via competition for phosphate is not necessary for correct model functionality, see Fig. 3-16. Our simulations show that the model can produce the corrects output in presence and absence of phosphate competition. While verification of the mechanism of type-A ARRs inhibitory effects are out of the scope of the model, the results suggest that the upstream inhibition is the main mechanism in meristem patterning.

One important ingredient of the model is the observation that the CK concentration profile is limited to the upper 20-25 cell layers. The exact cause of this is not important for the model to work, but as there is no evidence of a diffusion barrier for CK, we explored the consequences of a diffusion-like transport of CK within the tissue. Because the determining parameters for the CK profile are unknown, we cannot limit the synthesis regime of CK, besides the plausible assumption that CK synthesis is confined to the SAM. However, based on these considerations and using estimates for the effective diffusion rate of CK we conclude that the average lifetime of a CK molecules within the SAM is of the order of a few minutes. A further consequence of the model is that the size of the meristem might be determined by two distinct physical mechanisms. The model suggests that in adult plants the size of the SAM is governed by the length scale of CK diffusion, while in young plants it is determined by the distance from the L1 to the phloem.

We have shown that a combination of boundary driven patterns - CK and L1 signal acting as morphogenes - and a reaction diffusion system including AHK4 and its assumed inhibitor can

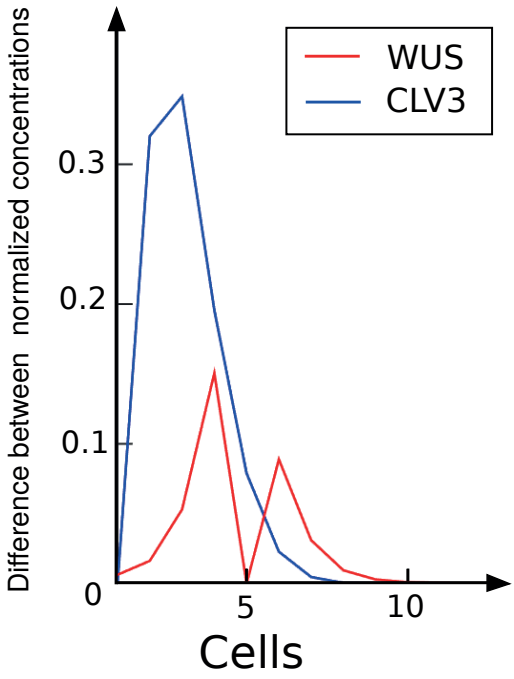

Figure 3-16: Phosphate competition between type-B and type-A ARRs does not significantly affect the model output. The difference in model simulation of WUS and CLV3 expression, when phosphate competition between ARRs is absent from the model. The expression profile of WUS and CLV3 in absence of phosphate competition were subtracted from the corresponding wildtype expression profile. The expression profiles were normalized to maximum levels in each case and the absolute difference between the two was calculated. To simulate the absence of phosphate competition, parameters k_4 and k_5 are set to zero. Model output is not significantly changed in absence of the phosphate competition.

account for a variety of observed phenomena regarding the SAM. The reorganization of the SAM after laser ablation and the appearance of multiple OCs upon lateral extension of the SAM closely resemble the properties of a reaction diffusion system. Our results suggest that both a short and a long range morphogene are required for establishment and regulation of WUS and CLV3 expression patterns within the SAM. The long ranged (on the scale of the SAM) CK confines the WUS expression peak to the SAM, while the short ranged L1 signal is required in order to restrict the expression of CLV3. We show that L1 signal, originating from the L1 layer and diffusing downwards, can adequately explain the induction of CLV3 expression in a specific location at the tip of the SAM. The model predicts that the signal does not diffuse past the first few cell layers beneath the L1. The recently characterized miR394, produced at the L1

layer and necessary for establishment and regulation of stem cells by WUS, provides a suitable candidate for the role of L1 signal in the SAM.

The proposed minimal model focuses on specific aspects in order to understand the core regulatory concepts and is not expected to capture the complex biological system in its full detail. This is specifically true for redundancy, which is a common feature of many biological systems. A survey of literature reveals a high degree of redundancy within the CK sub-network. There are several types of CKs in plants. Many ARRs have similar expression patterns and are thought to be at least partially redundant [77]. Single and even multiple mutants deficient in CK biosynthesis do not show significant SAM phenotypes [120, 121]. The same is true for many type-A and type-B ARR genes. Therefore, single mutant phenotypes predicted by the reductionist model presented here, cannot be expected to correspond to the observed single mutant phenotypes. However, the model is expected to exhibit systemic behavior that could be used to assess the hypothesis under study. Furthermore, the model makes specific predictions that can be utilized to design experiments to test the model hypothesis and to further clarify underlying mechanism of gene expression patterning within the SAM. In summary, we show that regulation of the CK receptor AHK4, through a reaction-diffusion mechanism can plausibly account for an array of observed phenomena regarding WUS patterning and thus providing one possible answer to the question of how the organizing center is centered.

3.6 Acknowledgments

We thank J. Traas, B. Müller and V. Reddy for providing seed materials and Y. Deb for advice regarding the laser ablation experiments. We thank Thomas Laux for stimulating discussions and support in the initial phase of this project.

CHAPTER 4

Integration of growth and patterning during vascular tissue formation in Arabidopsis

Adopted form the publication in Science, Aug 2014
DOI: 10.1126/science.1255215

Bert De Rybel[1,*], Milad Adibi[2,3,4,*], Alice S Breda[1,†], Jos R. Wendrich[1], Margor E. Smith[1], Ondřej Novăk[5,6], Nobutoshi Yamaguchi[7], Saiko Yoshida[1], Gert Van Isterdael[8,9], Joakim Palovaara[1], Bart Nijsse[4], Mark V. Boekschoten[10,11], Guido Hooiveld[10], Tom Beeckman[8,9], Doris Wagner[7], Karin Ljung[5], Christian Fleck[4,‡], and Dolf Weijers[1,‡]

[1] *Laboratory of Biochemistry, Wageningen University, Dreijenlaan 3, 6703HA Wageningen, the Netherlands.*

[2] *LifeGlimmer GmbH, Markelstrasse 38, 12163 Berlin, Germany.*

[3] *Albert-Ludwigs-University Freiburg, Faculty of Biology, Plant Biotechnology, Schaenzlestrasse 1, D-79104 Freiburg, Germany.*

[4] *Laboratory of Systems and Synthetic Biology, Wageningen University, Dreijenlaan 3, 6703HA Wageningen, the Netherlands.*

[5] *Umeå Plant Science Centre (UPSC), Department of Forest Genetics and Plant Physiology, SLU, SE-901 83 Umeå, Sweden.*

[6] *Laboratory of Growth Regulators, Centre of the Region Haná for Biotechnological and Agricultural Research, Palacký University and Institute of Experimental Botany AS CR, ˇlechtitelů 11, CZ-78371 Olomouc, Czech Republic.*

[7] *Department of Biology, University of Pennsylvania, Philadelphia, PA 1901046084, USA*

[8] *Department of Plant Systems Biology, VIB, Technologiepark 927, 9052 Gent, Belgium.*

[9] *Department of Plant Biotechnology and Bioinformatics, Ghent University, Technologiepark 927, 9052 Gent, Belgium.*

[10] *Division of Human Nutrition, Wageningen University, Dreijenlaan 2, 6703HA Wageningen, the Netherlands.*

[11] *TI Food and Nutrition, 6703HA Wageningen, the Netherlands.*

[*] *These authors contributed equally to this work.*

[‡] *Corresponding author. E-mail: dolf.weijers@wur.nl (D.W.); christian.fleck@wur.nl (C.F.)*

4.1 Introduction

Because plant cells cannot migrate during development, control of cell division orientation and simultaneous tissue patterning during early growth is vital to create a functional three-dimensional (3D) structure. The basic body plan of the plant is determined during early embryogenesis. The root vascular tissues develop from four provascular initial cells (Fig.4-1) that undergo several rounds of oriented, periclinal cell divisions to create a patterned vascular bundle by the end of embryogenesis [122, 123]. The vascular bundle then contains xylem cells marked by high auxin signaling and flanking zones of procambium cells characterized by high CK signaling [124] from which the phloem tissues will differentiate post-embryonically. Although growth through oriented cell divisions and pattern formation are thus crucial for normal development, it is yet unknown how these intertwined processes are regulated and if this occurs through distinct or overlapping pathways. Here, we combined experimental and theoretical approaches to unravel the integration of vascular growth and patterning during Arabidopsis embryogenesis.

4.2 *LOG4* is a direct TMO5/LHW target gene

The TARGET OF MONOPTEROS5/LONESOME HIGHWAY (TMO5/LHW) basic helix-loop-helix (bHLH) transcription factor dimer is a rate-limiting regulator of periclinal cell divisions [125]. Mutants show a reduction in vascular tissue size due to loss of periclinal division frequency, whereas ectopic coexpression of TMO5 and LHW can trigger this type of division in any cell type of the root [125]. The expression domains of TMO5 and LHW overlap in young xylem cells that strongly correlate with the zone in which periclinal divisions occur. However, xylem cells do not themselves divide periclinally, which suggests that the TMO5/LHW dimer promotes these divisions by inductive signaling toward neighboring procambium cells. Indeed, TMO5/LHW misexpression induces excess divisions both cell-autonomously and

non–cell-autonomously, suggesting that these transcription factors trigger periclinal cell division through a yet unknown diffusible signal [125].

Given that TMO5/LHW is a transcription complex, we sought to identify this unknown signal,

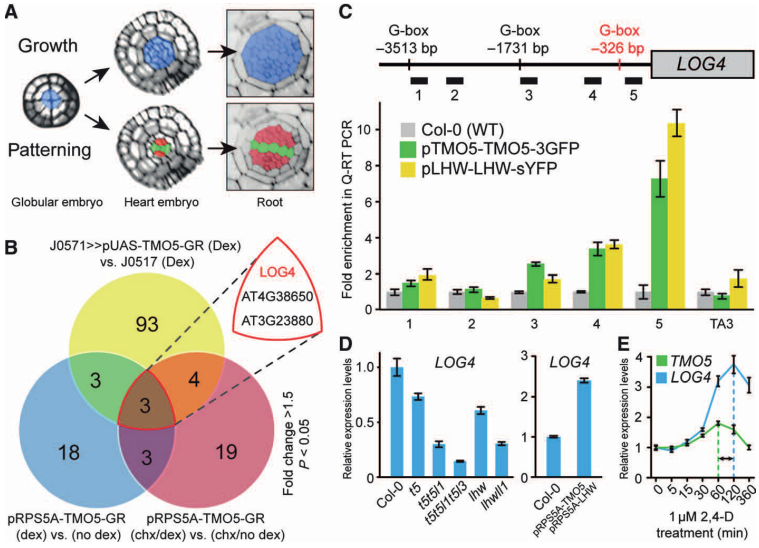

Figure 4-1: *LOG4* is a direct target of the TMO5/LHW dimer. (A) Growth (blue) and patterning (red: cambium; green: xylem) occur simultaneously in vascular tissue during embryogenesis. (B) Combinatorial microarray analysis, identifying *LOG4* as putative target gene of TMO5. (C) ChIP-qPCR experiment shows direct binding of TMO5 and LHW fusion proteins close to a G-box (−326 bp) of the *LOG4* promoter. (D) Relative qRT-PCR expression of *LOG4* in mutants or TMO5/LHW-OE compared to wild type (WT) (Col−0). (E) Relative expression levels (qRT-PCR) of *TMO5* and *LOG4* in roots upon 1 μM 2,4-dichlorophenoxyacetic acid (2,4−D) treatment for the indicated time. Error bars in (C) to (E) indicate SE.

or components of its biogenesis, through determining the direct transcriptional targets. We devised a combinatorial transcript profiling approach using independent, rapidly inducible TMO5 versions (see Materials and Methods in appendix A3 for detailed information). Only three genes were significantly induced by TMO5 in all independent experiments ($P < 0.05$, fold change >1.5) (Fig. 4-1B and table B2), and their regulation by TMO5 was confirmed by quantitative reverse transcription–polymerase chain reaction (qRT-PCR) (Fig. B1). One of these genes encodes LONELY GUY 4 (LOG4), an enzyme involved in the final biosynthesis step of CK [126, 127]. Given the previously established importance of CK in root vascular

tissue patterning [128], we focused our attention on this gene. Chromatin immunoprecipitation (ChIP) confirmed direct binding of both TMO5-3GFP (triple green fluorescent protein) and LHW-YFP (yellow fluorescent protein) to the same upstream fragment of the gene (Fig. 4-1C). This coincided with a predicted bHLH-binding G-box (CACGTG) located 326 base pairs (bp) upstream of the *LOG4* start codon (Fig. 4-1C). LOG4 transcripts were reduced in tmo5 and lhw mutant roots and increased upon TMO5/LHW misexpression (Fig. 4-1D), suggesting that TMO5/LHW are indeed required for LOG4 gene expression. TMO5 is a direct auxin response gene [129], and as expected, *LOG4* was also induced by auxin, but with delayed induction kinetics (Fig. 4-1E).

TMO5 expression marks the first four vascular founder cells in the globular embryo [128]. Consistent with direct regulation by the TMO5/LHW dimer, *LOG4* transcript (Fig. 4-2A and Fig. B2) and a p*LOG4*-n3GFP reporter (Fig. 4-2, B and C) were expressed in these same cells. Later, *LOG4* expression was confined to the TMO5/LHW domain in the xylem (Fig. 4-2, G and H). Because the *LOG4* expression domain was extended in pRPS5A-TMO5/pRPS5A-LHW misexpression (TMO5/LHW-OX) roots (Fig. 4-2, I and J) and absent in the xylem domain of lhw roots (Fig. 4-2, K and L), TMO5/LHW is a key transcriptional input. Nonetheless, expression of *LOG4* in xylem pole pericycle and xylem pole endodermis cells (Fig. 4-2H) suggests additional, TMO5-independent post-embryonic input. Together, these outcomes identify *LOG4* as a direct target gene of the TMO5/LHW transcription complex.

4.3 TMO5/LHW controls CK biosynthesis through *LOG4*

LOG proteins catalyze a rate-limiting step in CK biosynthesis [126,127], and thus the TMO5/LHW dimer may act by promoting CK biosynthesis. Indeed, concentrations of several CK species were reduced in *tmo5 t5l1* mutant roots, whereas most CK species were increased in TMO5/LHW-OX roots (Fig. 4-3A and table S2). In line with these elevated CK concentrations, TMO5/LHW-OX

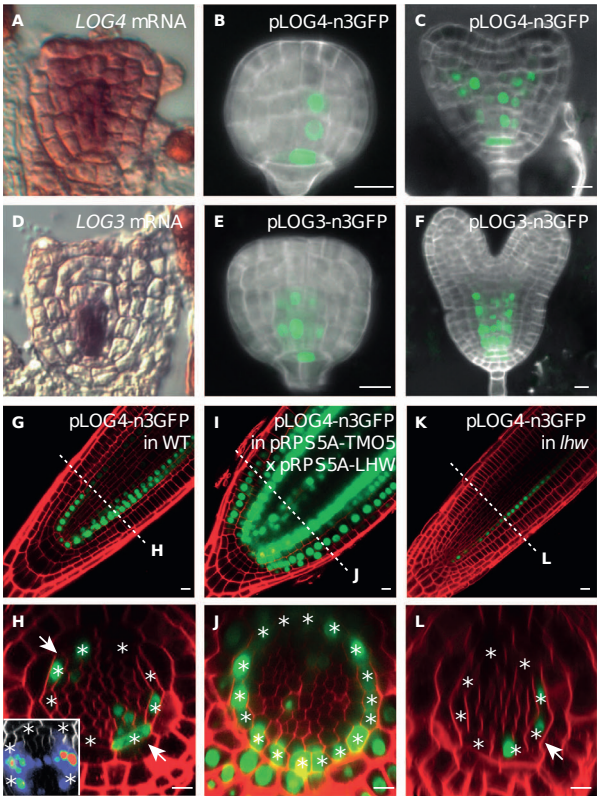

Figure 4-2: *LOG4* expression depends on TMO5/LHW. (A to F) *In situ* hybridization (A and D) and pLOG-n3GFP reporter expression (B, C, E, and F) of *LOG4* and *LOG3* during embryogenesis. (G to L) Expression of p*LOG4*-n3GFP reporter in post-embryonic root in WT (G and H), TMO5/LHW-OE (I and J), and lhw mutant (K and L). Inset in (H) represents a 3D stack cross section showing *LOG4* expression in false color scale across the entire xylem axis. Asterisks indicate endodermis; arrows indicate xylem. Roots are counterstained with FM4-64. Scale bars, 10 μm.

plants showed a strong postembryonic shoot phenotype, including ectopic leaf outgrowths (Fig. B3) that resembled CK-overproducing plants [129]. We next used gene expression reporters to determine if TMO5/LHW-dependent CK biosynthesis generates a transcriptional response. Whereas the synthetic CK response reporter pTCSn-GFP [101] was active only in the root cap and vascular initial cells in wild-type roots (Fig. 4-3B), it was ectopically activated throughout TMO5/LHW-OX roots (Fig. 4-3C). Likewise, the CK-repressed pAHP6-GFP reporter [130] was down-regulated upon TMO5/LHW misexpression (Fig. 4-3, D and E). Additionally, protoxylem differentiation was inhibited in TMO5/LHW-OX and *LOG4* misexpression roots (Fig. 4-3, H

and I), indicative of increased CK activity (Fig. 4-3, F and G) [130]. Hence, the TMO5/LHW complex triggers CK biosynthesis via inducing *LOG4* expression.

We next addressed the biological significance of LOG-dependent CK activity for TMO5/LHW

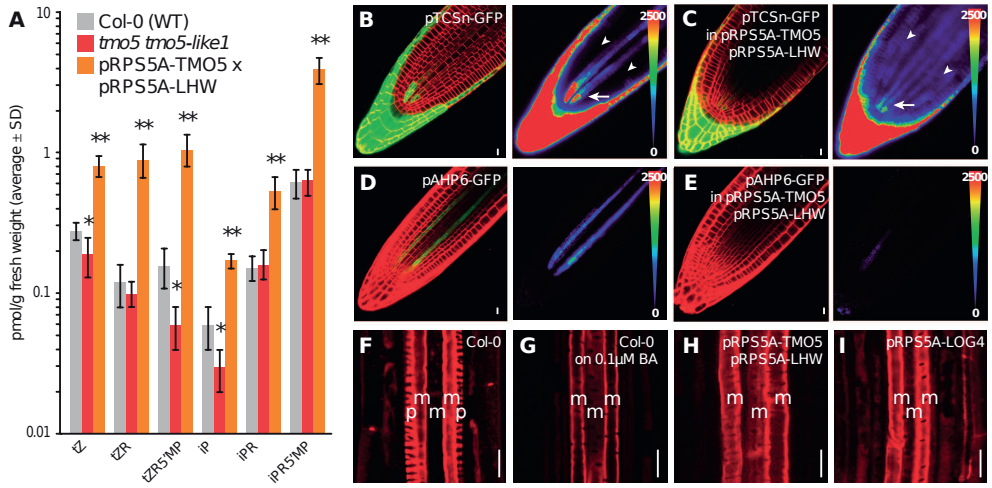

Figure 4-3: TMO5/LHW triggers CK biosynthesis. (A) Abundance of CK species in roots of t5t5l1 double mutant and double misexpression lines compared to WT (Col-0) (t test: *P < 0.05, **P < 0.001). (B to E) Expression of the pTCSn-GFP (B and C) and pAHP6-GFP (D and E) reporters in WT and TMO5/LHW-OX root tips. Right images show false color scales of the left image. (F to I) Basic fuchsin-stained roots of WT (Col-0), WT treated with 0.1 μM benzyladenine (BA), TMO5/LHW-OX, and *LOG4* misexpression (m, metaxylem; p, protoxylem). Error bars in (A) and (B) indicate SE. Images in (B) to (E) are counterstained with FM4-64. Scale bars, 10 μm.

function in promoting periclinal division and vascular tissue development. Consistent with a requirement for CK response, excess TMO5-induced periclinal cell division was suppressed in the *wol* receptor mutant (Fig. 4-4, A to F) [131]. *LOG4* single mutants did not show clear vascular defects (Fig. B3A-C), but this gene is member of a family of nine members (*LOG1* to *LOG9*) that has been shown to act redundantly in CK biosynthesis [126, 127]. We found that, indeed, CK-dependent pTCSn-GFP expression was absent in vascular precursors in the *log*1234578 heptuple mutant roots, but that expression could be restored by CK treatment (Fig. 4-4, G to J). Hence, *LOG* function is collectively required for CK biosynthesis in vascular tissue, which is reflected in defective embryonic vascular tissue development (Fig. B4A-B) and patterning (Fig. B4C) in this mutant. To determine which of the LOG genes may act

redundantly with *LOG4*, we first determined the expression patterns of all LOG genes. Only LOG3, LOG4, and LOG7 were consistently detected in young vascular tissues (Fig. 4-4, D to F, and Fig. B5) [126]. We therefore introduced the log3 log4 log7 triple mutant [132] into the TMO5/LHW-OX line and found this to suppress excess periclinal cell division (Fig. 4-4K). The partial suppression in this triple mutant suggests contributions of other LOG genes because several were up-regulated in a *log4* mutant (Fig. B4D), probably through CK-dependent repression (Fig. B4E). We next tested if CK activation is not only required but also sufficient for TMO5/LHW-dependent periclinal cell division. Mutations in LHW, as well as in TMO5 and TMO5-LIKE1 (T5L1), reduce vascular cell file numbers and lead to a switch from diarch to monarch pattern [125, 132]. Treatment of *lhw* and *t5t5l1* mutants with CK was sufficient to increase the number of periclinal divisions, revert to diarch patterns in both mutants, and even rescue cell number in the *lhw* mutant to wild-type levels (Fig. 4-4, L to R). In summary, these data suggest that *LOG*-derived CK is a major contributor to the vascular function of TMO5/LHW.

4.4 A model of vascular tissue formation

In addition to its function in vascular periclinal cell division, CK is also essential for patterning the vascular tissue into distinct domains, comprising the xylem axis with high auxin signaling and the flanking cambial domains with high CK signaling [124]. Thus, auxin-CK interactions appear to underlie both growth and patterning, and a key question is how these are coordinated. Previously, a phloem source of CK was postulated in the postembryonic root [133], but no functional phloem exists before seed germination [122], and recent modeling suggests that the phloem source may not provide positional information [134]. We therefore explored whether the auxin-MP-TMO5/LHW-LOG4-CK module could have a dual role and account for both patterning and growth using a computational approach.

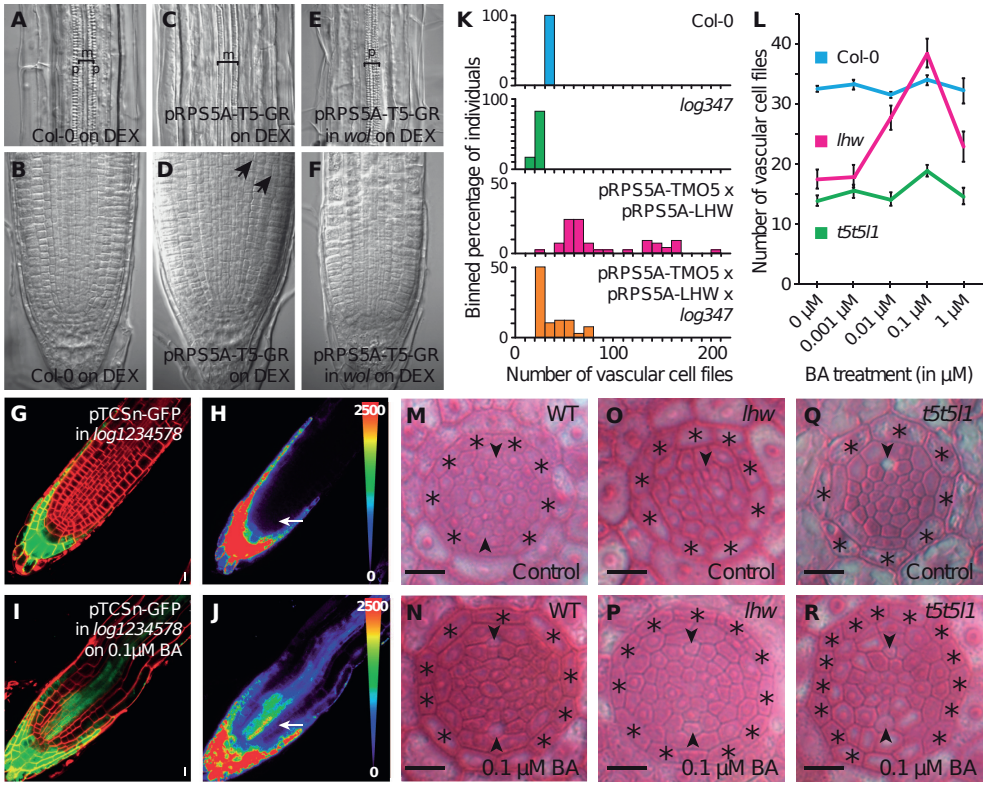

Figure 4-4: CK activation mediates TMO5/LHW activity. (A to F) Mature roots (top) and primary root meristems (bottom) of WT (Col-0), pRPS5A-TMO5-GR, and pRPS5A-TMO5-GR in wol mutant background; grown on 10 μM dexamethasone (DEX). Arrows indicate ectopic periclinal cell division (m, metaxylem; p, protoxylem). (G to J) pTCSn-GFP expression in log1234578 mutant without (G and H) or with (I and J) BA treatment. (H) and (J) are false color images of (G) and (I), respectively (counterstained with FM4-64). (K) Quantification of the distribution of vascular cell file number in roots of the lines indicated. (L) Number of vascular cell files in WT (Col-0), lhw, and t5t5l1 mutant backgrounds upon BA treatment (concentration as indicated). Error bars indicate SE. (M to R) Histologic cross sections of WT (Col-0), lhw, and t5t5l1 mutant roots grown without (control) or with 0.1 μM BA. Arrows indicate phloem poles. Scale bars, 10 μm.

4.4.1 Reaction network

We employ a reductionist modeling approach; that is we aim for a minimal set of assumptions and model components that can address the biological question at hand. Our model aims to test whether the identified genetic pathway, in which auxin triggers local CK production through MP, TMO5/LHW and LOG4, can account for stable patterning of the vascular tissues during embryonic growth. This entails a bilaterally symmetric pattern containing a central axis with

high auxin signaling (xylem cells), and two flanking zones with high CK signaling (cambial cells) [135]. In the model, auxin concentration is a proxy for auxin signaling; hence the xylem axis is characterized by relative high concentration of auxin. The model further incorporates the following facts and assumptions:

- In our mathematical model (Fig. 4-8A), the auxin-MP-TMO5/LHW-LOG4-CK module is represented as a set of ordinary differential equations mapped to a growing cellular grid using the VirtualLeaf software [9]. Because of the highly linear pathway, MP, TMO5/LHW, and LOG4 intermediates are not explicitly modeled, and thus in the model, auxin directly promotes CK production.

- Auxin levels in cells are determined by basal synthesis and degradation activity, as well as by passive diffusion and PIN-mediated active transport. (ii) PIN levels are subject to regulation by auxin and CK in addition to fixed synthesis and degradation [51].

- CK cell-autonomously inhibits PIN localization at the membrane [136], as has been shown for PIN1, the dominant PIN expressed in embryonic vasculature [136, 137]. We thus simplify the redundant PIN gene family [45, 137] by a representative "general PIN" that has PIN1-like properties. (iii) CK levels are promoted by auxin, and further depend on degradation and passive diffusion across membranes.

- Even though xylem cells produce CK, only the neighboring cambial cells respond by undergoing periclinal divisions. Thus, the CK-producing tissues do not respond to CK themselves. To capture this, we distinguish between CK and CK response. CK response is inhibited by auxin, as has been shown experimentally [116, 130].

- CK promotes periclinal division, which is represented in the model by lowering the cell size at which cells undergo division.

- By default, cells divide over their shortest axis once they double their area. CK signaling inside a cell lowers the threshold area for division thus increasing cell division rate [9].

- Auxin-dependent PIN dynamics are adopted from [63], as implemented in VirtualLeaf [9].
- There is an asymmetric flow of auxin towards the source cells due to the PIN protein topology in overlying cells (Fig. 4-8F-I and Fig. 4-9A,B). This is reflected in an increased auxin production rate of the two source cells.
- We assume that the cells with higher auxin input are fixed relative to the geometry of the tissue. This means if one of these cells divide, the daughter cell closer to the pericycle cells retains the higher auxin input, while the other daughter cell produces auxin at the same rate as non-source cells.
- Pericycle and endodermis cells divide along the axis that connects their centers to the center of the tissue. This is based on the observed division planes of these cells during vascular development [138].

4.4.2 Model Equations

The reaction network shown in Fig. 4-8A is described by the following five ordinary differential equations for each cell with cell index i:

$$\frac{dA_i}{dt} = k_1\chi_i - k_2 A_i + \frac{k_3}{a_i}\hat{D}A_i + \frac{k_4}{a_i}\sum_{j\in\mathcal{N}_i} l_{ij}\left(\frac{P_{ij}A_j}{1+\frac{A_j}{k_5}} - \frac{P_{ji}A_i}{1+\frac{A_i}{k_5}}\right) \tag{4.14}$$

$$\frac{dP_i}{dt} = k_6 - k_7 P_i + \sum_{j\in\mathcal{N}_i}\frac{l_{ij}}{a_i}\left(k_{20}P_{ij} - \frac{k_{15}P_iA_j}{\left(1+\frac{P_i}{k_{16}}\right)\left(1+\frac{A_j}{k_{17}}\right)\left(1+\frac{k_{18}\left(\frac{C_i}{k_{19}}\right)^p}{1+\left(\frac{C_i}{k_{19}}\right)^p}\right)}\right) \tag{4.15}$$

$$\frac{dP_{ij}}{dt} = \frac{k_{15}P_iA_j}{\left(1+\frac{P_i}{k_{16}}\right)\left(1+\frac{A_j}{k_{17}}\right)\left(1+\frac{k_{18}\left(\frac{C_i}{k_{19}}\right)^p}{1+\left(\frac{C_i}{k_{19}}\right)^p}\right)} - k_{20}P_{ij} \tag{4.16}$$

$$\frac{dC_i}{dt} = k_8\kappa_i\frac{\left(\frac{A_i}{k_9}\right)^m}{1+\left(\frac{A_i}{k_9}\right)^m} - k_{10}C_i + \frac{k_{11}}{a_i}\hat{D}C_i \tag{4.17}$$

$$\frac{dCr_i}{dt} = \frac{k_{12}C_i}{1+\left(\frac{A_i}{k_{13}}\right)^n} - k_{14}Cr_i \tag{4.18}$$

A_i, P_i, C_i and Cr_i are concentrations of Auxin, PIN, CK and CK signaling in the cytoplasm of cell i. P_{ij} is the concentration of PIN at the cell wall of cell i adjacent to cell j. $\mathcal{N}_i$ denotes the set of cellular neighbors of cell i and l_{ij} is the length of the wall shared by cells i and j. The index functions χ_i and κ_i are defined by: The diffusion operator $\hat{D}$ operating on index i reads:

$$\hat{D}X_i = \sum_{j \in \mathcal{N}_i} l_{ij}(X_j - X_i) \tag{4.19}$$

The index functions χ_i and κ_i are defined by:

$$\chi_i = \begin{cases} R\text{: cell } i \text{ is an auxin source cell} \\ 1 \text{ : cell } i \text{ not an auxin source cell} \end{cases} \tag{4.20}$$

$$\kappa_i = \begin{cases} 1\text{: cell } i \text{ is within the vascular bundle excluding pericycle cells} \\ 0\text{: cell } i \text{ is within the vascular bundle excluding pericycle cells} \end{cases} \tag{4.21}$$

The equations are integrated in iterative steps using fifth-order, adaptive-step-size Runga-Kutta algorithm [9].

4.4.3 Growth algorithm

The simulation starts with a heart stage embryo template where the four vascular founder cells are surrounded by pericycle and endodermis layers (cortex and epidermis are not included in the model). These surrounding layers do not produce CK and have a fixed growth rate, which is not affected by CK levels. These layers thus do not contribute to the model itself. Besides this, the entire model (Fig. 4-8A) continuously runs in all cells. Cell growth is modeled using turgor pressure uniformly exerted on all walls of a cell that can counteract, irreversibly expand, or yield in response (Fig. 4-6). The area at which all cells except pericycle and endodermal cells divide is given by:

$$a_i(t) = \frac{2a_i^0}{1 + \frac{k_{21}\left(\frac{Cr_i(t)}{k_{22}}\right)^q}{1+\left(\frac{Cr_i(t)}{k_{22}}\right)^q}} \tag{4.22}$$

where a_i^0 is the initial area of cell i. The pericycle and endodermal cells divide once they reach 2 and 3.2 times their original area, respectively.

4.5 Model components and assumptions

The model consists of a set of nonlinear ordinary differential equations (see further) mapped to a growing cellular grid using the VirtualLeaf software [9]. In VirtualLeaf, cells are defined as polygons and cell walls consist of viscoelastic cell wall elements connected by nodes. A Monte-Carlo based energy minimization algorithm describes the resulting displacement of nodes. The mechanical energy state of the system is described by the Hamiltonian [9]:

$$\frac{H}{k_B T} = \lambda_A \sum_i (a_i(t) - \mathcal{A}_i(t))^2 + \lambda_M \sum_j (l_j(t) - \mathcal{L})^2 \tag{4.23}$$

- Indices i and j sum over all cells and walls respectively.
- λ_A defines a cell's resistance to area expansion and compression.
- λ_M defines resistance of the cell walls to elongation and compression.
- $\mathcal{A}_i(t)$ is the resting area at time t of cell i, which is defined as an area at which the intracellular turgor pressure is balanced by ambient pressure.
- $\mathcal{L}$ is the resting length of a wall element, and is defined as the length it would attain in absence of turgor pressure.
- $a_i(t)$ and $l_j(t)$ are the area of cell i and length of wall element j at time t.

Over the course of a simulation, the aforementioned algorithm results in fluctuations around the optimal energy configuration, which leads to non-unique energy minimizations paths. In other words, different instances of the same simulation do not produce identical outputs (Fig 4-5)further details of VirtualLeaf assumptions and algorithms we refer to the original publication of the software [9]. Model components are comprised of cytoplasm and cell wall.

All molecules in the model are only present in the cellular compartment itself; except for PIN proteins, which can be present in both cytoplasm and membrane (represented in the model by the cell wall). Since our model aims to investigate mechanisms of pattern formation and hormonal

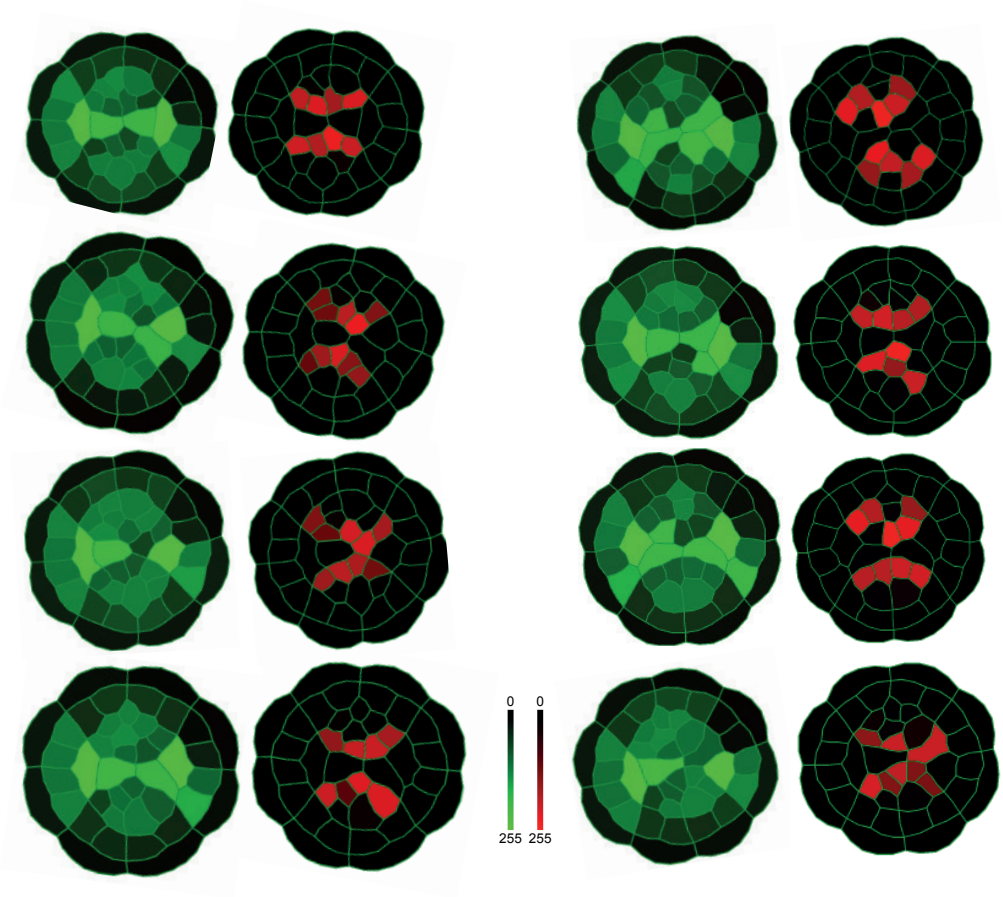

Figure 4-5: Fig. S8. Stochasticity in VirtualLeaf simulations. Due to the stochasticity of VirtualLeaf simulations, repeated simulations using the same setting and parameters do not produce identical outputs. Depicted are 8 independent simulations with identical parameters given in **table S4**, in which auxin signaling is shown in green (left panels) and CK signaling in red (right panels).

responses, we do not impose strict limits regarding the number of cells (18-60) in the model output. Simulations of mutants (Fig 4-10G,K and Fig 4-10H,L) and TMO5/LHW overexpression (Fig 4-13A,B), are run for the corresponding time-span of the wild-type simulation (Fig. 4-4F,J).

4.5.1 Simulation timescale

VirtualLeaf modeling platform assumes that mechanical equilibration of the growing tissue occurs much faster than the changes in protein and hormone concentrations. This separation of time scales is exploited in the simulation algorithm. One simulation step consists of three parts:

i The resting areas of the individual cells are incremented according to:

$$\mathcal{A}_i(t + \Delta t) = \mathcal{A}_i + \alpha \Delta t \tag{4.24}$$

where Δt is the time for one simulation step and α is the cell growth rate.

ii Mechanical equilibration is achieved; according to the above mentioned time scale separation this is considered to be instantaneous.

iii The reaction network is integrated from t to $t + \Delta t$, which completes the simulation step (Fig. 4-6). We assume that, by default, cells divide once they double their area. During this time, the average division rate of cells is approximately 130 hours. This gives us: $\alpha = \mu\text{m}^2\ h^{-1}$. In our simulations we use $\Delta t = 10$ min. Note that $\alpha \Delta t$ and Δt correspond to the parameters cell_expansion_rate and rd_dt in VirtualLeaf, respectively.

4.5.2 Simulation termination criteria

Simulations of the wild-type are terminated and the output is recorded when the source cells have divided at least once and there are at least 18 cells in the vascular bundle. This is justified by the observation that in wild-type, the protoxylem cells are at least two cells apart at the end of embryogenesis [139]. If the source cells remain undivided wild-type simulations are terminated once the cell number exceeds 60. This allows for a larger variation of the cell number in the model output compared to wild-type late heart stage embryo.

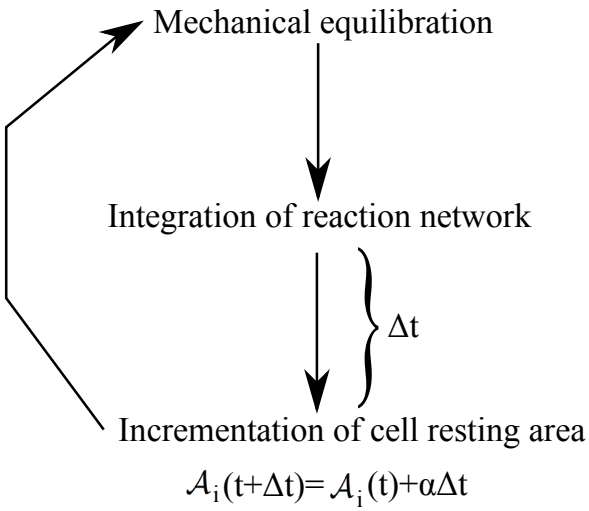

Figure 4-6: Overview of a VirtualLeaf simulation step. Mechanical equilibration of the growing tissue occurs much faster than the changes in protein and hormone concentrations. This is exploited in the simulation algorithm as in one simulation step first the mechanical configuration is equilibrated, then the reaction network is integrated and finally the target area of the cells are increased in order to mimic growth.

4.5.3 Model parameters

Model parameters were chosen from within biologically realistic ranges and manually curated to reproduce experimental observations. The following parameter values have been used in simulations of wild-type (Fig. 4-10F, J and Fig. 4-5).

4.5.4 Models parameters in mutant and over expression simulations

Mutation of MP gene was modeled by setting the parameter k_1 to zero. For the *wol* mutant, parameter k_8 was set to zero. TMO/LHW-OX was modeled by adding a constant production of CK ($0.5\,\mu\mathrm{mol}/(\mu\mathrm{m}^2\mathrm{min})$) in every cell.

As mentioned, we specified two "source cells" that contain elevated auxin concentration as a consequence of auxin transport from overlying tissues. During vascular tissue initiation, the cotyledon primordia become specified, which generates PIN1 convergence points [140] and hence local auxin sources in the cell layers overlying the vascular initials. As a consequence,

Table 4.1: Parameters used for the simulation in the main text.

Parameter	Value	Description	Unit
k_1	0.038	auxin production	$\frac{\mu\text{mol}}{\mu\text{m}^2\ \text{min}}$
k_2	0.053	auxin degradation	$\frac{1}{\text{min}}$
k_3	0.16	auxin membrane permeability	$\frac{\mu\text{m}}{min}$
k_4	0.45	auxin active transport	$\frac{\mu\text{m}^2}{\mu\text{mol min}}$
k_5	1.0	half max. auxin concentration for active transport	$\frac{\mu\text{mol}}{\mu\text{m}^2}$
k_6	0.01	cytosolic PIN production	$\frac{\mu\text{mol}}{\text{min}}$
k_7	0.10	PIN degradation	$\frac{1}{\text{min}}$
k_8	6.0	auxin dependent CK production	$\frac{\mu\text{mol}}{\mu\text{m}^2\ \text{min}}$
k_9	2.51	half max. auxin concentration for CK production	$\frac{\mu\text{mol}}{\mu\text{m}^2}$
k_{10}	0.498	CK degradation	$\frac{1}{\text{min}}$
k_{11}	0.10	CK membrane permeability	$\frac{\mu\text{m}}{min}$
k_{12}	2.11	CK response activation	$\frac{1}{\text{min}}$
k_{13}	2.5	half max. auxin concentration for response inhibition	$\frac{\mu\text{mol}}{\mu\text{m}^2}$
k_{14}	0.12	CK response degradation	$\frac{1}{\text{min}}$
k_{15}	5.0	PIN wall insertion rate	$\frac{\mu\text{m}^3}{\text{min}}$
k_{16}	1.0	half max. PIN concentration for wall insertion	$\frac{\mu\text{mol}}{\mu\text{m}^2}$
k_{17}	2.0	half max. auxin concentration for PIN wall insertion	$\frac{\mu\text{mol}}{\mu\text{m}^2}$
k_{18}	271.18	CK inhibition strength of PIN wall insertion	1
k_{19}	9.42	half max. CK concentration for inhibition of PIN wall insertion	$\frac{\mu\text{mol}}{\mu\text{m}^2}$
k_{20}	0.30	PIN dissociation rate from the wall	$\frac{\mu\text{m}}{\text{min}}$
k_{21}	1.17	strength of CK suppression of the division threshold	1
k_{22}	0.046	half max. Cr concentration for threshold suppression	$\frac{\mu\text{mol}}{\mu\text{m}^2}$
R	10	ratio of auxin production in source to non-source cells	1
m	5	Hill coefficient	1
n	5	Hill coefficient	1
p	4	Hill coefficient	1
q	5	Hill coefficient	1
λ_A	1	resistance of the cells to area expansion and compression	$\frac{1}{\mu\text{m}^4}$
λ_M	100	resistance of the cell walls to elongation and compression	$\frac{1}{\mu\text{m}^2}$
$\mathcal{L}$	3	resting length of the cell walls	μm
α	1/60	cell growth rate	$\frac{\mu\text{m}^2}{\text{min}}$

auxin is nonuniformly provided to the underlying vascular initials that are in closest proximity to the cotyledon primordia (Fig. 4-8B-E). Indeed, 3D reconstructions showed that auxin-dependent p*TMO5* (Fig. 4-8, F to I), p*DR5*, and p*LOG4* expression (Fig. 4-9A-B) was stronger in the two vascular initials that subtend the cotyledon primordia, and cotyledon number has previously been correlated with vascular tissue patterns [141].

4.6 Model analysis

4.6.1 Early geometric constraints bias vascular patterning

We simulated this network (Fig. 4-8A) and monitored growth and patterning, where auxin accumulation is a proxy for xylem identity and CK response reflects the cambial domain. Because exact values are unknown for most parameters, we performed a survey to find parameter sets for which the model generates a bisymmetric vascular bundle with a central high-auxin domain (See model analysis and Fig. 4-14). All following model analysis is based on the identified well-performing parameters sets.

Cellular connection bridge

We initially started from a stylized cross section of the embryonic root at early heart stage [122] (Fig. 4-10A). However, this simple geometry did not lead to a continuous central xylem axis flanked by cambial domains (Fig. 4-10A). Further exploration of the starting template indicated that the initial geometry strongly biases final model output. Only a configuration in which two of the four founder cells are connected by a small "bridge" (Fig. 4-10B) yielded stable realistic patterns (Fig. 4-10, E and F, I and J). We found that the existence of a bridge is required. Existence of a central cell wall between the two source cells coupled with growth and division of cells in flanking regions, results in elongated geometry of these cells prior to division. This ultimately leads to formation of the orientated division axis that in turn yields the correct geometry required for formation of a xylem axis (Fig 4-10B). In case of a four-way junction, due to the resulting overall symmetry, source cells attain a more symmetrical shape. This however does not guarantee the formation of the appropriate division axis required for the correct patterning (Fig. 4-10A). The scenario where the initial central wall was is shared by non-source cells did not lead to correct patterning (Fig. 4-10C).

Alteration of the bridge

We investigated whether the orientation of the connecting bridge has any effects on the growth and patterning of the tissue. Experimentations with the angle of the bridge between the two source cells reveal that any deviation from a vertical angle (perpendicular to the line passing through the centers of source cells) would result in reversion to the vertical angle (Fig. 4-7A). The Hamiltonian energy function as described earlier, maximizes the cell area while equalizing the edge length. This results in regular polygons. Hence, the irregular geometry of source cells resulting from deviation of the bridge from the vertical position is subsequently changed by reversion of the bridge to a vertical position. Similarly, altering the length of the bridge in the initial template does not affect the patterning capability of the model nor the length of the bridge in model output (Fig. 4-7B-C).

Furthermore, blocking active and passive transport across the bridge, does not affect the patterning ability of the model (Fig. 4-7D), indicating that the contribution of the bridge towards patterning is primarily geometrical.

We next evaluated the presence of a cellular connection between source cells, and found this geometry in nearly all embryos analyzed in 3D up to globular stage (21 out of 26; Fig. 4-10D and Fig. 4-9C) and in all embryos at postglobular stages (11 out of 11; Fig. 4-10D and Fig. 4-9C). Tracing the origin of the bridge revealed that it is a consequence of division planes at the two- to four-cell transition (Fig. 4-9C). Thus, this particular geometry in the center of the embryo follows from the improbability of generating exact four-way junctions [142] during earlier cell divisions, followed by cell expansion [123].

Intriguingly, the bridge needs to connect the source cells subtending the future cotyledon primordia (Fig. 4-10, B and C), and hence receive increased auxin input (Fig. 4-8, F to I, and Fig. S6, A and B). We therefore analyzed whether the bridge serves a function in intercellular signaling. In our simulation, we blocked transport of auxin and CK across this bridge and found that the model output remained unchanged (Fig. 4-7). We therefore conclude that the bridge

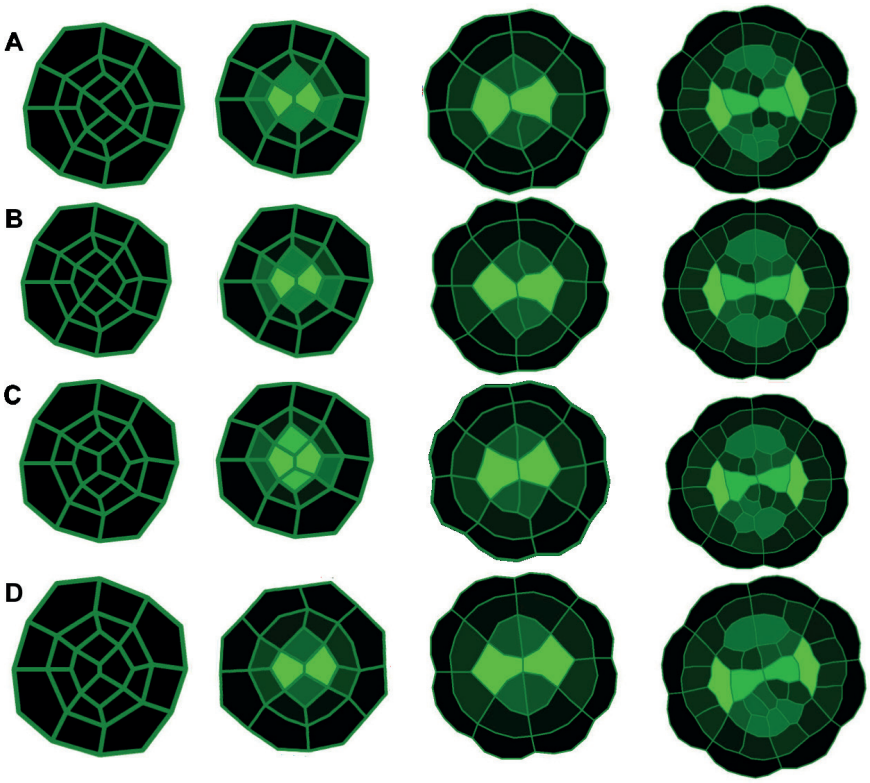

Figure 4-7: Model simulations using various bridge configurations. Tilting (A), decreasing (B), increasing (C) the bridge in the initial template, does not affect the patterning ability of the model. (D) Blocking active and passive transport across the bridge does not alter the pattern potential of the model.

imposes a geometric constraint to cell division.

We next tested robustness of our model toward parameter variation by performing sensitivity analysis (Supplementary Mathematical Modeling; Fig. 4-14). This showed that model performance depended most strongly on parameters connected to CK biosynthesis, CK response, and effect on PIN1 localization and cell division.

Finally, to validate this model, we determined whether it could recapitulate the developmental consequences of reduced auxin response [monopteros (mp) mutant; parameter k_1 set to 0] [143] or reduced CK response (*wol* mutant, parameter k_8 set to 0) [131]. In both cases, the model

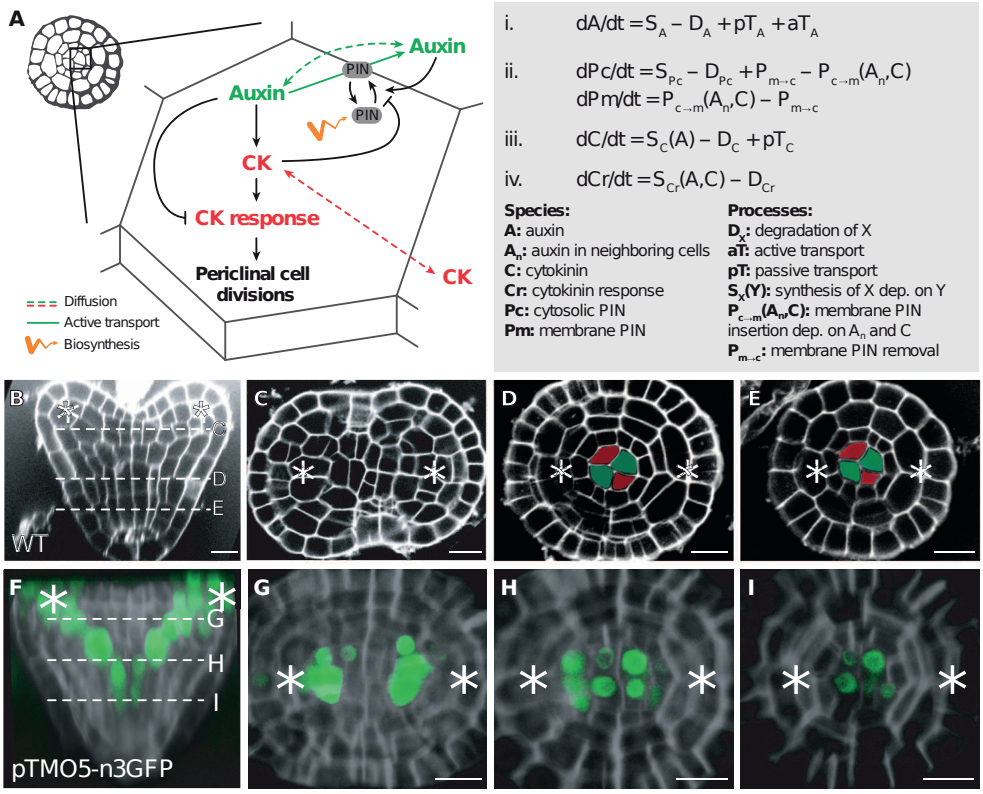

Figure 4-8: Connectivity of vascular initial cells. (A) Schematic representation of the identified genetic network (left) in an early heart stage embryo, and simplified ordinary differential equations reflecting these interactions in the model (right). (B to E) 3D reconstructed heart stage embryo showing the association of the connected vascular initial cells to the forming cotyledons. (F to I) pTMO5-n3GFP expression at different locations in the heart stage embryo relative to the location of the cotyledons. Scale bars, 10 μm.

correctly predicted the cellular pattern and hormonal responses (Fig. 4-10, G and K, H and L).

4.6.2 Network architecture during vascular tissue patterning

To understand how the genetic network is able to generate growth and patterning, we analyzed its modules in more detail. The conceptualized version of this network contains two interconnected incoherent feed-forward loop (IFFL) motifs (Fig. 4-11) [27]. IFFL-1 entails the opposing effects of auxin and auxin-dependent CK on PIN levels, whereas IFFL-2 describes the effects of auxin on CK biosynthesis and response. Although the temporal dynamics of IFFLs have been

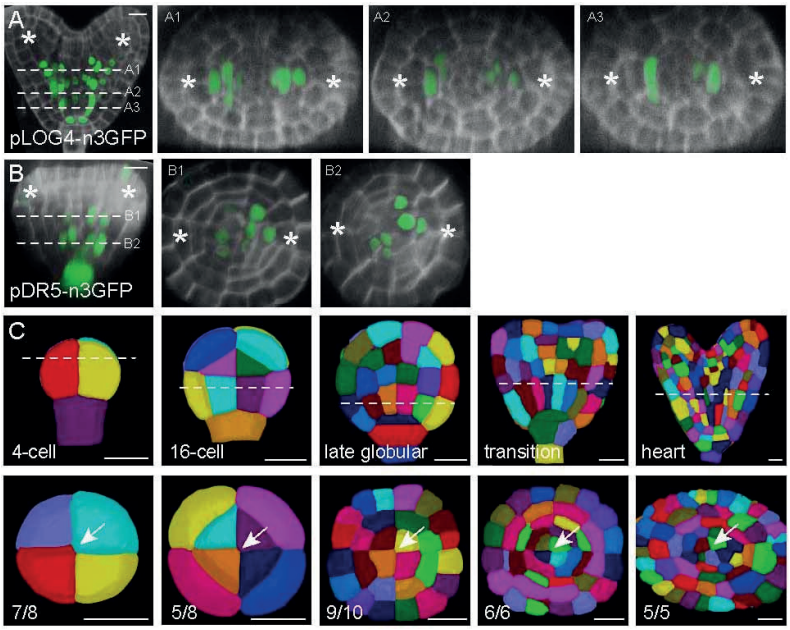

Figure 4-9: Two connected vascular founder cells have increased auxin-dependent expression. (A-D) Expression of the pLOG4-n3GFP (A) and pDR5-n3GFP (B) reporter lines at different locations in the he art stage embryo (as indicated by the dashed line)relative to the location of the cotyledons (asterisks). (C) 3D segmentation of confocal stacks of successive stages of embryogenesis showing the connection ('bridge') between two of the four provascular initial cells (arrows). The dotted line in the upper panel represents the location of the cross section shown in the lower panel. Note that the bridge is more pronounced at the apical part of the cell in the 4-cell stage, compared to the basal part and that the presence of the bridge becomes clearer later in development. For example, the bridge was clear in all transition (6/6) and heart stage (5/5) confocal stacks analyzed, while seen at lower percentage in earlier stages (e.g. 5 out of 8 at 16-cell stage). Scale bars are 10 μm.

previously discussed [27], their spatial properties may be more relevant for correct patterning in our model, given the intercellular signaling within a growing multicellular structure. In the following section we analyze the individual contributions of these two IFFLs to spatiotemporal tissue patterning by separating the two subnetworks. We demonstrate that IFFL-1 can generate a high-auxin domain between the two source cells in the growing tissue (Fig. 4-11), but fails to from a sharp bisymmetric pattern. IFFL-2, on the other hand, can generate sharp boundaries between the high-auxin domain and the neighboring CK response domains (Fig. 4-11). Integration of both motifs thus generates stable and distinct hormonal response zones within the growing vascular tissue. As such, the high-auxin domain in the xylem axis acts as an

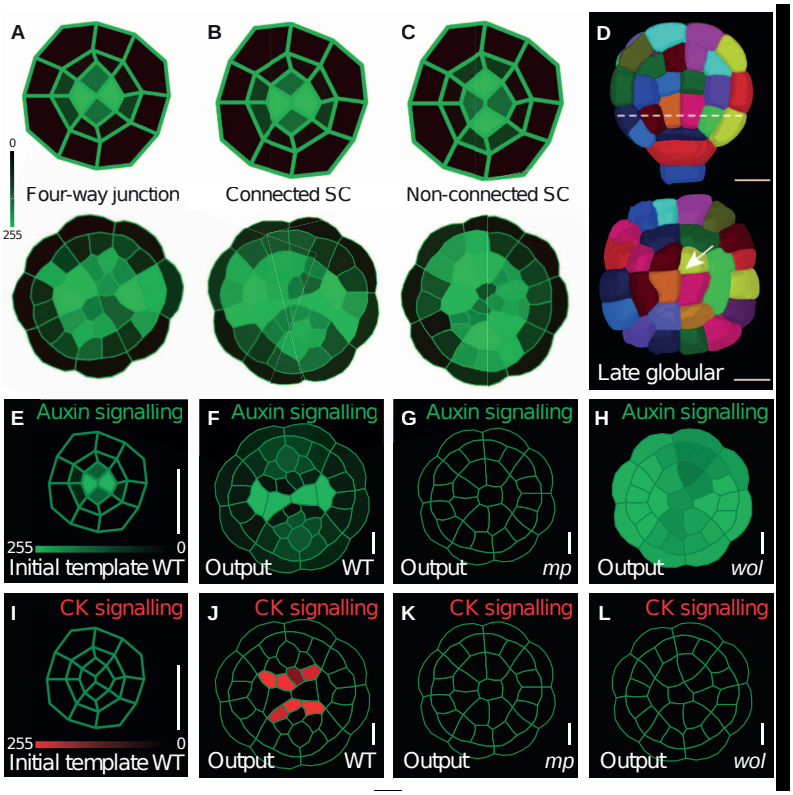

Figure 4-10: A growing model of vascular tissue formation. (A to C) Different initial geometries tested in the model. Left: four-way junction; middle: connection between source cells (SC); right: connection between non-source cells. Auxin signaling is shown in green, and PIN protein quantity at the membrane in red. (D) 3D reconstructed globular stage embryo showing connection between two vascular founder cells. (E to L) Model simulations using a realistic heart stage embryo template before (E and I) and after (F to H and J to L) growth showing auxin signaling (green) (E to H) and CK signaling (red) (I to L) in a WT situation (E and F, I and J), with reduced auxin signaling (representing mp: G and K) and with reduced CK response (representing wol: H and L). Scale bars, 10 μm (D); those in (E) to (L) are relative to each other.

organizer for the entire vascular bundle.

4.6.3 Analysis of the IFFL motifs

IFFL-1

In order to explore the mathematical model we analyzed the patterning properties of the two coupled IFFLs separately. First, we examined the properties of IFFL-1 (Fig. 4-11).

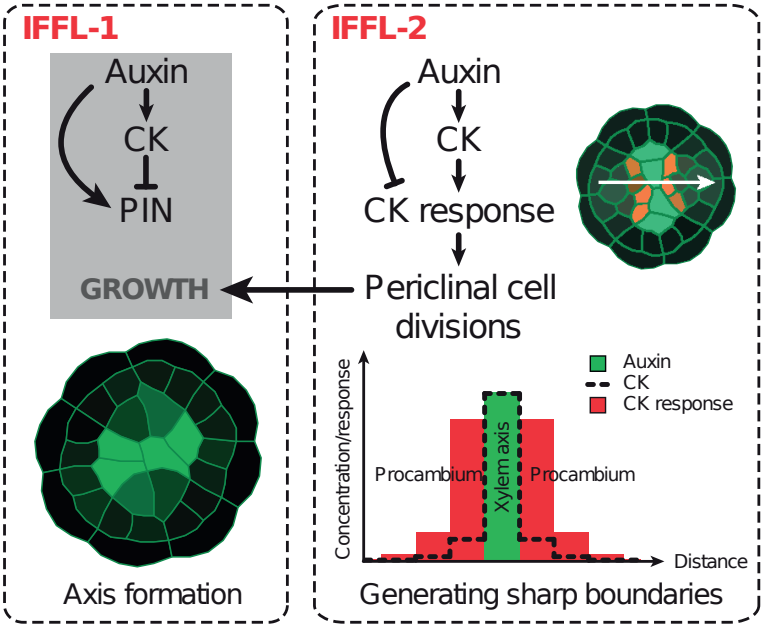

Figure 4-11: The genetic network comprises two incoherent feed-forward loops. Overview of the two connected IFFLs in the genetic network. IFFL-1 generates a high-auxin domain, whereas IFFL-2 creates sharp boundaries, as indicated by a discretized 1D model (along the white arrow) representing CK concentration (dashed line) and CK response (in cambium, red bars) according to the distance from the auxin domain (xylem axis, green bar).

Because growth and non-linear active transport are an integral ingredients of this motif, analytical examination is challenging. We therefore performed numerical experiments in order to investigate the behavior of the motif across the parameter space. The mathematical

equations describing IFFL-1 read:

$$\frac{dA_i}{dt} = k_1\chi_i - k_2A_i + \frac{k_3}{a_i}\hat{D}A_i + \frac{k_4}{a_i}\sum_{j\in\mathcal{N}_i} l_{ij}\left(\frac{P_{ij}A_j}{1+\frac{A_j}{k_5}} - \frac{P_{ji}A_i}{1+\frac{A_i}{k_5}}\right) \tag{4.25}$$

$$\frac{dP_i}{dt} = k_6 - k_7P_i + \sum_{j\in\mathcal{N}_i}\frac{l_{ij}}{a_i}\left(k_{20}P_{ij} - \frac{k_{15}P_iA_j}{\left(1+\frac{P_i}{k_{16}}\right)\left(1+\frac{A_j}{k_{17}}\right)\left(1+\frac{k_{18}\left(\frac{C_i}{k_{19}}\right)^p}{1+\left(\frac{C_i}{k_{19}}\right)^p}\right)}\right) \tag{4.26}$$

$$\frac{dP_{ij}}{dt} = \frac{k_{15}P_iA_j}{\left(1+\frac{P_i}{k_{16}}\right)\left(1+\frac{A_j}{k_{17}}\right)\left(1+\frac{k_{18}\left(\frac{C_i}{k_{19}}\right)^p}{1+\left(\frac{C_i}{k_{19}}\right)^p}\right)} - k_{20}P_{ij} \tag{4.27}$$

$$\frac{dC_i}{dt} = k_8\kappa_i\frac{\left(\frac{A_i}{k_9}\right)^m}{1+\left(\frac{A_i}{k_9}\right)^m} - k_{10}C_i + \frac{k_{11}}{a_i}\hat{D}C_i \tag{4.28}$$

We simulated these equations on growing discrete domain using the same model settings as for the main model. It is important to note that in the absence of Cr cells divide when they doubled there size (see Eq. (4.22)). The prevailing property of this motif is to form connected domains of high auxin concentration, given at least one source cell (cell with high basal auxin content) exists. A typical pattern result of this motif is shown in Fig. 4-11 using the parameters listed in **table 4.1**, besides: ($k_1 = 2.8$, $k_2 = 0.25$, $k_8 = 2$, $k_10 = 0.5$, $k_12 = 0.25$, $k_14 = 0.25$, $k_18 = 40$, $k_19 = 2.8$, $k_21 = 1$, $k_22 = 0.15$). Cells with high auxin content will have also high CK content, Eq. (4.28). It follows that inhibition of PIN insertion by CK, Eq. (4.27), attenuates the positive feedback of auxin on the active transport from neighboring cells and finally blocks active transport in cells with high auxin, Eq. (4.25). Due to this mechanism neighboring cells with high auxin levels can coexist. In contrast, without CK inhibition this configuration is unstable because small differences in auxin content between adjacent cells will be amplified.

IFFL-2

Next we investigated the capability of the IFFL-2 motif in producing distinct domains of hormonal responses. To this end it is sufficient to implement the motif in a one-dimensional setting

assuming a fixed level of auxin in the center of the domain. The spatial index n corresponds to the direction perpendicular to the xylem axis. The equations are as follows:

$$\frac{dC_i}{dt} = k_8 A_i - k_{10} C_i + \frac{k_{11} l}{a}\left(C_{i+1} + C_{i-1} - 2C_i\right) \tag{4.29}$$

$$\frac{dCr_i}{dt} = \frac{k_{12} C_i}{1 + \left(\frac{A_i}{k_{13}}\right)^n} - k_{10} Cr_i \tag{4.30}$$

We assumed that all cells have the same area and are connected with wall elements of the same length, i.e., $a_i \equiv a$ and $l_{ij} \equiv l$. The auxin input profile reads:

$$A_i = \begin{cases} A_0\text{: } i = 0 \\ A_1\text{: } |i| > 0 \end{cases} \tag{4.31}$$

The steady state solution to this discrete set of equation, using the boundary conditions $\lim_{i\to\infty} C_i = 0$ and $C_i = C_{-i}$ read:

$$C_i = \begin{cases} \frac{\beta(A_0(1+2\gamma-\gamma e^{-q})+2A_1(\gamma+\gamma^2(1-e^{-q})))}{1+4\gamma-\gamma e^{-q}+2\gamma^2(1-e^{-q})} & : i = 0 \\ \beta A_1 + \frac{\beta\gamma(A_0-A_1)}{1+4\gamma-\gamma e^{-q}+2\gamma^2(1-e^{-q})} e^{-q(|i|-1)} & : |i| > 0 \end{cases}$$

$$Cr_i = \begin{cases} \frac{\beta\theta A_0}{1+\left(\frac{A_0}{k_{13}}\right)^n} \frac{(1+2\gamma-\gamma e^{-q})+2\frac{A_1}{A_0}(\gamma+\gamma^2(1-e^{-q}))}{1+4\gamma-\gamma e^{-q}+2\gamma^2(1-e^{-q})} & : i = 0 \\ \frac{\beta\theta A_0}{1+\left(\frac{A_1}{k_{13}}\right)^n} \left[\frac{A_1}{A_0} + \frac{\gamma(1-\frac{A_1}{A_0})}{1+4\gamma-\gamma e^{-q}+2\gamma^2(1-e^{-q})} e^{-q(|i|-1)}\right] & : |i| > 0 \end{cases}$$

We defined the following parameters: $\beta = \frac{k_8}{k_{10}}, \theta = \frac{k_{12}}{k_{14}}, \gamma = \frac{k_{11} l}{k_{10} a}, q = 2\,\mathrm{argsinh}\left[\sqrt{\frac{1}{4\gamma}}\right]$.

$$\frac{\partial C}{\partial t}(y) = k_8 A(y) - k_{10} C(y) + D\frac{\partial^2 C}{\partial y^2}(y) \tag{4.32}$$

$$\frac{\partial Cr(y)}{\partial t} = \frac{k_{12} C(y)}{1 + \left(\frac{A(y)}{k_{13}}\right)^n} - k_{14} Cr(y) \tag{4.33}$$

The auxin input profile reads:

$$A(y) = \begin{cases} 1\text{: } y \le y_0 \\ 0\text{: } y > y_0 \end{cases} \tag{4.34}$$

The steady-state solution using the boundary conditions $\partial_y C(y=0) = 0$ and $\lim_{y\to\infty} C(y) = 0$ are given by:

$$C(y) = \begin{cases} \frac{k_{18}}{k_{10}}\left(1 - e^{-\frac{y_0}{l}} \cosh\left(\frac{y}{l}\right)\right) & : y \le y_0 \\ \frac{k_{18}}{k_{10}}\left(1 - e^{-\frac{y}{l}} \sinh\left(\frac{y_0}{l}\right)\right) & : y > y_0 \end{cases} \tag{4.35}$$

$$Cr(y) = \begin{cases} \frac{k_{12}k_{18}}{k_{10}k_{14}} \frac{k_{13}^n\left(1-e^{-\frac{y_0}{l}}\cosh\left(\frac{y}{l}\right)\right)}{1+k_{13}^n} & : y \le y_0 \\ \frac{k_{12}k_{18}}{k_{10}k_{14}}\left(1 - e^{-\frac{y}{l}} \sinh\left(\frac{y_0}{l}\right)\right) & : y > y_0 \end{cases} \tag{4.36}$$

The IFFL-2 motif produces a Cr concentration zone distinct from the auxin input (Fig. 4-11), where it acts as an inverter of the input profile. The drop from cell $i = 0$ (auxin input zone) to cell $i = 1$ is given by:

$$\frac{C_1}{C_0} = \frac{\beta A_1(1 + 4\gamma - \gamma e^{-q} + 2\gamma^2(1 - e^{-q})) + \beta\gamma(A_0 - A_1)}{\beta(A_0(1 + 2\gamma - \gamma e^{-q}) + 2A_1(\gamma + \gamma^2(1 - e^{-q})))}$$

for which we find the limiting cases: $\lim_{\gamma\to 0} \frac{C_1}{C_0} = \frac{A_1}{A_0}$ and $\lim_{\gamma\to\infty} \frac{C_1}{C_0} = 1$. Experimental observation show that the CK response does not extend very far from the central zone. The range is the CK profile is given by q^{-1}. It follows $q \gg 1$ (by this the CK profile does only significantly extend to the cell layer next to the xylem axis). This means that $2\,\mathrm{argsinh}\left[1/\sqrt{4\gamma}\right] \gg 1$ or roughly $\gamma \ll 1$ due to the properties of $\mathrm{argsinh}$. If we assume rectangular cells with an area $a = 400\mu\mathrm{m}^2$ and $l = 20\mu\mathrm{m}$, we find: $20\mu\mathrm{m} \gg \frac{k_{11}}{k_{10}}$, which puts a constraint on the ratio of the CK membrane permeability k_{11} and the CK degradation k_{10}. We find this fulfilled for all parameter sets $\vec{p} \in \omega_1$. E.g., for the parameters shown in **table 4.1** we obtain: $\frac{k_{11}}{k_{10}} \approx 0.5\mu\mathrm{m}$, which leads to $q \approx 4.6$.

In IFFL-2 auxin promotes CK but inhibits CK response. The strength $\mathcal{I}_i$ of the inhibition at point i can be defined as:

$$\mathcal{I}_i = 1 - \frac{Cr_i}{\lim\limits_{k_{13}\to\infty} Cr_i} = \frac{\left(\frac{A_i}{k_{13}}\right)^n}{1 + \left(\frac{A_i}{k_{13}}\right)^n}$$

CK response should be inhibited inside the xylem axis, but not outside. For a steep response of the inhibition to changes in auxin concentration the hill coefficient should be $n \geq 3$. Further, for the background production of auxin, $A_i = A_1$ for $|i| > 1$, should be low. It follows that $\frac{A_1}{k_{13}} < 1$ should hold. If we assume $A_0 \approx \frac{Rk_1}{k_2}$ and $A_1 \approx \frac{k_1}{k_2}$ we find that $1 > \frac{k_1}{k_2 k_{13}}$ should hold, which constrains the half max. auxin concentration for response inhibition k_{13}. For the parameter set given in **table S4** we have $\frac{k_1}{k_2} = 0.72$ and $k_{13} = 2.5$, i.e., $\frac{A_0}{k_{13}} \approx 2.9$ and $\frac{A_1}{k_{13}} \approx 0.29$.

4.6.4 Reproduction of mutant and overexperssion phenotypes

In our model, the same genetic network runs in all cells, but spatial bias imposed by local auxin sources is propagated to limit CK activation to TMO5/LHW-expressing xylem cells. To determine if local CK activation is required for normal growth and patterning, we first simulated the effects of uniform *TMO5/LHW* or *LOG4* expression by increasing the CK activation rate in all cells. This increased periclinal cell division and generated a large disorganized vascular bundle lacking a central xylem axis (Fig. 4-13, A and B), resembling the TMO5/LHW-OX phenotype [125]. We next tested the model prediction that local CK activation is important for vascular development by complementing the *log*1234578 mutant with either local (p*TMO5*) or ubiquitous (p*RPS5A*) *LOG4* expression. p*TMO5*-driven *LOG4* expression completely complemented the *log*1234578 mutant phenotype, whereas in contrast, pRPS5A-driven LOG4 expression induced supernumerary vascular cell files and loss of protoxylem differentiation (Fig. 4-13, C to F, and Fig. B6). Hence, local *LOG4* expression is sufficient for normal vascular development, and limitation to this domain is required to constrain cell number and patterning.

If CK is indeed locally activated in the xylem axis and diffuses outward, a gradient of CK response should be observed in procambium cells with maximal intensity close to the xylem (Fig. 4-10J). We tested this prediction by analyzing reporters for CK response. Indeed, both p*TCS*n-GFP and p*ARR5*-nYFP markers displayed this gradient (Fig. 4-13, H to K) [124], suggesting that our model accurately predicts CK activity in the growing vascular tissue.

4.7 Parameter exploration

4.7.1 Model evaluation

In order to evaluate the resulting simulation patterns one needs to define appropriate quantitative measures. The correct patterning of the model can be assessed using the auxin concentration distribution. A one-to-one comparison of auxin distributions would impose overly strict

restrictions on the model behavior, because the focus of the model is the general pattering behavior as opposed to exact reproduction of a specific pattern. Rather then comparing two-dimensional patterns we extract essential features from the auxin concentration distribution, which characterize the correct model output. Model analysis requires definition of a consistent geometrical coordinate system. The two-dimensional geometrical outline of a cross section of a wild-type vascular bundle during embryogenesis can be defined in reference to orientation of the xylem axis. In order to define an appropriate Cartesian coordinate system, we follow the below protocol:

1. Determine the direction of the x-axis by the direction of the line passing through the centroids of the source-cells (Fig. 4-12A).

2. Look for the integration path with highest auxin concentration parallel to the direction defined in 1 (Fig.4-12B).

3. The integration path with the highest auxin concentration defines the x-axis and the mid-point of the line defined in step 1. projected to the x-axis defines the origin of the coordinate system (Fig. 4-12C).

Using this coordinate system cellular auxin concentrations are mapped to a two-dimensional auxin concentration field: $A_i(\vec{p}) \rightarrow A(x, y; \vec{p})$, where $\vec{p}$ is the parameter vector. The first feature we extract from this two-dimensional concentration field is the marginalized and normalized auxin profile in y-direction, given by:

$$\bar{A}(y; \vec{p}) = \frac{\int_\Omega A(x, y; \vec{p}) dx}{\left\| \int_\Omega A(x, y; \vec{p}) dx \right\|} \tag{4.37}$$

Due to higher auxin input of the source-cells in the model, higher auxin concentrations can form along x-axis regardless of correct patterning. To address this bias the integration domain Ω is limited to a rectangle that excludes the source cells (Fig. 4-12C). The marginalized auxin field captures an essential feature of a correct pattern and can be easily compared to experimental data.

The second feature is the coefficient of variation η of the auxin concentration along the x-axis between the two source-cells:

$$\eta(\vec{p}) \quad = \quad \frac{\sqrt{\frac{1}{L}\int_\Omega \left(A(x,0;\vec{p})-\mu\right)^2 dx}}{\mu} \tag{4.38}$$

with L being the extension of the integration domain Ω (Fig. 4-12C) in x-direction at $y = 0$ and μ is the average auxin concentration along this line, given by:

$$\mu \quad = \quad \frac{1}{L}\int_\Omega A(x,0;\vec{p})dx \tag{4.39}$$

This feature distinguishes a non-continuous xylem axis from a correct pattern (Fig. 4-14D,E). For numerical integration, the extended trapezoidal rule is applied [144].

Reference auxin profile

A reference marginalized auxin concentration$\bar{A}_{exp}(y)$ can be obtained from experimental data by using GFP intensity as a proxy for auxin concentration in a cross-section of a 3D confocal stack of a postembryonic p*DR5*-n3GFP root (Fig. 4-12). A reference marginalized auxin concentration profile $\bar{A}_{exp}(y)$ can be obtained from experimental data by using GFP intensity as a proxy for auxin concentration in a cross-section of a 3D confocal stack of a post-embryonic pDR5-n3GFP root (Fig. 4-14). In the model, auxin concentration is a proxy for auxin downstream signaling. Experimentally, auxin response reporter genes are used as proxies for auxin signaling. Hence for model evaluations, we compare the pattern of auxin concentration against the p*DR5*-n3GFP expression pattern. We estimated the width $\sigma_i$of the marginalized auxin profile and the background level c_i for each experimental curve individually by solving:

$$\min_{\sigma_i,c_i} \|g(\sigma_i,c_i) - \bar{A}^i_{exp}\|^2 \tag{4.40}$$

Here $\|\cdot\|$ denotes the L2 norm, $\bar{A}^i_{exp}$ the ith experimentally measured profile, and g is given by: $g(x;\sigma,c) = c+(2\pi\sigma^2)^{-1/2}e^{-x^2/(2\sigma^2)}$. Using four experimental curves we found $\langle\sigma\rangle = 0.0745$

and $\langle c \rangle = 1.23$. This resulted in the reference profile:

$$\bar{A}_{\mathrm{ref}}(x) = \frac{g(x; \langle \sigma \rangle, \langle c \rangle)}{\|g\|} \tag{4.41}$$

which we used in the cost function as described below.

Construction of the cost function

The simulated pattern was evaluated against two objectives:

1. the distance d of the marginalized auxin profile $\bar{A}$, (Eq. 4.37), from the reference profile $\bar{A}_{\mathrm{ref}}$, Eq. (4.41):

$$d(\vec{p}) = \|\bar{A}(\vec{p}) - \bar{A}_{\mathrm{ref}}\| \tag{4.42}$$

2. and the variation η along the x-axis at $y = 0$, given by Eq. (4.38).

We aggregate the two objectives into the cost function L used for the parameter sampling process:

$$L(\vec{p}) = \left(\frac{\sqrt{2} d(\vec{p})}{d_0} \right)^2 + \left(\frac{\eta(\vec{p})}{\eta_0} \right)^2 \tag{4.43}$$

where d_0 denotes the distance of a flat, i.e., constant profile $\bar{A}(y) = \mathrm{const}$ to the reference profile. The cost function is constructed such that for ($d^2 = d_0^2/2$, $\eta = 0$), i.e. flat profile, as well as for ($d = 0$, $\eta = \eta_0$), i.e. perfect auxin profile with moderated variation in x-direction, $L = 1$ holds. We used $(d_0, \eta_0) = (0.65, 0.4)$ in the sampling process. Due to the inherent stochasticity of the Monte-Carlo simulations, the score $L(\vec{p})$ for parameter vector $\vec{p}$ is a stochastic value. We therefore average the score $\langle L(\vec{p}) \rangle$ over 200 simulations with identical initial conditions and parameters. The estimated standard error of the sample mean calculated by bootstrapping [144] was 0.0058 for 200 runs of the parameters described above.

Parameter sampling

In order to explore the global behavior of the model, we performed a qualitative parameter scan. We centered around an initial parameter set $\vec{p}_1$ with $\langle L(\vec{p}_1)\rangle < 1$ a hypercube Ω on the logarithmic scale, where we extended each parameter one order of magnitude in each direction: $\Omega = \Pi_j[p_1^j/10, 10p_1^j]$. Out of this subspace we randomly selected $N = 10^6$ parameter sets using Latin Hypercube Sampling [145]. For each of these sets or vectors $\vec{p} \in \{\vec{p}_1, \ldots, \vec{p}_N\}$, we calculated the averaged score $\langle L(\vec{p})\rangle$as described above. The subset defined by $\omega_1 = \{\vec{p} \in \{\vec{p}_1, \ldots, \vec{p}_N\} | \langle L(\vec{p})\rangle < 1\}$ gives those parameter sets for which the model produces a good pattern. Out of $N = 10^6$ tested we found $M = 25$ good parameter sets, i.e., $\#\omega_1 = 25$.

Sensitivity Analysis

Sensitivity was calculated as described in chapter 3:

$$S_i^j = \frac{p_i^j}{\langle L(\vec{p}_i)\rangle} \left| \frac{\langle L(p_i^1, \ldots, p_i^{j-1}, p_i^j + \delta, p_i^{j+1}, \ldots)\rangle - \langle L(\vec{p}_i)\rangle}{\delta} \right| \tag{4.44}$$

where $\langle\cdot\rangle$ denotes averaging over 200 simulations. From the set of S_i^j we calculated the quartiles as shown in the box-plot Fig. 4-14A.

4.7.2 Discussion

For decades, classical tissue culture experiments have been used to study the interaction between auxin and CK during tissue growth [146]. These phytohormones were suggested to act in a mutual inhibitory fashion in vascular tissue patterning [125, 130]. Here, we identified an interaction in which auxin promotes local CK activity in a manner central to both growth and patterning.

In parallel to promoting CK biosynthesis through TMO5/LHW as shown here, auxin was previously revealed to suppress CK response in the xylem [101]. Hence, auxin triggers the

formation of a nonresponding CK source. Modeling showed that this network, representing an IFFL, could account for generating a sharp boundary between high-auxin and high-CK domains. Furthermore, provided that auxin-dependent CK response suppression is cell-autonomous, CK diffusion will displace the domain of response to neighboring cells. An important question is what the nature of CK response inhibition is. Auxin activates expression of the CK response inhibitor AHP6 [124], but mutant phenotypes suggest that parallel or redundant functions must exist [101]. A recent study proposed local activity of a CK oxidase in xylem cells as a potential redundant mechanism [9]. However, it is questionable if local catabolism is compatible with the xylem acting as a CK source. The presence of a CK response gradient with the highest levels close to the xylem axis [9, 125] also renders regulation at the level of catabolism unlikely. Thus, inhibition likely acts at the level of CK response, and it will be important to identify its mediators.

Our simulations also revealed a surprising contribution of initial geometry to vascular tissue patterning. The bridge that connects the two auxin-accumulating vascular founder cells can be traced to the second round of divisions of the apical cell in the embryo. In addition, we have previously shown that the orientation of the first division is biased relative to the axes of the seed [123]. Thus, symmetry breaking in the vascular tissue could occur much earlier than previously thought. Likewise, lineages that generate the two cotyledons, the likely sources of auxin for vascular initiation [124, 147], can also be traced to these very early divisions [148]. Hence, both the geometric constraints and the signaling input that promote vascular tissue patterning are biased by the same cues. Whereas these findings show a clear correlation between geometry and pattern, it will be challenging to test causality because cell arrangements cannot easily be manipulated. Another critical question emerging from this is whether vascular tissue development in other plant species and during postembryonic organogenesis is similarly influenced by tissue geometry.

In conclusion, here we have identified a genetic network that reinfoerces an early developmental bias in auxin distribution to create a local, nonresponding source of CK, which drives growth

and patterning of the embryonic vascular tissues.

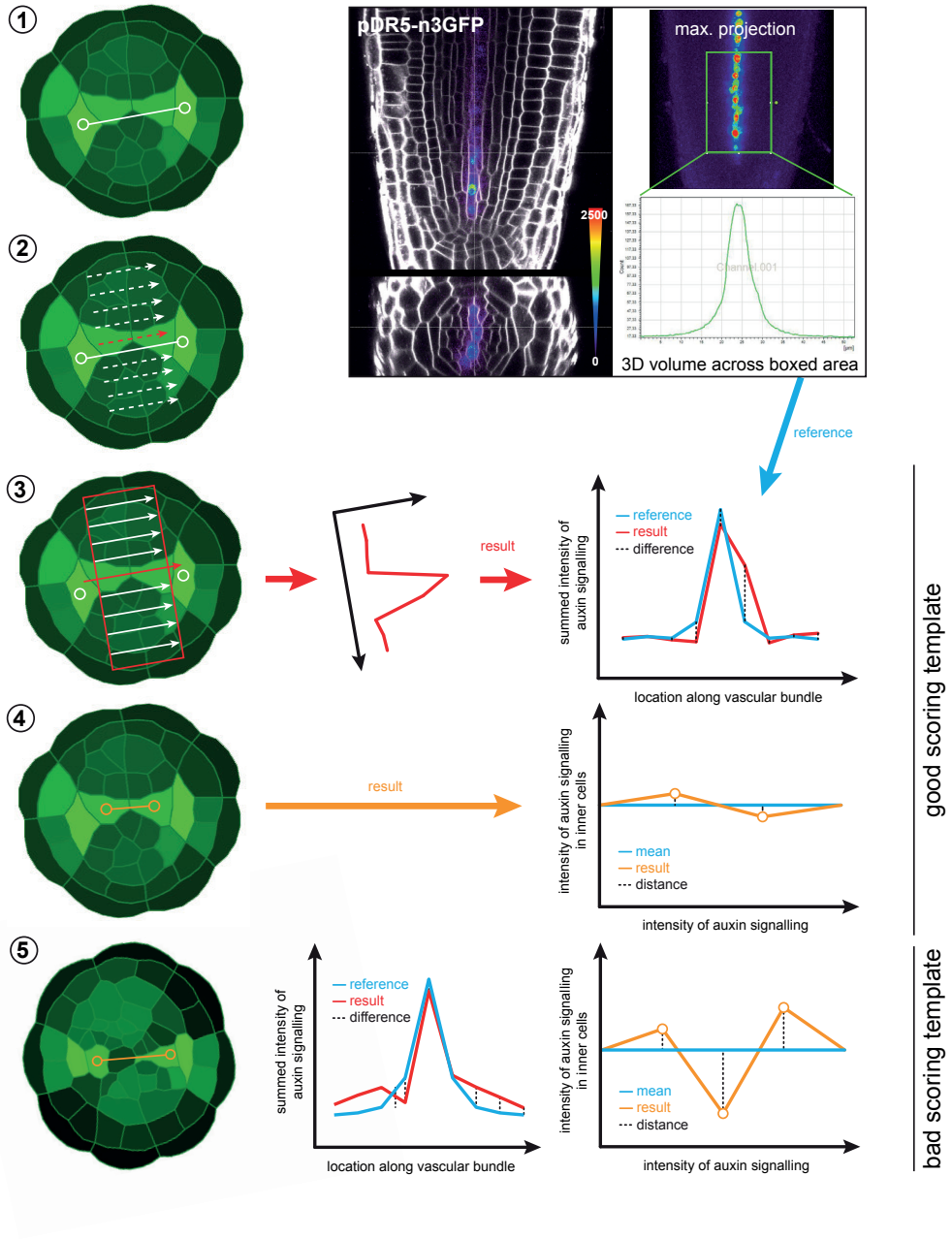

Figure 4-12: Overview of the model evaluation algorithm. Model output is evaluated against two objective. First the central axis of is determine using the line that connected the two centroids of the source cells (A-B). The first objective is calculated by comparing the marginalized auxin profile against a reference profile obtained from experimental data (C). The second objective measures variation along the central axis (D). The latter objective distinguishes a non-continuous axis from the experimentally observed continuous pattern (E).

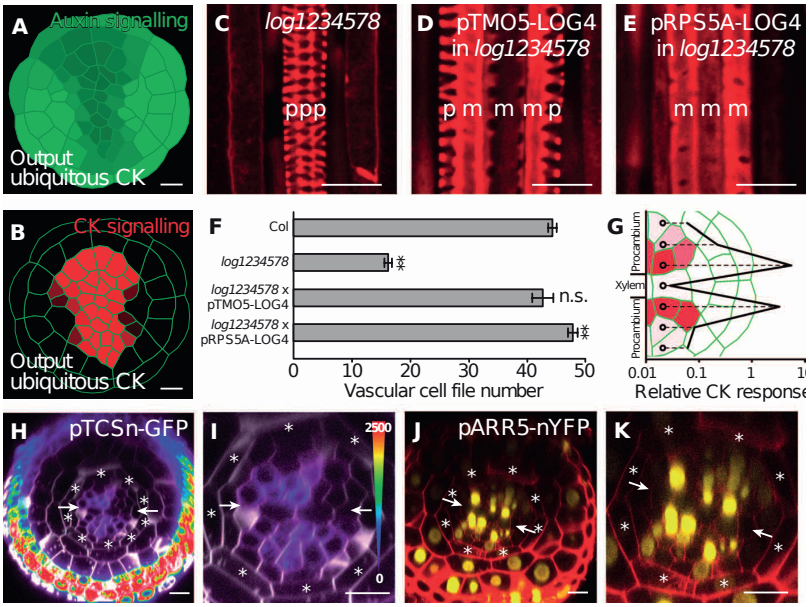

Figure 4-13: Local CK activation integrates patterning and growth. (A and B) Model of ubiquitous CK signaling (representing the TMO5/LHW-OE phenotype). (C to E) Xylem patterns in *log*1234578 mutant roots (C) and *log*1234578 complemented with pTMO5-LOG4 (D) or pRPS5A-LOG4 (E) constructs (m, metaxylem; p, protoxylem). (F) Vascular cell file number in WT (Col-0), log1234578 mutant, and log1234578 complemented with pTMO5-LOG4 or pRPS5A-LOG4 constructs. Error bars indicate SE as determined by two-sided t test (**P < 0.01; n.s., not significant). (G) A relative CK response plot (in log scale) in model output of Fig. 3Q shows a steep gradient emanating from central xylem cells. Note that CK response in xylem cells is very low. (H to K) pTCSn-GFP (H and I) and pARR5-nYFP (J and K) expression in root meristems show differential response. Scale bars, 10 μm (C to E and H to K); those in (A) and (B) are relative to each other.

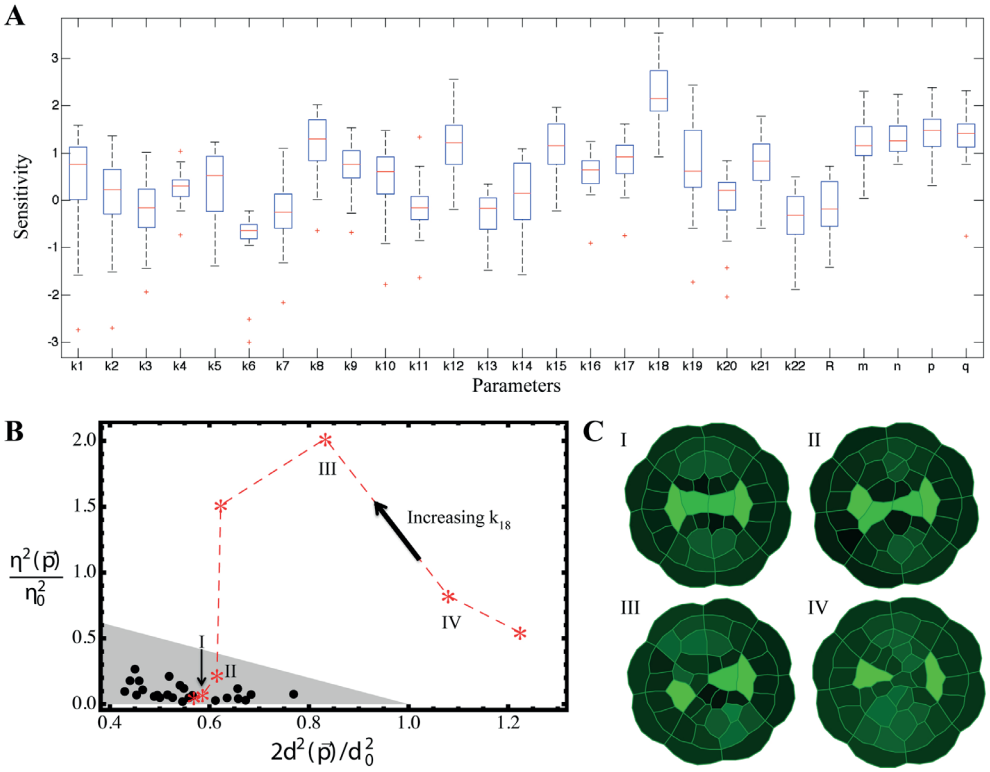

Figure 4-14: Model sensitivity. (A) Box-plot representation of the parameter sensitivities S_i^j on a logarithmic scale. Parameters related to CK signaling are most sensitive (k_8, k_{12}, k_{18}, m, n, p, q). An exception is k_{15} which controls the auxin dependent PIN insertion into the membrane. (B) Scatter plot showing the values of the objectives used in the cost function $\langle L(\vec{p}) \rangle$ for all 25 parameter sets $\vec{p} \in \omega_1$. The gray shaded region denotes the region for which $L \leq 1$ holds. The red dashed line depicts the path resulting from altering the value of k_{18} for the parameter set given in **table S4** (I= $1.5k_{18}$, II= k_{18}, III= $0.1k_{18}$, IV= $0.05k_{18}$). (C) Typical model output corresponding to the points along the path shown in (B).

CHAPTER 5

Theoretical approaches to understanding root vascular patterning: a consensus between recent models

Adopted form the publication in Journal of Experimental Botany, Nov 2016
DOI: 10.1093/jxb/erw410

Nathan Mellor[1,a,*], Milad Adibi[12,*], Sadeer El-Showk[3,4], Bert De Rybel[5,6,7], John King[1,8,9], Ari Pekka Mähönen[3,4,†], Dolf Weijers[5,†], and Anthony Bishopp[1,†]

[1] *Centre for Plant Integrative Biology, University of Nottingham, Sutton Bonington Campus, Loughborough LE12 5RD, UK.*

[2] *Department of Comparative Development and Genetics, Max Planck Institute for Plant Breeding Research, 50829 Cologne, Germany.*

[3] *Institute of Biotechnology, University of Helsinki, Helsinki FIN-00014, Finland*

[4] *Department of Biosciences, Viikki Plant Science Centre, University of Helsinki, Helsinki FIN-00014, Finland.*

[5] *Laboratory of Biochemistry, Wageningen University, Stippeneng 4, 6708WE Wageningen, The Netherlands.*

[6] *Department of Plant Systems Biology, VIB, Technologiepark 927, B-9052, Ghent, Belgium*

[7] *Department of Plant Biotechnology and Bioinformatics, VIB, Technologiepark 927, B-9052, Ghent, Belgium.*

[8] *School of Mathematical Sciences, University of Nottingham, Nottingham NG7 2RD, UK.*

[9] *Synthetic Biology Research Centre, The University of Nottingham, University Park, Nottingham NG7 2RD, UK.*

[*] *These authors contributed equally to this work.*

[†] *Correspondence: anthony.bishoppatnottingham.ac.uk, aripekka.mahonenathelsinki.fi, or dolf.weijersatwur.nl.*

5.1 Introduction

Over the last few years there has been considerable insight into the molecular mechanisms controlling the specification of root vascular pattern. In Arabidopsis embryos, the vascular cylinder forms from a group of four provascular initial cells [71] (Fig. 5.1). As the embryo develops, these provascular initials proliferate through a sequence of highly regulated cell divisions to produce a vascular cylinder of approximately 40 cells by the time the seed germinates. In addition to cell proliferation, cell specification is critical to establish the xylem and phloem cell lineages. These tissues go on to form the main conduit for long-distance transport of water, nutrients and signaling molecules within the plant. As the xylem and phloem initials differentiate a bisymmetric pattern becomes apparent, and this is defined by a central axis of xylem cells flanked by two domains of pluripotent procambial cells and two phloem poles.

Experimental studies have shown that the two hormones, auxin and CK, are essential in mediating both the cell proliferation and specification processes. The auxin response factor *MONOPTEROS* (MP/ARF5) is a central regulator of vascular formation, and mutants lacking this gene show defects in the formative divisions that create the vascular cylinder [143]. Amongst other targets, MP promotes the expression of a basic helix-loop-helix transcription factor, *TARGET OF MOPOTEROS* 5 (*TMO5*) [128]. Together with its homologues, TMO5 forms heterodimers with the LONESOME HIGHWAY (LHW) group of helix-loop-helix transcription factors to determines the frequency and orientation of cell divisions within the vascular cylinder [124, 149].

Auxin and CK also play a crucial role in regulating patterning, and the bisymmetric vascular pattern is the outcome of an initial bisymmetry in the signaling domains of these two hormones. Auxin response is highest in a central line of cells that will go on to become the xylem axis, while signaling peaks in the two domains flanking this axis [101, 123](Fig. 5.1B). Mutants severely impaired in either auxin or CK response lack bisymmetry and display a radially symmetric vascular pattern [101, 123].

These distinct boundaries in the domains of hormonal signaling are maintained by two key interactions. High auxin response directly promotes transcription of the CK inhibitor ARABIDOPSIS HISTINE PHOSPHOTRANSFERASE 6 (AHP6) [123]. In contrast, CK signaling modulates the activity of a group of auxin transfer proteins known as PINFORMED proteins (PINs) [123, 150, 151]. Although the molecular mechanisms governing the control of PINs by CK are not completely understood. CK indirectly regulates PIN7 transcription and modulates the subcellular localization of PIN1 [123, 136, 152].

A second patterning process controls the disposition of the two cell types which make up the xylem axis. Protoxylem forms first at the marginal positions of the axis. It is characterized by the helical deposition of lignin that allows the cells to elongate as the root grows. Once the cells have completed elongation, larger metaxylem cells with a pitted secondary wall structure form in the center of the axis. This patterning of the axis is controlled by an additional group of transcription factors. The transcription factor *SHORT ROOT* (*SHR*) is expressed within the stele and moves to the endodermis where it forms a complex with SCARECROW [153]. The SHR:SCR complex induces the expression of microRNA165/6 which moves into the vascular cylinder and targets the class III HD-ZIP transcription factors, including PHABULOSA (PHB) for degradation [117]. Collectively, these HD-ZIP genes determine proto versus metaxylem identity in a dose dependent manner, but they also interfere with the hormonal patterning mechanism by restricting AHP6 expression [117].

5.2 Why model biological systems?

Molecular research has traditionally focused on individual gene products. However, these products often undergo a complex series of interactions, often in non-linear pathways with multiple feedbacks occurring at both the cellular and tissue scales. Mathematical modeling provides a framework to formalize these interactions and understand how they can generate pattern in both time and space. Whilst mathematical models can serve to “document” molecular

processes and testing the plausibility of interactive networks by recapitulating observed patterns of expression, they have a more powerful role in challenging experimental assumptions and identifying gaps in our knowledge to direct future theoretical and experimental work.

5.3 Previous models of hormone action in the root tip

There have been models of auxin transport for several decades [50] but only more recently has auxin transport been considered in multicellular models at the organ scale. In order to explore the transport dynamics of auxin within the root, a number of independent models of auxin transport have been generated. These both are both based on a structured grids of rectangular cells [154–156]. But differ in the amount of positional information included. In Grieneisen et al., 2007 the first, multiple auxin transporter types are placed within the cells based on experimental observations of multiple PINs [155], whilst in Mironova et al., 2010, a single PIN type is modeled with its synthesis and degradation controlled by auxin (Mironova et al., 2010). Both these models are able to correctly generate an auxin maximum at the root quiescent center. More recent auxin transport models have used realistic root geometries [157] and have used new sensor lines [158] to incorporate a more detailed understanding of where auxin is localized within the root. In the mature root, while PIN levels change in response to perturbations, PIN polarity seems to be fixed, therefore most models of auxin action in the root are not concerned with formation and regulation of PIN polarity. These studies have shown that, in addition to the PIN proteins controlling auxin efflux, a group of auxin importers (AUX/LAX) is also required to recreate the pattern of auxin seen at the root tip. In general these models have all focused on the longitudinal flow of auxin; whilst there have been some models considering the radial flow of auxin in outer tissues [154, 159] these have not studied radial auxin flow through the vascular tissues. There have also been models which consider the crosstalk between auxin and CK, initially within the context of a single cell, but later in a one-dimensional line of cells. There

have been several models that have combined auxin and CK signaling networks within a single cell [160, 161].

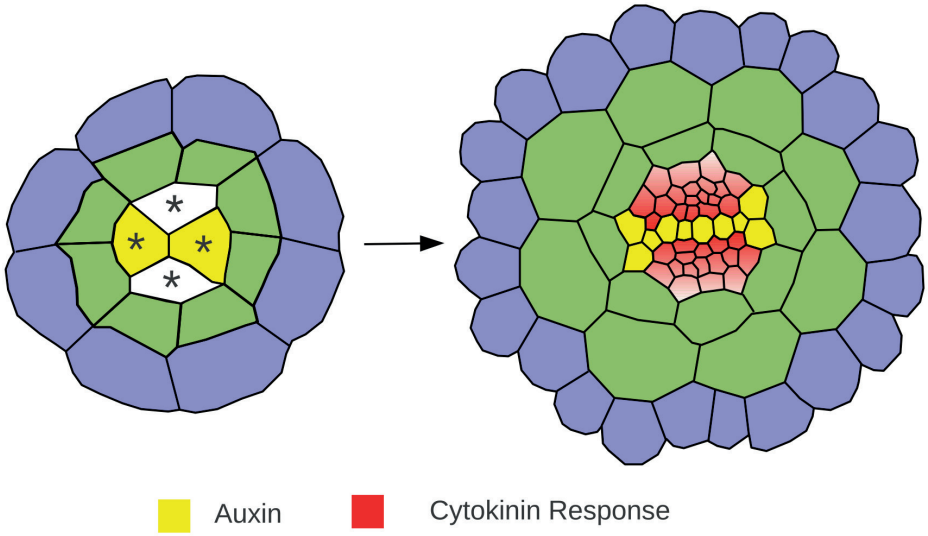

Figure 4-15: Schematic diagram showing cross sections taken through an embryo (left) and mature root (right) showing how four provascular initial cells (labeled with asterisks) give rise to a fully patterned vascular cylinder. Cells with high auxin response are shown in yellow and cells with high CK response, in red. The epidermis is shown in blue and the ground tissue in green. Note the "bridge" in the embryonic cross section between the two cells with high auxin response. It is necessary for these cells to have a shared cell wall for simulations to produce a correctly patterned xylem axis. Image reproduced with permission from (Mellor and Bishopp, 2014).

5.4 Modeling Root Vascular Patterning

In the last two years, there have been three independent publications modeling root vascular patterning in Arabidopsis. At first glance these models might seem redundant, but each model asks different questions and provides novel insights into the system. In this review, we explore the commonalities between these models as well as investigating their differences. We also run new simulations to test whether findings of specific models are supported by the different modeling approaches. Finally, we discuss specific areas where there is as yet no clear consensus

and highlight areas where future experimental programs may provide new insights.

The first of the three publications considered here, by [134], uses both a two-cell template and a multicellular geometry to identify a minimal gene regulatory network involved in establishing and maintaining vascular pattern. The second, by [72], builds upon this patterning mechanism to explore how root vascular pattern is established and develops during embryogenesis. Importantly, it considers both cell growth and division and provides new data showing how auxin and CK interact. The final publication, by [162], focuses on auxin transport in a spatially realistic model incorporating hormonal regulation of the auxin transporters. Hereafter, the three models are referred to as the Minimal Framework model [134], the Growing Root model [72] and the Auxin Flux model [162]. A summary of the network configurations in the different models is given in Fig. 5.2.

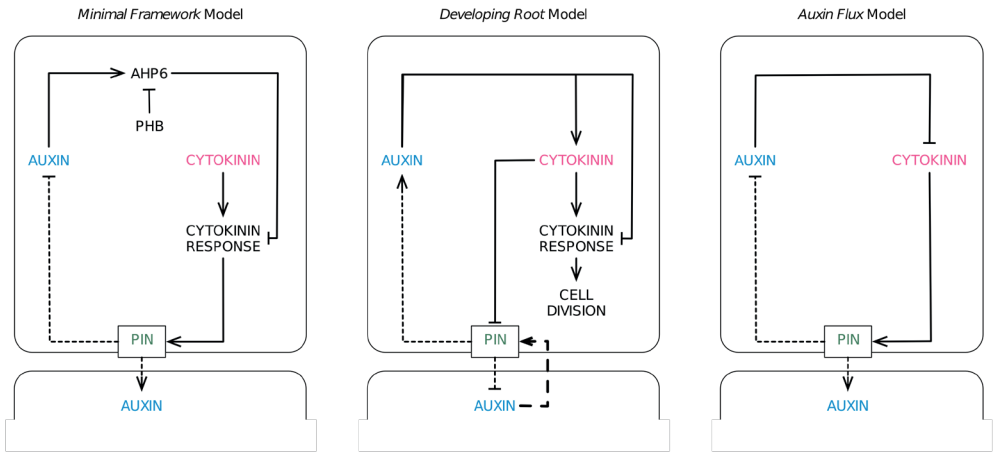

Figure 4-16: Schematic diagrams showing the network configurations of the three vascular patterning models. These have been re-arranged from the original figures to aid comparison between models. Activation or repression is shown with solid lines. Dashed lines indicate transport of auxin into and out of the cell, with the arrowhead indicating whether it promotes or inhibits auxin accumulation within that cell. The long dashed lines indicate a mechanisms by which PIN proteins are polarized within a cell in a manner dependent on the concentration of auxin within neighboring cells (see text). Although only 2 cells are shown, these models are all embedded within multicellular templates.

5.5 Model construction

Mathematical models will always be an abstraction of complex biological systems. There is never a clear answer as to how detailed to make them, and different teams will always take different approaches regarding how much information to include, depending on the question being addressed. A summary of the different network configurations is given in Fig. 5.2. The Minimal Framework model seeks to understand the interaction between molecular components and how these interact as a network to control pattern. To this end it includes each key class of molecule modeled explicitly. This has the advantage of providing greater insight into the molecular circuitry, and indeed this model has led to new insights into the patterning of AHP6 by a PHB-miR165/6 module that has not been considered in the other models.

In contrast, the Auxin Flux model addresses a different question, asking how the hormonal activation of auxin transport is regulated in a spatial context. In terms of spatial structure this is the most comprehensive of the three models as it offers the most detail in terms of compartmentalization of cells, by considering the apoplast as a separate compartment. In contrast the molecular network in this model is designed using the most conservative approach of making the most parsimonious model of vascular development possible. Essentially, the model uses as few molecular components as possible whilst maintaining the ability to address the biological question. In this model, no distinction is made between hormone levels and hormone signaling output. Some key components such as AHP6 are not modeled as discrete components; instead, AHP6 is handled via a generic repression of CK in response to auxin.

The Growing Root model asks how hormones control tissue development and as such it is essential to use a growing template to investigate both the effects both on cell growth/proliferation and also on cell patterning. Since a new role for auxin-mediated CK biosynthesis is an essential finding of this paper, and the authors investigate this by separately modeling CK levels and CK response separately, enabling the two processes to be differentiated. However, they take a more parsimonious approach to some elements of their model where modeling would be unlikely to

provide critical insights, applying a generic repression of CK signaling by auxin (similar to the Auxin Flux model) and simplifying chains of interaction.

The three models used different modeling platforms: the Minimal Framework model was built using OpenAlea [163], the Growing Root model used Virtual Leaf [9], and the Auxin Flux model was a Cellular Potts based models. The first two approaches are the most similar as they are both vertex-based. Geometrically, such models are comprised of polygons, with each polygon representing a distinct cell; a set of Ordinary Differential Equations (ODEs) determines the molecular processes occurring within each cell, and components can move between cells based on a set of terms in the ODEs governing the permeability across membranes or cell vertices. Cellular Potts models differ in that cells are comprised of a number of pixels or voxels arranged in a grid and thus have internal space; in addition, the apoplast is explicitly included in the model. Whilst the vertex-based approaches simulate movement of molecules purely as permeability across a membranes. In contrast, the Cellular Potts-based model, also allows the the investigation of diffusion within a cell and in the apoplast. Simulating the diffusion within cells has previously been shown to be important in templates with larger cells, such as those considering root bending or lateral root initiation [164]. In general vertex-based and Cellular Potts models have similar capabilities in a static setting, the major differences emerge when they are used to model cellular growth. This discussion is not within the scope of this paper and is covered in detail elsewhere [165, 166].

5.6 A Minimal Molecular Framework for Vascular Patterning

The Minimal Framework model [134] investigated the feasibility of an auxin-CK mechanism as a control of tissue specific patterning, first in a two-cell system but later in a multicellular template. The two-cell system was based on a pair of identical cells with a shared interface through which auxin and CK could diffuse or, in the case of auxin, be transported through polar auxin transport. Within each cell a series of equations calculated how the various components

(auxin, CK, AHP6, PIN7) interacted to determine the steady state solutions for each cell. For simulations run with extremely high/low levels of either auxin/CK only one possible steady-state solution existed, in which both cells would have similar outputs. For example, extremely high auxin levels resulted in both cells expressing high levels of AHP6 and having negligible CK response. However, for a large subset of intermediate conditions, multiple steady state solutions existed in which one cell had high AHP6 and the other cell high PIN7. The presence of multiple steady state solutions suggest that the system can act in a 'switch like' manner to determine discrete domains of gene activity, and reinforces the concept that the auxin-CK interaction can act as a patterning mechanism. However, this two-cell approach does not address how these patterns could look in a realistic tissue.

To introduce this model into a multicellular template, a series of simulations were run in which the expression/localization of PINs were fixed based on experimental observations and were not regulated by the model in order to explore genetic redundancy between the PINs. In an effort to simplify an otherwise complex network, later included only a single PIN type whose activity was based upon that of PIN7. During this work, the authors assumed a flat field of both CK and auxin production, although subsequent work has shown this not to be the case. In order to direct pattern formation, an initial asymmetry was required; this was supplied through an initial pre-pattern in PIN7 expression. An experimentally defined network of auxin and CK regulation, including the regulation of AHP6 by PHB [117], was not sufficient to recreate the stable domains of gene expression as seen in roots. However, the authors were able to stably reproduce the observed patterns of gene expression by making two changes to this network configuration. The first involved altering the way in which PHB and microRNA165/6 interact. The introduction of a mutual degradation between these two components was required in order to produce stable gradients that could restrict AHP6 sufficiently restrict AHP6 to the marginal positions. The second change involved the incorporation of an additional, as yet unidentified, inhibitor of CK (termed CKIN). This was required alongside AHP6 to restrict CK response, and therefore PIN7, in the central parts of the xylem axis. At the time, the authors proposed that

this component could target either CK biosynthesis or signaling; however, subsequent studies suggest that the former is unlikely.

The revised network could reproduce a stable vascular pattern, but it required an initial asymmetry in PIN7. To test the robustness of this system, the output from a previous simulation was used as a set of initial conditions that closely resembled the pattern of gene expression seen in wild-type roots. Simulations were then run to steady state in a system in which every cell had the potential to express PIN7. These simulations revealed that the initial vascular pattern was maintained, suggesting that the network provides a robust mechanism for maintaining pattern around an initial asymmetry, even though it does not generate the initial asymmetry, or address its possible causes.

5.7 Early events specifying the xylem axis

This question was addressed in the Growing Root model [72] by investigating how the xylem axis was specified during embryogenesis. The model incorporated both growth and patterning within a dynamic array of cells. This study identified a crucial new interaction through which auxin promotes the transcription of the LONELY GUY 4 (LOG4) gene via the TMO5/LHW dimer (De Rybel et al., 2014). *LOG4* is a crucial enzyme involved in the final stages of the CK biosynthesis pathway and is believed to be the rate-limiting step during CK homeostasis [125]. *LOG4* is expressed in all four of the vascular initials, but in the growing root it is expressed throughout the xylem axis, suggesting that the xylem axis acts as a source of CK [72]. Although this model regulates both growth and patterning, it is likely that it achieves these activities via two independent CK responses. In this model CK signaling promotes periclinal cell division. PIN localization is regulated via CK directly, in what the model assumes to be an independent CK response pathway. The PIN dynamics differ from those used in the Minimal Framework and Auxin Flux models; CK mediates the inhibition of PIN1 localization [136] rather than inducing expression of PIN7. Furthermore, PIN1 is also polarized in response to auxin gradients, as

has been done in some other models [51]. In this model, xylem cells are capable of producing CK via TMO5/LHW via TMO5/LHW dependent activation of *LOG4*. As a result of mutual interaction between cell growth and the reaction network, the production of CK is constrained to the developing xylem axis in model simulations. As a result of high auxin levels in the xylem axis, CK signaling is inhibited in these cells, which results in suppression of periclinal cell division.

The model itself comprised a combination of two interconnected feed-forward loops that controlled both growth and patterning. The first feed-forward loop considered CK rather than CK response to control PIN regulation and cell growth. The second feed-forward loop incorporated the interaction between auxin and CK response to control periclinal cell divisions. When applied to a template consisting of four provascular initial cells these interconnected loops were sufficient to recapitulate both the growth and patterning processes necessary to create an axis of high auxin response in a growing template. However, this required two additional inputs within the initial four-cell template. The first was a bias in which auxin was elevated in two source cells representing the convergence points of the cotyledons. Second the two source cells had to be connected by a small bridge (see Fig. 5.1), an assumption that subsequent experimental analyses have shown to be valid. Not only can these simulations recreate experimental observations based on limited prior information, but the simulations also showed gradients in both CK and CK response, with the highest CK response in the cells adjacent to the xylem axis. Whilst some of our CK markers are not sensitive enough to reflect this gradient, re-analysis of others has shown such a gradient.

5.8 A parsimonious model of auxin fluxes

The Auxin Flux model [162] delves much deeper into the concentration and flux patterns of auxin. Whilst the previous models only considered a single PIN protein, this model included PIN1, 3 and 7 with a combined role for PIN2 and the PGPs. It also incorporated a generic

auxin importer to account for AUX1, LAX1 and LAX2. The Auxin Flux model incorporates CK-mediated upregulation of PIN7 in a similar way to the Minimal Framework model. However, the role of AHP6 is simplified in this model; instead of explicitly modeling AHP6, the linear chain between auxin, AHP6, and repression of CK-mediated PIN activation is simplified to a generic repression of PIN7 and PIN1 by auxin.

Using a series of so called "static simulations", in which the auxin transporters were localized as observed experimentally but were not regulated by the hormone, the model was able to recreate patterns of auxin response similar to those seen experimentally in wild-type roots. However, static simulations run in the *woodenleg*(*wol*) mutant [130], which almost completely lacks CK signaling response, did not recreate the auxin response patterns observed patterns in mutant plants; hormonal regulation of transporters in "dynamic simulations" was required to recapitulate the correct pattern. Further analysis revealed that the difference between the static and dynamic simulations resulted from differences in the diffusion of auxin through the apoplast. The authors also simulated the outcome of a mutation in the auxin importers. While auxin still accumulated in the xylem axis in these mutations, the concentration was much lower. This led the authors to suggest that xylem specification might be unstable in plants with impaired auxin transport, a finding they confirmed experimentally, as *aux1 lax1 lax2* triple mutant plants were found to have unstable pattern formation.

Although the Auxin Flux Flux model focused on vascular patterning in the root tip, it provided unexpected insights into the process of lateral root priming. Lateral roots originate from the pericycle cells flanking the xylem poles [167]. In the model, certain subcellular arrangements of PIN1 generate an Auxin Flux circuit that not only allows the xylem pole pericycle cells to accumulate auxin at the expense of the xylem axis, but also allows the two poles to compete against each other for auxin. While this dynamic provides a potential mechanism to prime lateral roots, future work is needed to experimentally assess the subcellular status of PIN1 and to evaluate the Auxin Flux circuit in simulations of a growing, three-dimensional root.

What initial conditions are required to set vascular pattern? All three models require an

initial asymmetry in order to establish the vascular pattern, but each addressed the asymmetry differently. In both the Minimal Framework and Auxin Flux models, an initial asymmetry was required to generate the vascular pattern, which was provided from an initial pre-placement of PINs. Furthermore, in the case of the Minimal Framework model, this initial asymmetry is required only required transiently; once established the system is able to maintain a stable pattern, even after the asymmetry is removed. The Growing Root model, in contrast, uses a persistent asymmetry in auxin input to drive pattern formation. Two of the four vascular cells continuously receive continuously higher auxin input than other cells in the vascular bundle, based on the observation that symmetry breakage first occurs in the apical part of the embryo and leads to an asymmetric production and transport of auxin at the incipient cotyledon, as cells immediately subtending the cotyledons have been shown to have higher auxin response [72], whilst mutants with altered numbers of cotyledons have been shown to generate roots with irregular numbers of xylem poles [141]. A key question, which we now investigate with a new set of simulations, is whether a transient auxin input can be used to drive patterning in the Minimal Framework model.

To test this, we reran the minimal Minimal Framework Framework model using the original parameters and allowing each component (including PIN7) to be expressed in any cell, but with an initial condition of high auxin at both protoxylem cells and all four xylem- pole pericycle cells, where high AHP6 expression has been observed. The production rate of auxin is uniform throughout the tissue. We made one additional change to the model. In the original model we had a hypothetical component termed 'CKIN' that acted redundantly to AHP6 to inhibit CK in the metaxylem. We changed this from a repressor of CK levels to a repressor of CK response in keeping with the subsequent discovery of the xylem as a source of CK. With these changes, the resulting steady state pattern of AHP6 expression closely resembles the initial conditions with only a minor shift in the position of the xylem axis (Fig 5.3). These simulations support the idea that an asymmetry in auxin drives pattern formation in the root but suggest that such an asymmetry is required only transiently. Whilst in the embryo and primary root of Arabidopsis a

the continuous transport of auxin from the cotyledons/pre-existing vascular is likely to provide a continuous asymmetry in auxin input as incorporated within the Growing root Root model, this is not necessarily the case in newly formed roots (such as lateral or crown roots) or during pattern specification in other plant species with three or more vascular poles. To investigate the importance of a continuous asymmetric auxin input for functionality of the growing root model, we ran model simulations using a transient asymmetric auxin input; the model does not produce the correct pattern of auxin and CK. However when run in a static template (Fig. 5.4B), the same simulation produces the correct CK and auxin patterns. The results from the growing model suggests that continuous asymmetric auxin input is necessary during establishment of vasculature, while this input is not required in later stage and in mature root to maintain auxin and CK signaling domains. We feel that the observation that transient changes in auxin can be propagated as stable changes in vascular pattern will allow future models to address this process in other species.

5.9 The xylem axis as a source of CK

Although there are multiple markers for observing CK response at a cellular/tissue scale, there are no methods for imaging the location of CK itself at this resolution. Although the Minimal Framework and Auxin Flux models could produce stable patterning with a homogenous field of CK production in each cell, experimental results published with the Growing Root model showed that the xylem provides the major source of CK. One output of the Growing Root model is that by driving CK synthesis in the xylem axis only in the xylem axis, it is possible to create a gradient of CK across the vascular tissues. Does such a gradient exist in plants and is it required for patterning? Analyses of independent CK responsive marker genes suggest that a gradient in CK response does occur, but the current technology does not allow us to know whether this is mirrored by a gradient in CK itself. The presence of a CK gradient in these tissues is a question where there are different viewpoints between the authors.

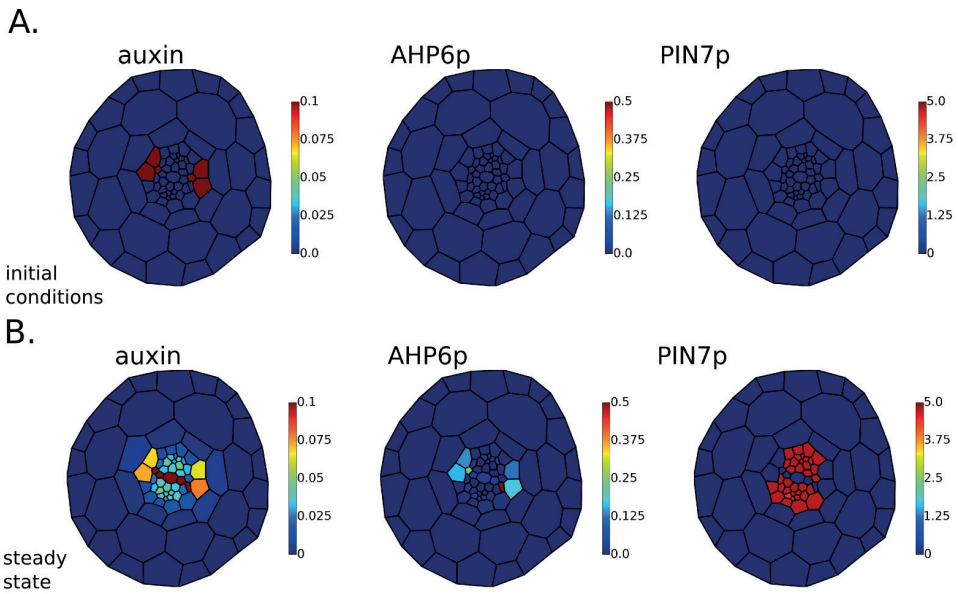

Figure 4-17: Initial conditions (A) and steady state values (B) of a simulation using the Minimal Framework model with the previously published parameter values. Rather than pre-patterning via PIN7 localisation as in Muraro et. al. 2014, the model is primed by having high auxin in the protoxylem and xylem pole pericycle as an initial condition, after which the production rate of auxin is equal in all cells. The model is able to pattern two poles of AHP6 either end of the xylem axis, with only a small change to the initial pattern provided. Colour ranges show arbitrary nondimensional values.

The Growing Root model investigates both cell division and patterning through regulation of the PINs. Although CK regulates both of these processes it is likely that it does so using different downstream regulatory components; CK-mediated patterning and cell proliferation are therefore handled separately in the model. As little is known about the mechanism through which CK regulates PIN1, this was modeled as a direct interaction between CK and PIN1 based on data from lateral root organogenesis [136]. This simplification was introduced in order to reduce unnecessary parameters, although subsequently it has since been shown that this interaction is dependent on CK signaling rather than being a direct activity modulated by the hormone itself [136]. Within the Growing Root model, a gradient of CK promotes increased polarization of PINs away from the xylem axis is instructive in polarizing the PINs. Here we test whether a gradient of CK is an absolute requirement for this model.

By running simulations in the Growing Root model with increased CK diffusion, we were able

to observe that the correct output can be achieved with much shallower gradients than were previously published. In the most extreme simulations CK diffusion could be increased up to 40x-fold with levels and maintain correct patterning (Fig. 5.4A). Nevertheless to specify pattern correctly there is a requirement for CK levels to be higher in the xylem than in adjacent cambial cells. The idea that only a shallow gradient of CK is required is appealing as, although the majority of LOG activity is within the xylem axis [72], other sources of CK are likely to exist. In reality multiple modes of CK-mediated PIN activity likely co-exist in plants and further experimental analyses documenting the exact interaction between CK and individual PINs is needed. Collectively these simulations show that a shallow gradient of CK is required in simulations incorporating PIN1-like regulation, as this appears to be the most important PIN during embryonic root formation [137], it is possible that there are different requirements for CK gradients during the formation of embryonic and mature roots. These studies highlight the need for detailed analyses analyzing exactly how each PIN responds to CK in specific tissue types. Whilst this is feasible for the growing root, it provides a significant technical challenge to investigating this process during embryogenesis.

A gradient of any molecule within across a multicellular tissue is possible providing it is synthesized (either exclusively or at higher levels) in a group of source cells and that the molecule must moves between cells (e.g. via diffusion). The slope of the gradient results exclusively from the balance between the rates of diffusion and degradation. A molecule that diffuses very quickly or degrades very slowly will form a shallow gradient or become homogenously distributed throughout the tissue; a slower rate of diffusion or quicker rate of degradation will form a steeper gradient. The identification of the xylem axis as a key source for CK provides a group of source cells, but what kind of gradient forms around this source?

The identification of the xylem as a key source for CK production clearly meets the first criterion, but how about the second and third criteria? This depends on two critical parameters, CK diffusion and CK degradation. Unfortunately as we are unable to visualize individual molecules, the degradation rate and diffusion coefficient of CK are both unknown. In the Auxin

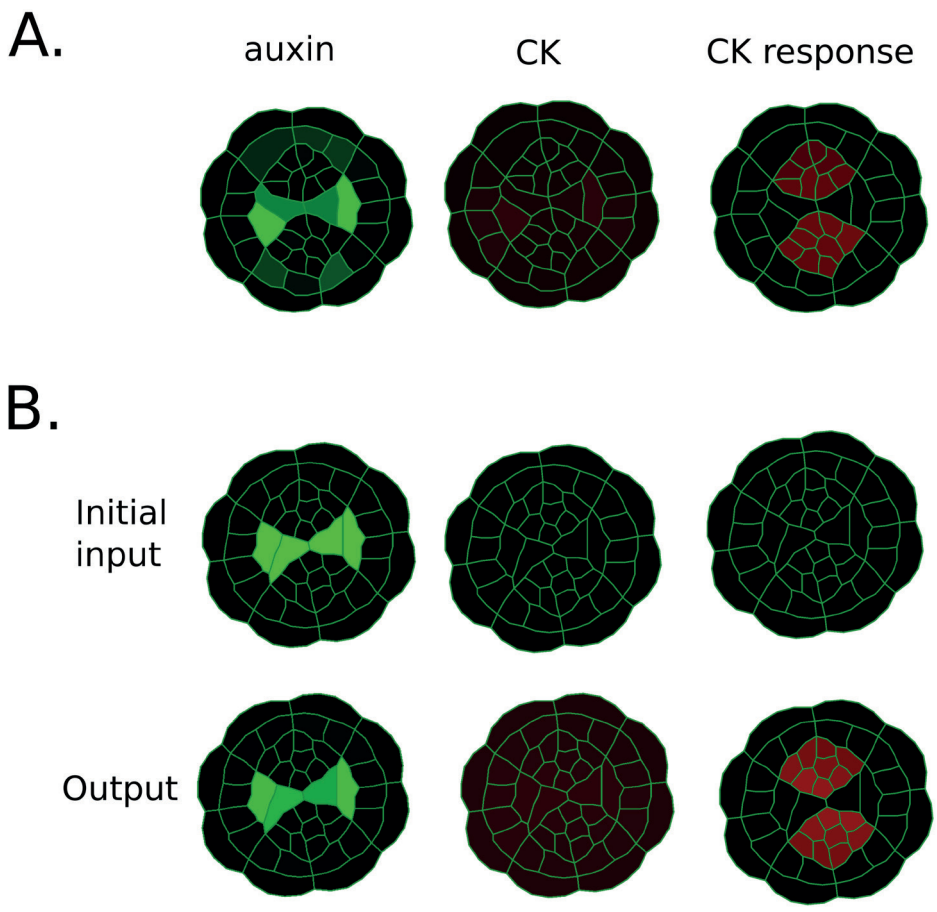

Figure 4-18: (A) Output of a Simulation using the growing model where CK localization on cell wall is upregulated via CK signaling. The correct patterns of auxin and CK signaling is obtained, while CK forms a homogeneous gradient throughout the cellular template. Parameters used in this simulation are listed in supplementary information. (B) Results of a simulation of the growing root model in a static template with a transient high auxin input within the xylem axis. The initial asymmetric transient auxin input is sufficient to establish the correct patterns of auxin and CK within the template.

Flux paper the authors argue that parameters required to generate a informative gradient of CK in tissues the size of an Arabidopsis root requires are unrealistic. Since all three models only include passive movement of CK via diffusion, the choice of these parameters is critical for determining the shape of the resulting gradient; however, problems arise because these parameters are simply unknown.

5.10 Can a gradient of CK exist?

In the Minimal Framework and Growing root models, movement of chemicals between cells is governed only by permeability across a membrane. In the Auxin Flux model, movement also occurs via diffusion within cells and in the apoplast, arguably giving a more realistic modeling of diffusion. This is of particular importance for hormonal signaling since, at least in short-range, signaling molecules are thought to propagate faster apoplasticaly than symplasticaly [168]. The Auxin Flux model uses the same diffusion co-efficient for CK and auxin based on the rationale that they are similar sized molecules. Although the parameter for auxin diffusion has been used in other computational models and is based on experimental values, these were not measured in plants but were generated using a polar membrane created between egg lecithin and decane [169]. Within this system, diffusion was dependent on pH and the rate of Auxin Flux across the membrane was increased as through conversion of auxin to an ionized form at the membrane surface. Whilst these may represent the "best estimates" of CK diffusion, they are open to debate and only direct measurements will be able to provide irrefutable parameters. Since an informative gradient would require that the CK diffusion or degradation rates differ by several orders of magnitude from those used in the Auxin Flux model, the authors carried out an experiment to establish a lower limit on the diffusion of CK. They treated roots with exogenous CK and measured the change in CK response within the root; CK response increased in both the outer and inner layers of the root within six hours, suggesting that CK can traverse the radius of the Arabidopsis root in a matter of hours [123]. This is a rate of CK movement which is incompatible with the formation of an informative CK gradient via diffusion unless the degradation rate is also orders of magnitude higher; however, such rapid degradation would also place limits on how far CK could travel and would affect the time scale of regulatory networks. The authors therefore suggest that other mechanisms, such as active CK transport or uneven expression of the CK perception machinery, might be responsible for the observed CK signaling patterns.

Although the models use a different system for dealing with diffusion, the Auxin Flux model was able to reproduce the gradient formed in the Growing Root model with an appropriate choice of parameters. We therefore endeavored to evaluate the questions of whether the xylem axis can act as a sole source of CK and whether an informative CK gradient can exist using the Minimal Framework model.

To reconcile these findings and test whether the xylem axis could function as the sole source of CK we ran new simulations in the Minimal Framework model with CK production restricted to the xylem axis. As before, we provide an initial asymmetry in PIN localization and then test the robustness of any pattern by removing this restriction on PIN placement. Using the original model parameters produces a sharp gradient of CK away from the xylem axis, resulting in very low PIN7 expression except in the protoxylem, and AHP6 expression spreads throughout the pericycle and adjacent cells in the stele. (Fig. 4.5A).

As discussed above, while the Auxin Flux model uses a diffusion coefficient in a Cellular Potts model to simulate CK movement within and between cells, the other models only simulate movement from cell to cell using a permeability parameter. We estimate that based on an estimated average width of cells in the cross section of 30μm, the diffusion coefficent used in the Auxin flux Flux model of Dck=600μm $4s^{-1}$ would correspond to a permeability, Pck =20μm s^{-1} in either of the other models. Based on an approximate average width of the cell layers in the cross section of 30μm , we estimate that, for a given CK production and degradation rate, the CK distribution in the Auxin Flux model with Dck=600μm2 s^{-1} can be reproduced in the other two models with Pck =20μm s^{-1}. Similarly we predict the results with permeability Pck =10μm s^{-1} used in the minimal Minimal Framework Framework model can be roughly reproduced in the Auxin Flux with an estimated effective diffusion coefficient of 300 μm2 s^{-1}. Though this effective diffusion coefficient is of the same order of magnitude to that used in the Auxin Flux model, CK degradation (dck), the other key parameter in determining the sharpness of any CK gradient, is much higher in the Minimal Framework model than in both the Growing Root and Auxin Flux models, resulting in the sharp gradient in (Fig. 4.5A). Although the exact data

regarding the turnover of CK is not available, reducing this in line with the other models (from 10 s^{-1} to 0.1 s^{-1}), so that it degrades over the time scale of minutes rather than seconds, results in improved patterning of the xylem axis (Fig. 4.5B). A further adjustment, so that the level of CK in the procambium regions is closer to that in the published model, results in the correct patterning of the root vascular cylinder and the formation of a gradient of CK peaking within the xylem axis (Fig. 4.5C).

Using the parameters from the Auxin Flux model (CK production pck = 0.001 arbitrary units s^{-1}, degradation dck = 0.0001 s^{-1}, estimated permeability Pck =20μm s^{-1}) in the Minimal Framework model with CK production restricted to the xylem results in little or no gradient in CK, but also no regular pattern due to insufficient overall levels of CK (Fig. 4.5D). However, when raising the level of CK production to pck = 0.003 arbitrary units s^{-1} , while there is still no CK gradient, the overall level of CK is raised sufficiently so ensure that the correct pattern is generated and maintained robustly (Fig. 4.5E).

As these new simulations required a change of parameters, we tested the sensitivity of the three key parameters relating to CK activity: CK production (pck), CK degradation (dck) and CK permeability (Pck). Using the value of Pck from the Minimal Framework model (Pck =10 μm s^{-1}) as a starting point we found ranges of the other two parameters, pck and dck, for which the correct pattern is maintained robustly. To assess whether the pattern is formed correctly we use k-means clustering to categorize cells into two clusters based on the level of AHP6 protein. If and only if the cluster of cells with the highest AHP6 level is exactly equal to the set of six cells comprising the two protoxylem and four xylem pole pericycle cells do we conclude the model has patterned the tissue correctly.

Plotting the region of two-parameter space for which the correct pattern is formed (Fig. 4.5F) shows that, with the permeability Pck =10 μm s^{-1}, no pattern can be formed for degradation rates above around dck = 0.22 s^{-1}. Below this degradation rate there always exists a range for which patterning occurs. This shows that while the model is able to form a pattern with very shallow or intermediate CK gradients, when the CK degradation rate is too high, the CK

gradient away from the xylem axis becomes too steep to be able to maintain a stable pattern. We also note that for a given degradation rate below the threshold value, there is only a relatively narrow range of CK production that will support a pattern. This parameter does not affect the CK gradient, but instead determines the overall level of CK in the tissue. Since PIN7 is sensitive to the level of CK, if production is too high PIN7 expression dominates throughout the stele, while if it is too low AHP6 expression dominates instead. The narrow range of viability to form the correct pattern further illustrates the importance of the regulation of CK production as shown by [72]. Similarly shaped regions of parameter spaces, but with different numerical ranges are produced when repeating the exercise using the permeability from the Growing Root model (Pck =0.1 μm min-1) and the estimated representative permeability from the Auxin Flux model (Pck =20 μm s^{-1}) (see supp info).

If CK is expressed evenly throughout the tissue, rather than just in the xylem axis, it is still possible to produce the desired pattern of AHP6 expression. Plotting the region of two-parameter space for which the desired pattern occurs as before we see that while for a given CK degradation rate there is a corresponding range of production rates for which there is the correct, stable pattern, there is no upper limit on the degradation rate, as is the case when production is limited to the xylem (Fig. 5.5G).

Together these simulations suggest that, whilst restricting CK production to the xylem axis is a plausible method for vascular patterning at least in the Minimal Framework and Growing Root models it is not an absolute requirement for the patterning process.

5.11 Conclusion

The organization of root vascular tissues provides a fascinating model to investigate how patterns form in multicellular structures, and the surge in research in vascular development is testament to this. Experimental studies have identified the key components involved in this process and determined how they interact. More recently theoretical studies have investigated

these non-linear interactions and feedback mechanisms and revealed how they collectively determine patterning output. Whilst each of the models incorporates known values where possible, all models by necessity rely on parameter estimation. To address the uncertainty of these parameters, each of the models has made an exploration of the parameter space required that allows patterning. Whilst there are some areas where the authors favor alternative hypotheses, on most issues the three models are largely in agreement. All three models support the interaction of auxin and CK as a plausible system for generating pattern. The exact wiring of this system varies, and this largely depends upon the different questions that each model pursues. In this paper we ran new simulations to test the findings of the different models. Although the three models use quite different platforms, it is reassuring to see that the several findings are transferable across these platforms. Collectively we feel that our modeling efforts support the hypothesis that an asymmetry in auxin input can direct the formation of vascular pattern. We agree that the correct pattern can be generated using the xylem axis as the sole source of CK, but other sources of CK do exist and our simulations in this paper show that broader patterns of CK production can also pattern the root. We do not have a consensus of whether there is a meaningful gradient of CK present in the root; however, we show that a CK gradient is required only required with certain configurations of PIN dynamics, and even then correct patterning can be generated from a very shallow gradient. Moreover, the theoretical dispute about the formation and presence of a CK gradient presents a challenge to be resolved by experiments; we hope that future work will either show that the parameters relevant to CK diffusion are in the range to form an informative gradient or demonstrate that CK is patterned by an alternative mechanism. We have also highlighted several other key areas that need further research, namely further insight into how CK regulates PIN activity and the factor(s) that operate alongside AHP6 to limit auxin response in the xylem axis.

The three independent modeling approaches together offer considerable insight into the patterning process. All models support each other in some aspects; but at the same time each model provides new insights into the network that are unique to that model. In a few areas

they find disagreements. By comparing the three modeling approaches, we are able to focus future experimentation on aspects where the modeling has indicated that there is additional complexity. We believe that the approach of integrating multiple independent models of root vascular patterning serves as an exemplar for understanding other developmental processes in plants.

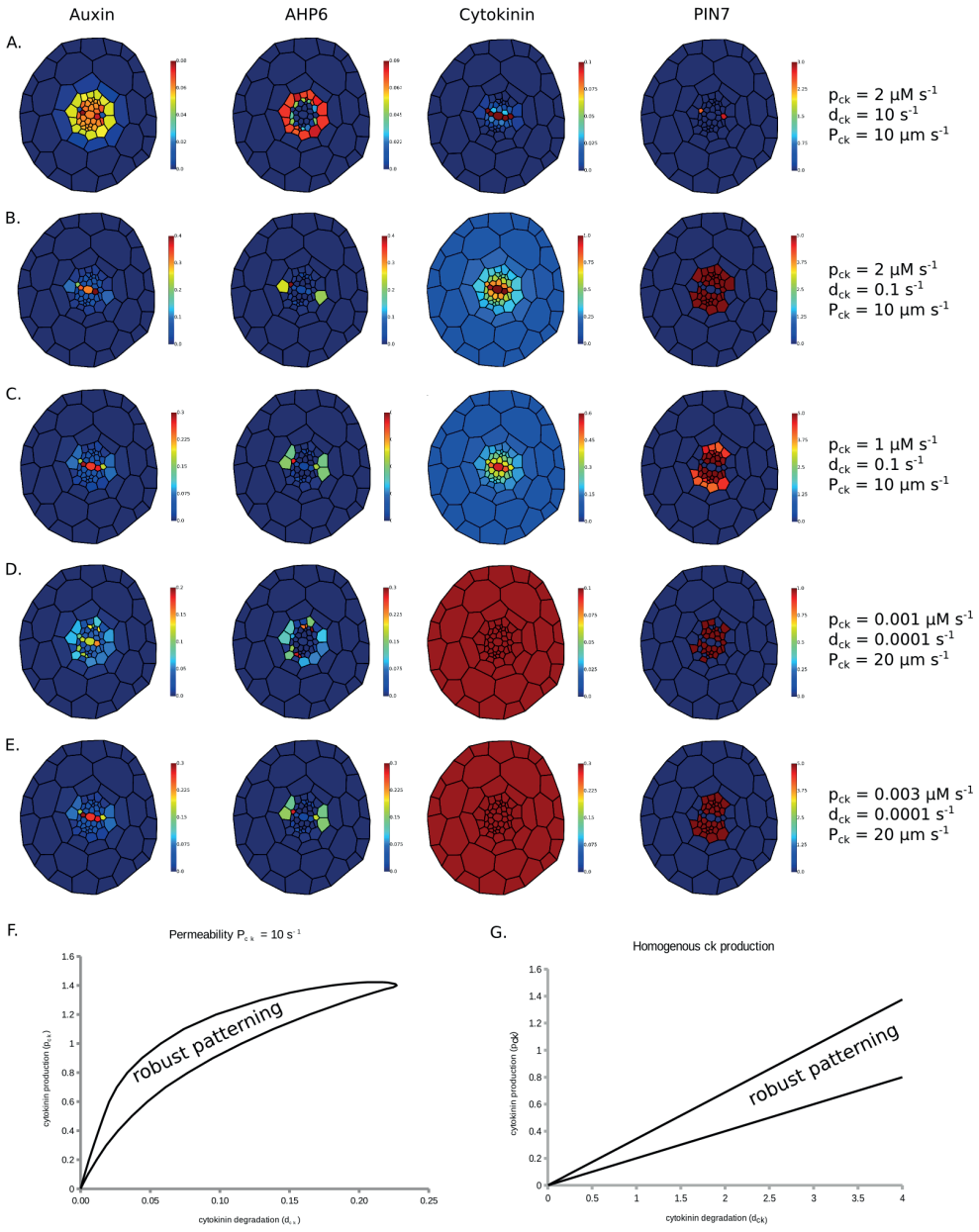

Figure 4-19: Output from the Minimal Framework model with CK production limited to the proto- and meta-xylem cells, for a range of parameter values. A) parameters as in Muraro et. al. 2014, B) as A) with lower CK degradation, C) as B) with lower CK production, D) parameters as in El Showk et. al. 2015, E) as D) with higher CK production. Only C) and E) are able to pattern the tissue correctly. Colour ranges show arbitrary nondimensional values. F-G) Two-parameter plots for CK production and degradation showing the region of parameter space for which robust patterning is maintained. F) CK permeability as in the Minimal Framework model with production restricted to the xylem axis, G) CK production homogeneous throughout tissue.

CHAPTER 6

General Discussion

The task of evaluating the model output based on observed experimental data is not straightforward, especially when it comes to spatial models. For non-spatial models the relevant data is often single quantities that represent the concentration of a molecule in a single cell. In contrast in non-spatial models the data is often comprised of gene expression domain spanning many cells. This requires application of methods that quantify these spatial domains in biologically meaningful manner. Furthermore, due to simplifications and abstractions applied to model interactions and spatial framework, a one-to-one comparison between model output and biological observation is not valid in most cases, i.e. the model is only expected to qualitatively reproduce the experimental data. This is especially relevant when dealing with models simulation with stochastic components where model outputs cannot be compared against a single fixed reference observations. This is because stochastic simulations can result in a range of outputs that differ from each other but are equally valid. Even when a model is deterministic, in many cases, a one-to-one (e.g. pixel-wise) comparison of model output against an experimental observation is too restrictive. This is due inherent variability of biological observations, which complicates their representation by a single reference instance. In general, a simple averaging of many observations is often not the appropriate answer. These problems are perfectly demonstrated when considering a system with oscillating spatial output. System output can appear very different due to their phase difference. A simple averaging of many outputs of such a system would produce a homogeneous outcome, which is far from an adequate representation of the system output. The model evaluation procedure outlined in this thesis is aimed at addressing that problem. The approach concentrated on identifying essential features of the experimental observation that define and distinguish the observation. In our example of an oscillating system, frequency and amplitude of the output correspond to such essential features.Identifying such features requires a careful study and evaluation of the experimental data, since defining a feature as essential is only meaningful when considering the biological context. The model evaluation procedure applied in chapters three and four is by no means complete, it is only a first step towards establishing a framework for assessing simulation output of spatial models against

biological data. In particular, the criteria for choosing quantifiable measures to match against experimental data is not well-defined and can benefit from further investigation.

In **chapter three** I set out to identify the genetic components involved in SAM patterning that correspond to a Turing RD system. We started with a through inspection of the available experimental data related to SAM patterning, spanning several species and developmental stages. We identified specific genes and genetic interaction that constitute likely candidates for a Turing RD system. Wherever this was not possible due to lack of available data, we made minimal assumptions that closely followed the available data. By putting these components together we constructed a computational model, comprised of three motifs: two gradient motif and a Turing RD motif. We demonstrated that interaction between these motifs can account for several observation regarding SAM patterning. Using a network analysis approach we assessed the impact of each of these motifs on model output. The results demonstrated that elements of a RD system can exist embedded within a signaling network, where a whole subnetwork, with multiple elements, is equivalant a single interaction. In addition, in contrast to classical RD systems, in our work, the initial conditions do not include a homogeneous (albeit noisy) distribution of the chemical species. The gradient motifs of the model, L1 signal and CK form gradients that interact with a core RD system. The work clearly demonstrates to what extent the abstract realization of such systems can differ from their biological counterpart. This might at least partially explain how, despite their demonstrated predictive power, reaction-diffusion systems have not passed the burden of biological proof. While, successful in reproducing many biologically observed patterns [170–172], for the most part, experimental identification of RD systems has been challenging.

Our results suggest that identification of biological counterparts of reaction diffusion systems, requires detailed investigation of existing data and examining the capabilities of various networks/subnetworks in functioning as constituent parts of RD systems. The concept of reaction-diffusion systems is concerned with systems that, without diffusion, are at a homogeneous steady-state, and obtain a non-homogeneous 'patterned' steady-state when diffusion is added.

The analytical methods developed for the study of reaction-diffusion systems use such a criteria for defining pattering and non-patterning networks and parameter regimes. The work presented here and others [173, 174], suggests that the development of mathematical methods to analyze RD patterns that do not arise from an initially homogeneous state can be a next step in studying RD systems. Finally we performed and proposed experiments to test the model assumptions and predicted specific properties for the hypothetical model components such as their spatial distribution and their upstream signaling components. Taken together this project was successful in bringing experimental and theoretical research of SAM patterning closer together and providing directions for future experimental efforts.

In the work presented in **chapter four**, the biological context and the developmental time-frame of interest under study made it possible to address the question via a two-dimensional representation of a cross-section of the embryo. The results, demonstrated the importance of auxin transport and patterning in the development of vasculature. In the model, the apical-basal pattern of auxin is not explicitly modeled and is considered as an input (the higher auxin levels of two of the vascular founder cells). We demonstrate that this apical-basal input of auxin is an essential factor in establishing bilateral symmetry in lower vascular tissue. The apical-basal auxin and PIN patterns during vascular development appear to be consistent with the flux-based models. While, as demonstrated in this thesis, the lateral patterns matches the concentration based models. Naturally the next challenge would be to investigate auxin patterning in whole embryo, using three dimensional modeling platforms. A dual model of PAT has shown the capability of reproducing experimental observations [53]. It would be interesting to see whether such a model would be able to account for the early embryonic patterns of auxin distribution, which shows features of both peak formation and canalization. We demonstrated that auxin and CK can regulate vascular development via controlling the growth and geometry of the vascular cells, thus controlling the position of shortest wall that divides those cells. Recently it has been established that auxin is capable of overwriting the shortest wall rule for cell division and result

in asymmetrical cell divisions [122]. An important finding of the work presented in **chapter four** is that the position of connected vascular founder cells in relation to the cotyledons is determined prior to initiation of vasculature. In fact such asymmetry can be traced back to first periclinal division of the embryo; The cell division cell division plane forms with a consistent angle with respect to the axis of the ovule, suggesting that the bilateral symmetry of the plant embryo is established with the first periclinal division. Investigating how the very first cell divisions in embryo are regulated would provide clues into how the bilateral symmetry of the embryo is initially established.

This modeling effort benefited greatly from utilizing the VirtualLeaf modeling platform. By employing this well-developed tool for model simulation and analysis I could focus my efforts solely on model development. Several spatial patterning models are included in VirtualLeaf, including an auxin-PIN up the gradient model, which greatly facilitated the investigation of the role of auxin in the context of the project. Furthermore model description and subsequent communications with other researchers was greatly facilitated thanks to the previously published detailed description of VirtualLeaf and the familiarity of many researchers in the field with this software. This project clearly demonstrate the advantages of a utilizing such platforms to focus and facilitate computational modeling of development in a given field. Ultimately such an approach holds the potential to improve interactions and exchange between researcher active in plant and animal fields.

Chapter five was a result of a collaboration between three research groups involved in computational modeling of vasculature formation. Each group had independently developed a computational model concerning the role of CK and auxin in development and regulation of vasculature in Arabidopsis. These models arrived at different conclusions regarding the genes/hormone regulatory networks involved. Since these models focused on different research questions and employed distinctive modeling approaches, comparison of their conclusions and methodology was not straight forward. The collaboration aimed to determine the fundamental differences in of these models, and to identify assumptions and prediction common between

them. The results showed, in two of these models, while the effect of CK on PIN levels was modeled differently, the overall effect of this interaction was essentially the same. This was confirmed by showing that CK interactions on PIN as specified by one model, result in correct patterning in another model. Thus we could conclude, despite the seemingly conflicting implementation in these models, The CK effect on auxin distribution via regulation of PINs plays a central role in vascular development. The collaboration also pointed out that some important differences in output of these models were due to divergent assumptions regarding CK diffusion rate, thus highlighting the critical experimental data that could lead to further clarification of the role of Ck in shaping plant vasculature.

When it comes to studying processes that give rise to plant organs and tissues, the application of mathematical modeling is inevitable. As demonstrated in this thesis, even in the simplest of settings, such problems are complex and non-intuitive. They fundamentally differ from approaches that deal with intracellular phenomena; mechanical properties of cells, diffusion of chemicals from cell to cell are among aspects that greatly increase the complexity of models. Moreover unlike non-spatial models, outputs are often not numbers corresponding to concentrations; measures that are quantitative and more readily comparable with experimental data. Model output is often in the form of 'expression domains'; patterns that are rather qualitative.

Spatial models of development often deal with pattern formation. When dealing with such a model a critical question is: has the model shown the emergence of a pattern from interactions of its components? do the model assumptions and settings constitute a pattern that is essentially same as the model output. It can be argued that the latter type of models do not demonstrate any system-level behavior but are rather an propagation and maintenance of already existing patterns. The models presented in this thesis are a mixture of both scenarios. They incorporate preexisting patterns, however they demonstrate emergence of patterns that are fundamentally different from the input patterns. Particular attention has been paid to clarify this distinction in the description of the models. This is carried out by clearly stating model assumptions,

model initial conditions and boundary conditions etc. This enable a clear assessment of the contribution of a model to the existing knowledge. This was in part motivated by the observation that often such clarity is lacking in published mathematical models of plant development; model assumptions are not clearly stated and must be inferred indirectly by scrutinizing the details of simulations and model description. This can greatly hinder the understanding and reproduction of such published models which in turn negatively impacts progress in the field. I believe the field of mathematical modeling in plant development can greatly benefit from clarity when it comes to mathematical and computational descriptions of models and the models presented in this thesis are a testament to this.

APPENDICIES

A Chapter three appendix

A.1 Model parameters

Table S1 lists the non-dimensionalized parameters used in simulations presented in the main text unless otherwise stated.

Table S1: The Parameters used in the main text simulations. All parameters are dimensionless.

Parameter	Value	Description
k_1	4	Type-B ARR production
k_2	1	Inverse half maxima for AHK4 activation
k_3	0.8	Inverse half maxima for AHP phosphorylation
k_4	0.1	Rescaled inverse K_d for AHP binding to type-A ARR
k_5	0.1	Rescaled inverse K_d for AHP binding to type-B ARR
k_6	1.5	Strength of the phosphorelay inhibition by X
k_7	1.5	Type-B ARR degradation
k_8	10	Type-A ARR production
k_9	0.01	Strength of the type-A ARR inhibition by WUS
k_{10}	1.4	Type-A ARR degradation
k_{11}	6	AHK4 production
k_{12}	0.1	Inverse half maxima for AHK4 production
k_{13}	3	AHK4 degradation
k_{14}	15	X production
k_{15}	10	X degradation
k_{16}	0.2	WUS production
k_{17}	0.2	Strength of the WUS inhibition by CLV3 peptide
k_{18}	10	CLV3 mRNA production
k_{19}	1	Inverse half maxima for CLV3 mRNA production
k_{20}	20	CLV3 mRNA degradation
k_{21}	12	CLV3 peptide production
k_{22}	2	CLV3 peptide degradation
d_1	300	X diffusion
d_2	2	WUS diffusion
d_3	200	CLV3 peptide diffusion

A.2 Plant material and shoot meristem culture

Plants and cultured apices were grown under the long photoperiod (16 h light). The following lines of *Arabidopsis* have been described previously: Arabidopsis TCS-GFP containing an

enhanced version of the published construct [175] and WUS-GFP [176] are in the Col-0 background. CLV3-GFP (Yadav et al. 2009) is in the Landsberg erecta (Ler) background.For in vitro *Arabidopsis* shoot meristem culture, inflorescence meristems of *Arabidopsis* plants were dissected and transferred to MS medium containing 0.7% phytagel. For Ck treatment, benzyladenine (Sigma-Aldrich) was added to the medium at final concentration of 500M.

In laser ablation experiments 7/9, A total of 6 WUS-GFP seedling were ablated and all subsequently recovered. Out of the 9 TCS-GFP seedling that were ablated and subsequently placed in BA medium 7 recovered. All of 5 CLV3-GFP seedling that were ablated subsequently recovered. In microsurgical experiments 2/2, 2/2 and 3/3 recovered for TCS-GFP, WUS-GFP and CLV3-GFP respectively.

A.3 Microscopy and laser ablation

Confocal analysis was carried out using a Leica upright confocal laser-scanning microscope (Leica TCS SP5) with long-working distance water immersion objectives. The cell wall was stained with 0.2% propidium iodide (PI; Sigma-Aldrich) for 1min. Apices were observed in the 3% agarose medium. Following laser settings are used for the observation; GFP (Argon laser, excitation 488nm, emission, 500-530nm), PI-staining (Argon laser, excitation 488nm, emission 600-700nm). Poking was carried out by fine tungsten needles (World Precision Instruments). Laser ablation was carried out by diode laser at the wavelength of 405 nm. Target cells were chosen using the Leica bleach point function and submitted to UV laser irradiation (90% laser power for 25 seconds). Confocal z-stacks were 3D reconstructed by MorphographX software [177].

B Chapter four appendix

B.1 Plant material and cloning

All seeds were surface-sterilized, sown on solid MS plates, and vernalized for 2 days before growing at a constant temperature of 22°C in a growth room. The log mutants [132] and TMO5/LHW misexpression constructs were genotyped using the primers listed in table B4. All cloning was performed using the LIC cloning system [178] and the vectors described therein. For transcriptional fusions of the LOG genes, 3-kb fragments upstream of the ATG were PCR-amplified from genomic DNA using Q5 polymerase (NEB). To generate pRPS5A-driven misexpression, the coding sequences of all genes were amplified from complementary DNA (cDNA) clones. All constructs were completely sequenced.

B.2 Microscopic analysis

Differential interference contrast, fluorescence, and confocal microscopy were performed as described previously [179]. For histological sections, roots were fixed overnight and embedded as described previously [180]. 3D imaging of embryos was performed according to [181]. Confocal image stacks were reconstructed, and segmentation was performed in MorphoGraphX software [177]. Confocal imaging was performed on a Leica SP5-II system (HyD detector).

B.3 CK measurements

CK quantification by ultrahigh performance liquid chromatography–electrospray tandem mass spectrometry (LC-MS/MS) was performed according to the method described previously [182]. Briefly, 25 to 60 mg fresh weight of 4-day-old Arabidopsis seedling roots were collected and extracted in ice-cold modified Bieleski buffer (methanol/water/formic acid, 15:4:1, v/v/v)

[183]. To each extract, stable isotope-labeled CK internal standards (0.5 pmol of CK bases, ribosides, N-glucosides and 1 pmol of O-glucosides, nucleotides) were added to validate the quantification. For the purification of free CKs, two solid-phase extraction columns were used: the octadecylsilica-based column (500 mg of C18 sorbent, Applied Separations) and the MCX column (30 mg of mixed-mode sorbent, Waters) [184]. Analytes were eluted by two-step elution using a 0.35 M NH4OH aqueous solution and 0.35 M NH4OH in 60% (v/v) methanol solution. Samples were then evaporated under vacuum at 37°C to dryness in vacuo. Purified samples were analyzed by the LC-MS/MS system consisting of an ACQUITY UPLC System (Waters) and a Xevo TQ (Waters) triple quadrupole mass spectrometer. Quantification was obtained using the multiple reaction monitoring mode of selected precursor ions and the appropriate product ions. For each mutant line, four independent biological replicates were analyzed. See Table B3

B.4 ChIP and qRT-PCR analysis

ChIP was performed as previously described [185]. Six hundred milligrams of 5-day-old pTMO5-TMO5-3GFP or pLHW-LHW-sYFP seedlings grown in long-day conditions were used. Anti-GFP antibody (5 μl per sample) (cat. no. 632592, Clontech) was used. Real-time PCR was performed using Power SYBR Green PCR Master Mix (Applied Biosystems). TMO5 and LHW occupancy on genomic DNA was calculated by computing the enrichment over the respective input and normalized over wild type. The primers used for ChIP-qPCR are listed in table B4. Other qRT-PCR analyses were performed as described previously [186]. RNA was extracted with the RNeasy kit (Qiagen). Poly(dT) cDNA was prepared from 1 μg of total RNA with an iScript cDNA Synthesis Kit (Bio-Rad) and analyzed on a CFX384 real−time PCR detection system (Bio−Rad) with iQ SYBR Green Supermix (Bio−Rad) according to the manufacturer's instructions. Primer pairs were designed with Beacon Designer 8.0 (Premier Biosoft International). All individual reactions were done in triplicate with two or three

biological replicates. Data were analyzed with qBase [187]. Expression levels were normalized to those of EEF1α4, CDKA1;1, and ACTIN2. The primer sequences are listed in table B4.

B.5 Combinatorial transcriptome profiling, cell sorting experiments, and data analysis

To identify targets of the TMO5/LHW dimer, transcriptional changes were analyzed after a brief (1 hour) induction of ubiquitously expressed TMO5-GR protein (pRPS5A::TMO5-GR) [125] by dexamethasone in root tips (Fig. B1). This induction was also performed in the presence of the protein synthesis inhibitor cycloheximide to exclude activation of indirect target genes. Because ectopic TMO5 expression can induce PD outside of the vascular domain, in an independent approach, TMO5-GR was ectopically induced in the ground tissue cells, where LHW is already present, thus allowing ectopic TMO5/LHW dimers to form. To enrich for TMO5-GR-expressing cells, we analyzed transcriptional changes in GFP-positive ground tissue cells after dexamethasone treatment in J0571»TMO5::GR/GFP root tips [125] (Fig. B1). These cells were sorted by fluorescence-activated cell sorting using fluorescence of the J0571 GAL4 enhancer trap line. Protoplasting and cell sorting was done as reported previously [188]. Total RNA (100 ng) was labeled using an Ambion WT Expression Kit (Life Technologies) and hybridized to Arabidopsis Gene 1.0 ST arrays (Affymetrix), which probes the expression of 27,827 unique genes. Sample labeling, hybridization to chips, and image scanning were performed according to the manufacturer's instructions. Microarray analysis was performed using MADMAX pipeline for statistical analysis of microarray data [189]. Expression values were calculated using the robust multichip average (RMA) method, which includes quantile normalization [190, 191]. Probe sets on the array were redefined using current genome information [192]. Here, probes were reorganized on the basis of the gene definitions as available in the TAIR10 database. Differentially expressed probe sets (genes) were identified

by linear models and an intensity-based moderated t statistic, taking into account the paired design [193]. P values were corrected for multiple testing by a false discovery rate method [144], and probe sets that satisfied the criterion of $P < 0.05$ were considered to be significantly regulated. Combining these three experiments yielded a small set of 143 genes that were significantly up-regulated (>1.5-fold; $P < 0.05$) in at least one experiment (see table B2). The transcriptomics data files are submitted to Gene Expression Omnibus (GEO) (accession no. GSE56868).

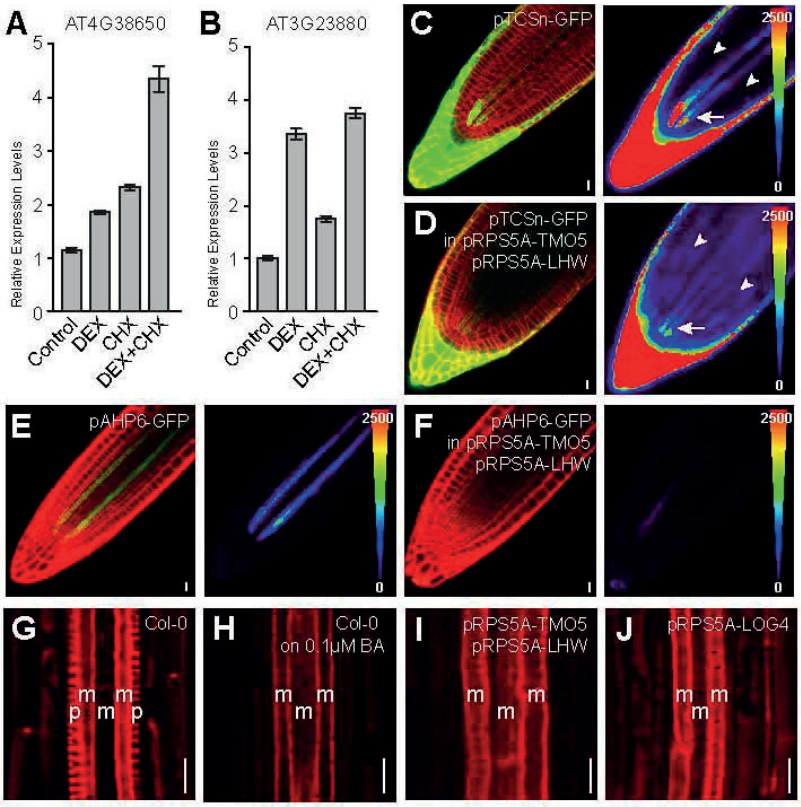

Figure B1: Array validation and CK-related defects in TMO5/LHW-OX lines. (A-B) Relative expression levels of AT4G38650 (A) and AT3g23880 (B) in TMO5-GR root tips upon 1h dexamethasone (DEX), cycloheximide (CHX) or DEX+CHX treatments compared to a control treatment (qRT-PCR confirmation of micro-array). (C-F) Expression of the pTCSn-GFP and pAHP6-GFP reporters in WT and TMO5/LHW- OX root tips. Right images show false color scales of the left image. (G-J) Basic fuchsin stained roots of wild type (Col-0), wild type treated with 0.1 μM BA, TMO5/LHW-OX and LOG4 misexpression (m: metaxylem, p: protoxylem). Error bars in A-B indicate standard error. Scale bars are 10 μm. Images in C-F are counterstained with FM4-64.

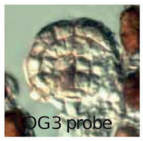

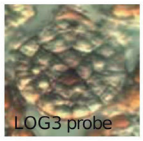

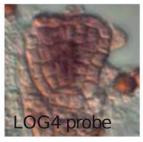


```
LOG3_probe      GTTTGTTTGACACTCGTAAAACTGTCTTAAGAAATTAGATTCTTGTGCTCAAAGAAACCT 60
LOG4_probe      ------------------------------------------------------------

LOG3_probe      TAAACTGCTTACCTTTTCTCTTTCCGCCCAAAATTTAGAATCACATGGAAATCAAAGGTG 120
LOG4_probe      ------------------------------------------ATGGAGGTCAACAATG 16
                                                           *****  ****   **

LOG3_probe      AATCGATGCAAAAGTCAAAGTTCAGAAGAATCTGTGTCTTCTGTGGAAGCAGCCAAGGCA 180
LOG4_probe      AAACCATGCAAAAGTCAAAGTTTGGAAGAATCTGTGTGTTTTGTGGAAGCAGCCAAGGCA 76
                ** * ******************  ************* ** ********************

LOG3_probe      AGAAGAGCAGTTACCAAGATGCTGCTGTTGACCTCGGCAACGAACTGGTTTCAAGGAATA 240
LOG4_probe      AGAAGAGTAGTTACCAAGATGCTGCTGTGGATCTAGGCAACGAATTGGTTTTAAGGAACA 136
                ******* ********************** ** ** ********* ****** ****** *

LOG3_probe      TTGATCTAGTCTATGGAGGTGGGAGCATAGGATTGATGGGTTTGGTTTCACAAGCTGTTC 300
LOG4_probe      TTGATCTAGTCTATGGAGGTGGAAGCATAGGTTTGATGGGTTTGGTTTCGCAAGCTGTTC 196
                ********************** ******** ********************* **********

LOG3_probe      ATGATGGTGGTCGTCATGTTATTGGAATCATTCCCAAGACCCTCATGCCTAGAGAGTTGA 360
LOG4_probe      ATGATGGTGGTCGCCATGTTATTGGAGTTATTCCCAAGACACTCATGCCTAGAGAGTTGA 256
                ************* ************ * *********** ********************

LOG3_probe      CTGGTGAAACAGTAGGAGAAGTAAGAGCAGTTGCAGATATGCACCAAAGGAAAGCTGAGA 420
LOG4_probe      CCGGTGAAACAGTAGGAGAAGTAAGAGCAGTTGCAGATATGCATCAAAGAAAAGCAGAGA 316
                * ****************************************** ***** ***** ****

LOG3_probe      TGGCTAAGCACTCTGATGCTTTTATTGCCTTACCAGGTGGTTATGGAACACTTGAAGAAT 480
LOG4_probe      TGGCTAGACACTCTGATGCTTTTATTGCTTTACCAGGTGGATATGGAACACTTGAAGAGC 376
                ******  ******************** *********** *****************

LOG3_probe      TGCTTGAAGTCATAACTTGGGCTCAGCTTGGTATACATGACAAGCCGGTGGGTTTGCTCA 540
LOG4_probe      TTTTGGAGGTCATAACATGGGCTCAGCTTGGAATACATGATAAACCGGTGGGTTTGCTCA 436
                *  * ** ******** ************** ******** ** *****************

LOG3_probe      ATGTTGATGGATACTACAACTCTCTGCTCTCATTCATTGACAAAGCAGTCGAAGAAGGAT 600
LOG4_probe      ATGTTGATGGATACTACAACTCTTTGCTCTCTTTCATTGATAAAGCCGTTGAAGAAGGCT 496
                ********************** ******* ******** ***** ** ******** *

LOG3_probe      TTATTAGCCCGACTGCTCGTGAGATCATCGTCTCCGCACCTACTGCTAAAGAGCTGGTGA 660
LOG4_probe      TCATCAGTACAAACGCACGCCAGATCATAATTTCTGCACCTACTGCCAAGGAGCTTGTAA 556
                * ** **  * *  ** **  *******  * ** ********** ** ***** ** *

LOG3_probe      AAAAGCTAGAGGAATATGCACCTTGCCATGAAAGGGTTGCAACGAAGCTTTGTTGGGAGA 720
LOG4_probe      AGAAGCTGGAGGAATATTCGCCTTGCCATGAAAGTGTTGCGACTAAGCTTTGTTGGGAGA 616
                * ***** ********* * *************** ***** ** ****************

LOG3_probe      TGGAACGGATTGGTTACTCCTCTGAAGAGTGATTCAGATCAAGATTATCTATATAACTAT 780
LOG4_probe      TAGAGCGGATTGACTACTCTTCTGAAGACTGA---------------------------- 648
                * ** *******  ***** ******** ***

LOG3_probe      TTAAAATATTTTATAATATAGATTTGAAACTTTCGGAGATTTCATGATTTAATCTTACTA 840
LOG4_probe      ------------------------------------------------------------

LOG3_probe      AAAAAGGAAGGGATAGATTTTGATTAGTTGGGTAAAATTTCCACTTCGGAGGAGATTTTT 900
LOG4_probe      ------------------------------------------------------------

LOG3_probe      AATGTAAATTATTAGTAATGTCTTTTTAAGTCGAAGCTAAATGTTTTTAGTTTATGTAAT 960
LOG4_probe      ------------------------------------------------------------

LOG3_probe      TGTCGCAAC 969
LOG4_probe      ---------
```

Figure B2: *In situ* hybridization of *LOG3/4*. ((Left) DIC images of globular and transition stage embryos hybridized with anti-sense *LOG3* or *LOG4* probes. *LOG3* shows highly specific expression in the provascular initial cells (as seen with the p*LOG3-n3GFP* reporter line), while *LOG4* expression is less focused but enriched in vascular cells. (Right) ClustalW multiple sequence alignment of *LOG4* and its closest homolog *LOG3*. Note that *LOG4* is almost identical to *LOG3*, but *LOG3* has predicted 3' and 5'UTR regions that were included in the probe.

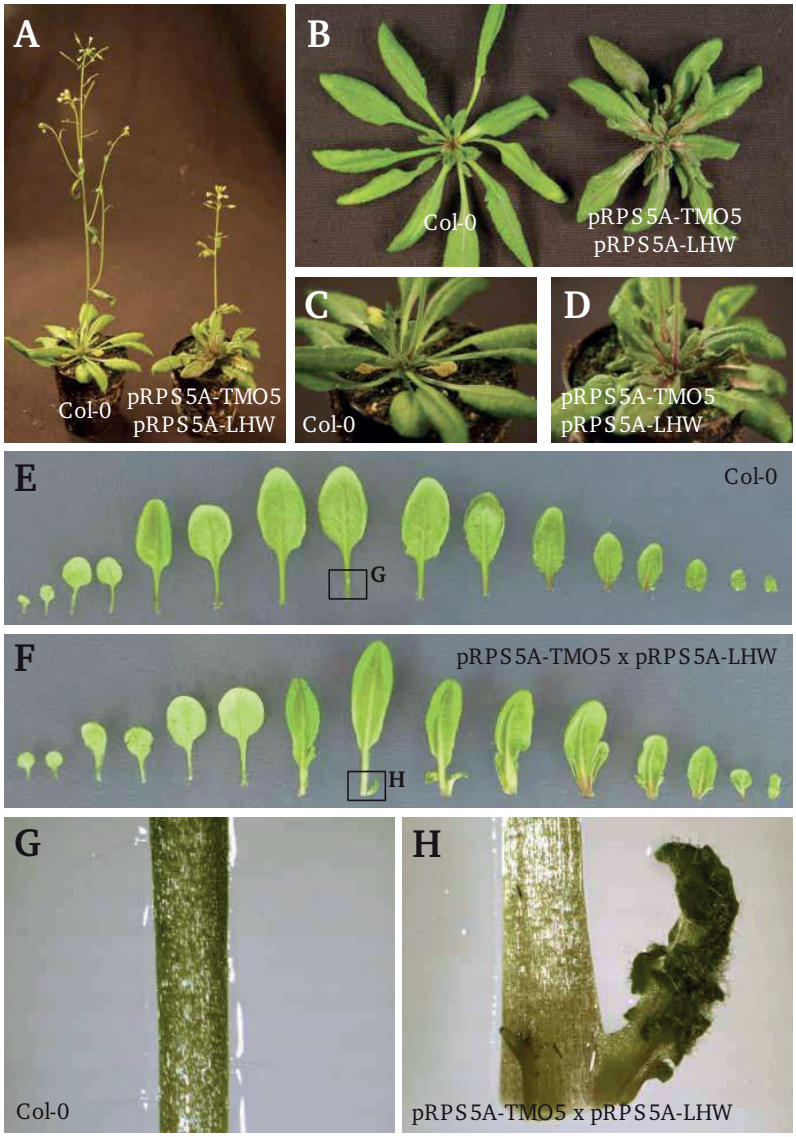

Figure B3: Shoot and leaf phenotypes of TMO5/LHW misexpression. (A-D) Shoot and rosette phenotype of TMO5/LHW-OX compared to wild type (Col-0). (E-H) Leaf series (E-F) and close-up (G-H) of the base of the petiole of TMO5/LHW-OX compared to wild type (Col-0).

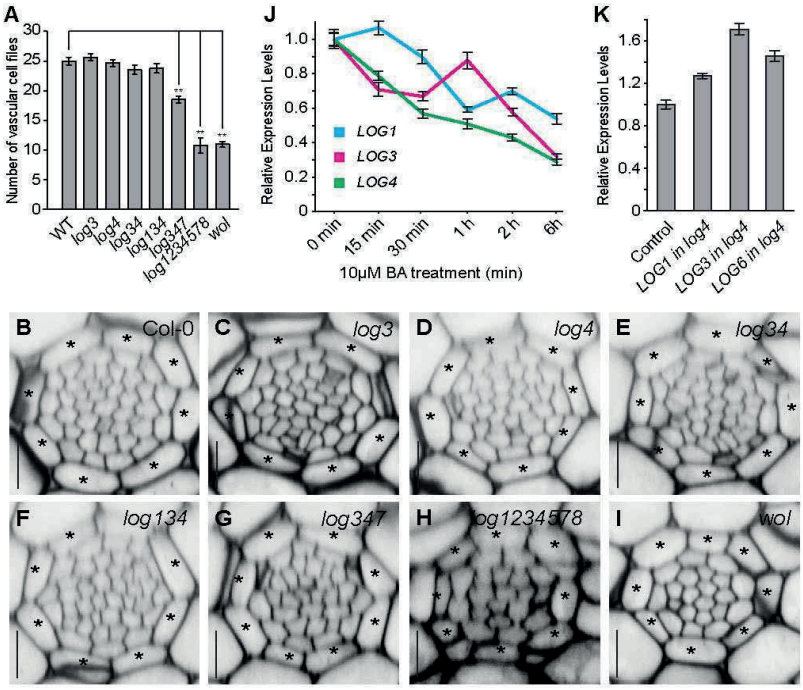

Figure B4: *log* mutant vascular phenotypes and transcriptional *LOG* regulation. (A) Quantification of vascular cell file number in root meristems of *log* single and multiple mutants and *wol* mutant compared to wilt type (WT) (**: p-value < 0.01 as determined by two-sided student t-test). (B-I) Cross sections of vascular tissue in five- day-old root meristems of *log* single and multiple mutants and *wol* mutant compared to wilt type (Col-0). Asterisks indicate endodermis. (J) Relative expression levels of *LOG1*, *LOG3* and *LOG4* after 10 μM benzyl adenine (BA) treatment for the indicated time. (K) Relative expression levels of *LOG1*, *LOG3* and *LOG6* in *log4* mutant roots. Error bars in A, J, K indicate standard error. Scale bars in B-I are 10 μm.

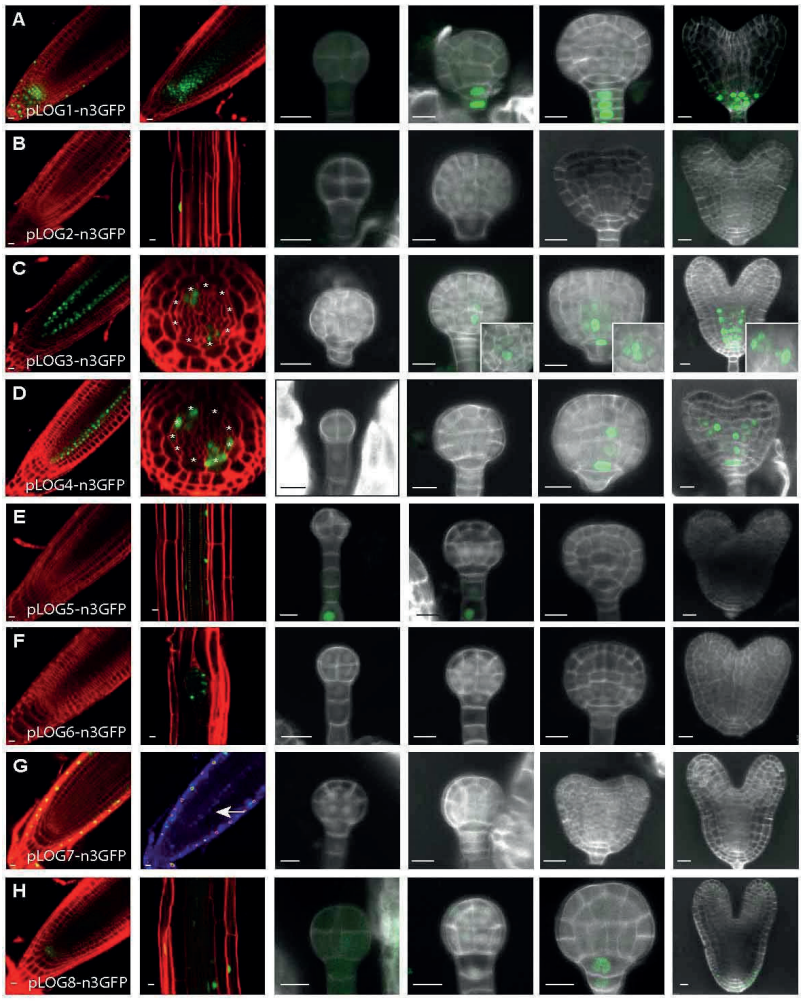

Figure B5: Expression of the LOG family in embryo and root. (A-H) Expression pattern in post-embryonic roots and during embryogenesis of p*LOGx*-n3GFP reporters for *LOG1* (A), *LOG2* (B), *LOG3* (C), *LOG4* (D), *LOG5* (E), *LOG6* (F), *LOG7* (G) and *LOG8* (H). Note that only *LOG3* and *LOG4* show vascular expression during embryogenesis and *LOG7* shows vascular expression in the post-embryonic root (see arrow). *LOG1* had a variable expression pattern. Scale bars are 10 μm.

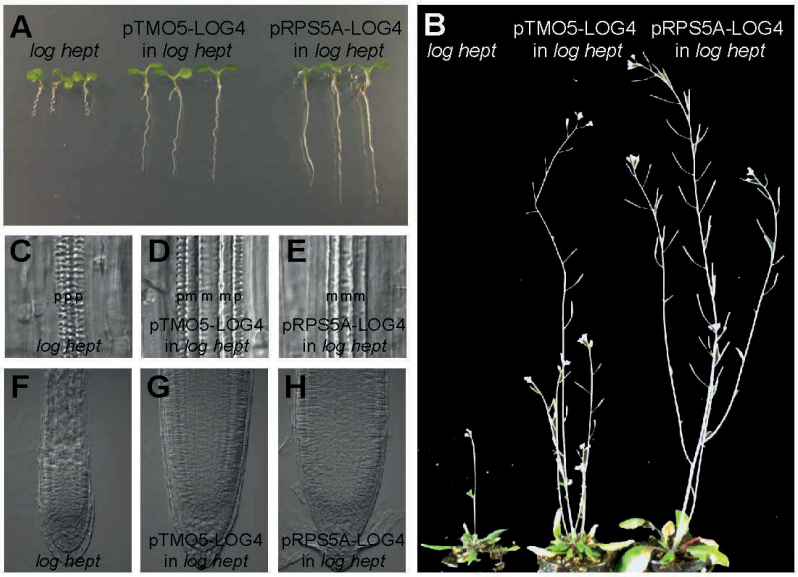

Figure B6: Complementation of the log 1324578 (hept.) mutant. (A-B) Seedling and shoot phenotypes of the *log hept*. mutant and *log hept*.complemented with pTMO5-LOG4 or pRPS5A-LOG4 transgenes. (C-H) Mature root vascular (C-E) and root meristem (F-H) phenotypes of the *log hept*. mutant and *log hept*. complemented with pTMO5-LOG4 or pRPS5A-LOG4 transgenes (m: metaxylem, p: protoxylem).

DEX	DEX+CHX	FACS	FACS vs DEX+CHX	FACS vs DEX	DEX vs DEX+CHX	FACS vs DEX vs DEX+CHX
31	**32**	**103**	**7**	**6**	**6**	**3**
22	**22**	**93**	**4**	**3**	**3**	**3**
AT3G53450	AT3G53450	AT3G53450	AT3G53450	AT3G53450	AT3G53450	AT3G53450
AT4G38650	AT4G38650	AT4G38650	AT4G38650	AT4G38650	AT4G38650	AT4G38650
AT3G23880	AT3G23880	AT3G23880	AT3G23880	AT3G23880	AT3G23880	AT3G23880
AT1G18400	AT1G07860	AT1G01183	AT1G29951	AT1G01110	AT4G17788	
AT1G20530	AT1G19210	AT1G02000	AT1G29952	AT4G01020	AT5G07010	
AT1G22651	AT1G27870	AT1G03746	AT2G37390	AT1G29950	AT5G39080	
AT2G01023	AT1G29951	AT1G08430	AT3G04430			
AT2G05185	AT1G35625	AT1G10640				
AT2G19440	AT1G56540	AT1G16390				
AT2G20722	AT1G63340	AT1G16850				
AT2G36307	AT1G29952	AT1G22400				
AT2G39540	AT1G67000	AT1G23090				
AT2G39675	AT2G04070	AT3G02410				
AT2G43870	AT2G37390	AT1G25425				
AT2G45403	AT3G04430	AT1G28160				
AT1G29950	AT3G14620	AT1G04490				
AT1G01110	AT3G28420	AT1G29560				
AT3G21930	AT3G57460	AT3G25710				
AT3G45930	AT3G61400	AT1G65900				
AT3G49630	AT4G12190	AT1G29951				
AT3G55490	AT4G12410	AT1G31670				
AT4G00885	AT4G17788	AT1G33670				
AT4G01020	AT4G32280	AT1G35610				
AT4G03140	AT4G33800	AT1G35820				
AT4G11213	AT4G38560	AT1G36180				
AT4G17788	AT5G03890	AT1G43720	9			
AT4G39180	AT5G07010	AT1G48390				
AT5G07010	AT5G20470	AT1G48670				
AT5G09710	AT5G24540	AT1G54200				
AT5G22700	AT5G39080	AT1G54680				
AT5G39080	AT5G42325	AT1G58380				
	AT5G46520	AT1G60110				
		AT1G60830				
		AT1G29952				
		AT1G68620				
		AT1G80340				
		AT2G05790				
		AT2G11891				
		AT2G17010				
		AT2G17220				
		AT2G19800				
		AT2G20515				
		AT2G21430				
		AT4G38340				
		AT3G17130				
		AT3G56220				
		AT4G35420				
		AT2G31585				
		AT2G36400				
		AT2G37390				
		AT3G60176				

Table B2: Micro-array Data -Overview of significantly up-regulated genes for each treatment and the overlaps (>1.5 fold change, $p<0.05$). DEX: 3-day-old pRPS5A-TMO5-GR seedlings were grown on control medium and transferred to medium containing 10μM DEX for 1h. Root tips were next used for RNA extraction. DEX+CHX: 3-day-old pRPS5A-TMO5-GR seedlings were grown on control medium and transferred to medium containing 10μM DEX and 10μM CHX for 1h. Root tips were next used for RNA extraction. FACS:3-day-old J0571»pUAS-TMO5-GR seedlings were grown on control medium and transferred to medium containing 10μM DEX for 2h. Root tips were next protoplasted before cell sorting and RNA extraction.First row of numbers shows the amount of genes in that column, the second number the amount of unique genes.The raw .CEL data files are submitted to GEO (accession number GSE56868).

		AT2G40610 AT2G40970 AT2G44460 AT2G44940 AT2G46310 AT3G04430 AT3G04420 AT1G29950 AT3G05190 AT2G26440 AT1G01110 AT3G17420 AT2G38110 AT3G22070 AT1G23205 AT5G08370 AT2G28130 AT3G26160 AT3G44320 AT3G45390 AT4G20362 AT5G52450 AT3G56600 AT3G58980 AT3G14540 AT4G01020 AT4G02170 AT4G02555 AT3G20830 AT4G16855 AT2G29330 AT4G20650 AT4G25780 AT4G28870 AT4G29990 AT2G28120 AT4G14690 AT5G05490 AT5G05460 AT3G45650 AT5G07460 AT5G07640 AT3G24450 AT5G09270 AT5G11430 AT5G27200 AT5G37030 AT5G42590 AT5G46050 AT5G47900 AT1G28110 AT5G60760	10			

	sample	FW (mg)	tZ	tZOG	tZR	tZROG	tZ7G	tZ9G	tZR5'MP
1	Col-0_r1	64.2	0.2798	2.4981	0.0832	0.0879	4.0805	0.6888	0.1207
2	Col-0_r2	52.6	0.2408	2.2281	0.1019	0.0477	4.4354	0.7158	0.2287
3	Col-0_r3	54.2	0.2490	2.4050	0.1144	0.0653	4.3664	0.5710	0.1753
4	Col-0_r4	62.4	0.3350	2.5553	0.1715	0.1038	5.5367	0.8944	0.1280
5	tmo5xtmo5like1_r1	22.5	0.2416	3.0071	0.1062	<LOD	4.4400	0.6729	0.0860
6	tmo5xtmo5like1_r2	25.4	0.1829	1.6839	0.0821	<LOD	3.3547	0.4693	0.0480
7	tmo5xtmo5like1_r3	27.9	0.1099	2.0821	0.0837	<LOD	2.9667	0.5043	0.0476
8	tmo5xtmo5like1_r4	17.4	0.2112	3.2672	0.1347	<LOD	5.0632	0.7190	0.0729
9	TMO5/LHW-OE_r1	42.7	0.6500	14.5482	0.5951	0.5536	30.9754	4.7642	0.8948
10	TMO5/LHW-OE_r2	39.2	0.7096	23.4385	0.7842	1.1311	36.1028	4.6385	0.8099
11	TMO5/LHW-OE_r3	61.9	0.9671	15.9174	1.0288	0.8153	41.9129	5.8819	1.0640
12	TMO5/LHW-OE_r4	64.2	0.8502	19.3603	1.1338	0.7181	39.1117	6.2157	1.4249

	sample	FW (mg)	cZ	cZOG	cZR	cZROG	cZ9G	cZR5´MP
1	Col-0_r1	64.2	0.6439	2.2209	0.3699	<LOD	0.4849	0.9466
2	Col-0_r2	52.6	0.5447	2.3660	0.3517	<LOD	0.4190	1.1639
3	Col-0_r3	54.2	0.5223	2.8284	0.3803	<LOD	0.4511	1.2875
4	Col-0_r4	62.4	0.6346	2.3026	0.4704	<LOD	0.5702	1.2123
5	tmo5xtmo5like1_r1	22.5	0.3729	1.7916	0.3644	<LOD	0.4689	0.5511
6	tmo5xtmo5like1_r2	25.4	0.3130	1.6299	0.2579	<LOD	0.3441	0.4858
7	tmo5xtmo5like1_r3	27.9	0.1989	1.2763	0.2436	<LOD	0.2513	0.3186
8	tmo5xtmo5like1_r4	17.4	0.4190	2.2402	0.4278	<LOD	0.4960	0.4333
9	TMO5/LHW-OE_r1	42.7	0.1211	3.0244	0.3253	0.3860	1.1721	0.7728
10	TMO5/LHW-OE_r2	39.2	0.1640	3.2589	0.3176	0.5611	1.1855	0.7566
11	TMO5/LHW-OE_r3	61.9	0.1816	2.1449	0.3743	0.6496	1.0286	0.8701
12	TMO5/LHW-OE_r4	64.2	0.1436	2.8830	0.4413	0.4857	0.8361	0.7104

	sample	FW (mg)	DHZ	DHZOG	DHZR	DHZROG	DHZ7G	DHZ9G	DHZR5'MP
1	Col-0_r1	64.2	<LOD	<LOD	<LOD	<LOD	0.9861	<LOD	<LOD
2	Col-0_r2	52.6	<LOD	<LOD	<LOD	<LOD	1.5456	<LOD	<LOD
3	Col-0_r3	54.2	<LOD	<LOD	<LOD	<LOD	1.4638	<LOD	<LOD
4	Col-0_r4	62.4	<LOD	<LOD	<LOD	<LOD	1.5322	<LOD	<LOD
5	tmo5xtmo5like1_r1	22.5	<LOD	<LOD	<LOD	<LOD	0.9996	<LOD	<LOD
6	tmo5xtmo5like1_r2	25.4	<LOD	<LOD	<LOD	<LOD	0.6783	<LOD	<LOD
7	tmo5xtmo5like1_r3	27.9	<LOD	<LOD	<LOD	<LOD	0.6086	<LOD	<LOD
8	tmo5xtmo5like1_r4	17.4	<LOD	<LOD	<LOD	<LOD	1.0523	<LOD	<LOD
9	TMO5/LHW-OE_r1	42.7	<LOD	0.3670	0.0816	<LOD	8.4347	0.1290	<LOD
10	TMO5/LHW-OE_r2	39.2	0.0199	0.6145	0.0575	<LOD	10.2296	0.1429	<LOD
11	TMO5/LHW-OE_r3	61.9	0.0102	0.3336	0.0661	<LOD	13.1813	0.1968	<LOD
12	TMO5/LHW-OE_r4	64.2	0.0179	0.4885	0.1047	<LOD	13.3498	0.1567	<LOD

	sample	FW (mg)	iP	iPR	iP7G	iP9G	iPR5'MP
1	Col-0_r1	64.2	0.0682	0.1245	20.9759	0.6757	0.4319
2	Col-0_r2	52.6	0.0391	0.1379	19.6523	0.6838	0.6460
3	Col-0_r3	54.2	0.0475	0.1318	20.3362	0.6319	0.7828
4	Col-0_r4	62.4	0.0693	0.1874	25.6654	0.9122	0.6199
5	tmo5xtmo5like1_r1	22.5	0.0314	0.1620	21.6173	1.1249	0.5796
6	tmo5xtmo5like1_r2	25.4	0.0235	0.1644	18.6055	0.8819	0.4720
7	tmo5xtmo5like1_r3	27.9	0.0174	0.1038	14.7889	0.6326	0.6918
8	tmo5xtmo5like1_r4	17.4	0.0320	0.2095	25.4391	1.1201	0.7632
9	TMO5/LHW-OE_r1	42.7	0.1622	0.3547	108.4042	3.4461	3.3536
10	TMO5/LHW-OE_r2	39.2	0.1581	0.6438	113.3747	3.6334	3.5087
11	TMO5/LHW-OE_r3	61.9	0.2006	0.6397	132.9404	3.8048	3.6050
12	TMO5/LHW-OE_r4	64.2	0.1764	0.4767	123.2382	3.8231	5.1112

Table B3: Cytokinin measurements. in 4-day-old root tips of wild type, tmo5 tmo5-like1 double mutant and pRPS5A-TMO5 x pRPS5A-LHW double misexpression lines. Cytokinin content in 1g of extracted 4-day old root tissue (pmol/g).

cloning primers for LIC cloning

primer	for/rev	sequence with LIC adapter
pLOG1	for	TAGTTGGAATGGGTTCGAAgctaaattgccataaaatgaagg
	rev	TTATGGAGTTGGGTTCGAActttctcttcacacaaagttttg
pLOG2	for	TAGTTGGAATGGGTTCGAAcatccacatcccacatcttttaatgg
	rev	TTATGGAGTTGGGTTCGAAtatctctctctctttctgtctttttcc
pLOG3	for	TAGTTGGAATGGGTTCGAAgtgatatcactgccatcgtcatgg
	rev	TTATGGAGTTGGGTTCGAAgtgattctaaattttgggcgg
pLOG4	for	TAGTTGGAATGGGTTCGAAgtctgttcgaatcctgcgagattgg
	rev	TTATGGAGTTGGGTTCGAAtggttacgatgagagctcaagc
pLOG5	for	TAGTTGGAATGGGTTCGAAccattttcctagaaaagaaaagaaag
	rev	TTATGGAGTTGGGTTCGAAtttcttagccaaatcagtttactttc
pLOG6	for	TAGTTGGAATGGGTTCGAAgaaatagtcgctggttacaaatgc
	rev	TTATGGAGTTGGGTTCGAAtgtttcggctaacttgtcaaagtcg
pLOG7	for	TAGTTGGAATGGGTTCGAActctgatcgttggggttttgcaaggg
	rev	TTATGGAGTTGGGTTCGAAatttctctctctttctctttgttactttgtc
pLOG8	for	TAGTTGGAATGGGTTCGAAgtttgcatttttttcccaattacc
	rev	TTATGGAGTTGGGTTCGAAtaatggataaaaatctacaaatc
LOG4-CDS	for	TAGTTGGAATAGGTTCatggaggtcaacaatgaaaccatgc
	rev	AGTATGGAGTTGGGTTCtcagtcttcagaagagtagtcaatcc

genotyping primers

primer	for/rev	sequence
log3-1	for	CATTCCCAAGACCCTCATGCCTAGA
	rev	CTAATTTTAAGTGCCAGATGTTGAT
log4-3	for	GGTTTGCTTTGTAATGATTTCTGGG
	rev	TCAGTCTTCAGAAGAGTAGTCAATC
log7-1	for	GTCATTACATGGGCTCAACTCGGTA
	rev	TCACAATCAGGGGTTATGTAGTCGT

Q-PCR primers

primer	for/rev	sequence
CDKA	for	ATTGCGTATTGCCACTCTCATAGG
	rev	TCCTGACAGGGATACCGAATGC
EEF	for	CTGGAGGTTTTGAGGCTGGTAT
	rev	CCAAGGGTGAAAGCAAGAAGA
ACT2	for	CTCCATTTGTTTGTTTCATT
	rev	TCAATTCGATCACTCAGA
TMO5	for	CGATAGAAGAAGCGTTAA
	rev	CGATTCACCATCTTACTA
LOG1	for	TCCCACTTGTGAAATCTCA

Table B4: Primer List. Overview of the primers used for cloning, genotyping, Q-RT-PCR and in situ hybridization (p: promoter). All primer sequences are from 5' to 3'.

	rev	CGGTTTGCTTGGACTAAG
LOG3	for	GGAAGGGATAGATTTTGATTAGTT
	rev	GAGAGTTGCGACAATTACATAA
LOG4	for	GGTTTGATGGGTTTGGTTTCGC
	rev	CTACTGTTTCACCGGTCAACTCTC
LOG6	for	GGTGATGAGGAAGATTGA
	rev	GAGACATTGACAGAGTGA
AT4G38650	for	AAGTTAAGGCGACGACAG
	rev	ATGATGCCAACTCTATACTCTC
AT3G23880	for	TACATCAACGGGACACTA
	rev	AAGCTCCTTGAACTCATC

***in situ* hybridisation probes**

primer	for/rev	sequence
LOG3	for	aaaaaGAATTCGTTTGTTTGACACTCGTAAAAC
	rev	aaaaaGGATCCGTTGCGACAATTACATAAAC
LOG4	for	aaaaaGAATTCATGGAGGTCAACAATGAAACC
	rev	aaaaaGGATCCTCAGTCTTCAGAAGAGTAGTC

ChIP-Q-PCR

primer	for/rev	sequence
LOG4-1	for	CGATGGTATCTTCGACGTCAT
	rev	GTCATTGCTATGCCCCATTT
LOG4-2	for	AGAAAGCGAGGAGCCTTTTC
	rev	GTGTGCGCCGAATACAGAT
LOG4-3	for	GCTCATGGAAAACGATGTCA
	rev	GCTTGGAAGCAATGAATTTG
LOG4-4	for	AGGGAATCAAAAAGCGAGGT
	rev	TGTCGTGCGAAAGATAATGG
LOG4-5	for	TCCAAGAGCATGACGAGAAA
	rev	CGAGAGTTGGGGATTGTTGT
TA3	for	CTGCGTGGAAGTCTGTCAAA
	rev	CTATGCCACAGGGCAGTTTT

BIBLIOGRAPHY

Bibliography

[1] Wendell A Lim, Connie M Lee, and Chao Tang. Design principles of regulatory networks: searching for the molecular algorithms of the cell. *Molecular cell*, 49(2):202–212, 2013.

[2] Ewa Paluch and Carl-Philipp Heisenberg. Biology and physics of cell shape changes in development. *Current Biology*, 19(17):R790–R799, 2009.

[3] Alan Mathison Turing. The chemical basis of morphogenesis. *Phil. Trans. R. Soc. B*, 237:37–72, 1952.

[4] Pva Křeček. The pin-formed (pin) protein family of auxin transporters. *Genome biology*, 10(12):249, 2009.

[5] Klaartje van Berkel, Rob J de Boer, Ben Scheres, and Kirsten ten Tusscher. Polar auxin transport: models and mechanisms. *Development*, 140(11):2253–2268, 2013.

[6] GJ Mitchison, DE Hanke, and AR Sheldrake. The polar transport of auxin and vein patterns in plants [and discussion]. *Philosophical Transactions of the Royal Society of London B: Biological Sciences*, 295(1078):461–471, 1981.

[7] GJ Mitchison. A model for vein formation in higher plants. *Proceedings of the Royal Society of London B: Biological Sciences*, 207(1166):79–109, 1980.

[8] Richard Kennaway, Enrico Coen, Amelia Green, and Andrew Bangham. Generation of diverse biological forms through combinatorial interactions between tissue polarity and growth. *PLoS Comput Biol*, 7(6):e1002071, 2011.

[9] Roeland MH Merks, Michael Guravage, Dirk Inzé, and Gerrit TS Beemster. Virtualeaf: an open-source framework for cell-based modeling of plant tissue growth and development. *Plant physiology*, 155(2):656–666, 2011.

[10] Frédéric Boudon, Christophe Pradal, Thomas Cokelaer, Przemyslaw Prusinkiewicz, and Christophe Godin. L-py: an l-system simulation framework for modeling plant architecture development based on a dynamic language. *Frontiers in Plant Science*, 3:76, 2012.

[11] Guy Karlebach and Ron Shamir. Modelling and analysis of gene regulatory networks. *Nature Reviews Molecular Cell Biology*, 9(10):770–780, 2008.

[12] Florian Lienert, Jason J Lohmueller, Abhishek Garg, and Pamela A Silver. Synthetic biology in mammalian cells: next generation research tools and therapeutics. *Nature Reviews Molecular Cell Biology*, 15(2):95–107, 2014.

[13] Ingrid Lobo. Biological complexity and integrative levels of organization. *Nature Education*, 1(1):141, 2008.

[14] Upinder S Bhalla and Ravi Iyengar. Emergent properties of networks of biological signaling pathways. *Science*, 283(5400):381–387, 1999.

[15] David G Green. Emergent behaviour in biological systems. *Complex systems: from biology to computation*, pages 24–35, 1993.

[16] Denis Noble. *The music of life*. Oxford University Pressy, Oxford, UK, 2008.

[17] Jeff Hasty, David McMillen, Farren Isaacs, and James J Collins. Computational studies of gene regulatory networks: in numero molecular biology. *Nature Reviews Genetics*, 2(4):268–279, 2001.

[18] Frank Emmert-Streib and Galina V Glazko. Network biology: a direct approach to study biological function. *Wiley Interdisciplinary Reviews: Systems Biology and Medicine*, 3(4):379–391, 2011.

[19] John Tyler Bonner. *First signals: the evolution of multicellular development*. Princeton University Press, 2009.

[20] Sami Alom Ruiz and Christopher S Chen. Emergence of patterned stem cell differentiation within multicellular structures. *Stem cells*, 26(11):2921–2927, 2008.

[21] Roeland MH Merks and James A Glazier. A cell-centered approach to developmental biology. *Physica A: Statistical Mechanics and its Applications*, 352(1):113–130, 2005.

[22] G Wayne Brodland. How computational models can help unlock biological systems. In *Seminars in cell & developmental biology*, volume 47, pages 62–73. Elsevier, 2015.

[23] Hans Meinhardt. Models of biological pattern formation: common mechanism in plant and animal development. *International Journal of Developmental Biology*, 40(1):123–134, 2003.

[24] Hidde De Jong. Modeling and simulation of genetic regulatory systems: a literature review. *Journal of computational biology*, 9(1):67–103, 2002.

[25] Przemyslaw Prusinkiewicz. Modeling plant growth and development. *Current opinion in plant biology*, 7(1):79–83, 2004.

[26] Ron Milo, Shai Shen-Orr, Shalev Itzkovitz, Nadav Kashtan, Dmitri Chklovskii, and Uri Alon. Network motifs: simple building blocks of complex networks. *Science*, 298(5594):824–827, 2002.

[27] Shmoolik Mangan and Uri Alon. Structure and function of the feed-forward loop network motif. *Proceedings of the National Academy of Sciences*, 100(21):11980–11985, 2003.

[28] Scott Camazine. *Self-organization in biological systems*. Princeton University Press, 2003.

[29] Eric Karsenti. Self-organization in cell biology: a brief history. *Nature Reviews Molecular Cell Biology*, 9(3):255–262, 2008.

[30] Mathias Bode and H-G Purwins. Pattern formation in reaction-diffusion systems-dissipative solitons in physical systems. *Physica D: Nonlinear Phenomena*, 86(1):53–63, 1995.

[31] AJ Koch and Hans Meinhardt. Biological pattern formation: from basic mechanisms to complex structures. *Reviews of Modern Physics*, 66(4):1481, 1994.

[32] Alfred Gierer and Hans Meinhardt. A theory of biological pattern formation. *Kybernetik*, 12(1):30–39, 1972.

[33] J_ D Murray. A pre-pattern formation mechanism for animal coat markings. *Journal of Theoretical Biology*, 88(1):161–199, 1981.

[34] Simona Digiuni, Swen Schellmann, Florian Geier, Bettina Greese, Martina Pesch, Katja Wester, Burcu Dartan, Valerie Mach, Bhylahalli Purushottam Srinivas, Jens Timmer, et al. A competitive complex formation mechanism underlies trichome patterning on arabidopsis leaves. *Molecular Systems Biology*, 4(1):217, 2008.

[35] J Raspopovic, L Marcon, L Russo, and J Sharpe. Digit patterning is controlled by a bmp-sox9-wnt turing network modulated by morphogen gradients. *Science*, 345(6196):566–570, 2014.

[36] Andrew D Economou, Atsushi Ohazama, Thantrira Porntaveetus, Paul T Sharpe, Shigeru Kondo, M Albert Basson, Amel Gritli-Linde, Martyn T Cobourne, and Jeremy BA Green. Periodic stripe formation by a turing mechanism operating at growth zones in the mammalian palate. *Nature genetics*, 44(3):348–351, 2012.

[37] HG Othmer and E Pate. Scale-invariance in reaction-diffusion models of spatial pattern formation. *Proceedings of the National Academy of Sciences*, 77(7):4180–4184, 1980.

[38] Edward Pate and Hans G Othmer. Applications of a model for scale-invariant pattern formation in developing systems. *Differentiation*, 28(1):1–8, 1984.

[39] René Benjamins and Ben Scheres. Auxin: the looping star in plant development. *Annu. Rev. Plant Biol.*, 59:443–465, 2008.

[40] William D Teale, Ivan A Paponov, and Klaus Palme. Auxin in action: signalling, transport and the control of plant growth and development. *Nature Reviews Molecular Cell Biology*, 7(11):847–859, 2006.

[41] Eric M Kramer. Pin and aux/lax proteins: their role in auxin accumulation. *Trends in plant science*, 9(12):578–582, 2004.

[42] Ranjan Swarup and Benjamin Péret. Aux/lax family of auxin influx carriers—an overview. *Frontiers in plant science*, 3, 2012.

[43] Jürgen Kleine-Vehn, Pankaj Dhonukshe, Ranjan Swarup, Malcolm Bennett, and Jiří Friml. Subcellular trafficking of the arabidopsis auxin influx carrier aux1 uses a novel pathway distinct from pin1. *The Plant Cell Online*, 18(11):3171–3181, 2006.

[44] Tomasz Paciorek, Eva Zažímalová, Nadia Ruthardt, Jan Petrášek, York-Dieter Stierhof, Jürgen Kleine-Vehn, David A Morris, Neil Emans, Gerd Jürgens, Niko Geldner, et al. Auxin inhibits endocytosis and promotes its own efflux from cells. *Nature*, 435(7046):1251–1256, 2005.

[45] Anne Vieten, Steffen Vanneste, Justyna Wiśniewska, Eva Benková, René Benjamins, Tom Beeckman, Christian Luschnig, and Jiří Friml. Functional redundancy of pin proteins is accompanied by auxin-dependent cross-regulation of pin expression. *Development*, 132(20):4521–4531, 2005.

[46] Jürgen Kleine-Vehn and Jirí Friml. Polar targeting and endocytic recycling in auxin-dependent plant development. *Annual review of cell and developmental biology*, 24:447–473, 2008.

[47] Teva Vernoux, Fabrice Besnard, and Jan Traas. Auxin at the shoot apical meristem. *Cold Spring Harbor Perspectives in Biology*, 2(4):a001487, 2010.

[48] T Sachs. Polarity and the induction of organized vascular tissues. *Annals of Botany*, 33(2):263–275, 1969.

[49] F Santos, W Teale, C Fleck, M Volpers, B Ruperti, and K Palme. Modelling polar auxin transport in developmental patterning. *Plant Biology*, 12(s1):3–14, 2010.

[50] GJ Mitchison. The dynamics of auxin transport. *Proceedings of the Royal Society of London B: Biological Sciences*, 209(1177):489–511, 1980.

[51] Henrik Jönsson, Marcus G Heisler, Bruce E Shapiro, Elliot M Meyerowitz, and Eric Mjolsness. An auxin-driven polarized transport model for phyllotaxis. *Proceedings of the National Academy of Sciences of the United States of America*, 103(5):1633–1638, 2006.

[52] Richard S Smith, Soazig Guyomarc'h, Therese Mandel, Didier Reinhardt, Cris Kuhlemeier, and Przemyslaw Prusinkiewicz. A plausible model of phyllotaxis. *Proceedings of the National Academy of Sciences of the United States of America*, 103(5):1301–1306, 2006.

[53] Emmanuelle M Bayer, Richard S Smith, Therese Mandel, Naomi Nakayama, Michael Sauer, Przemyslaw Prusinkiewicz, and Cris Kuhlemeier. Integration of transport-based models for phyllotaxis and midvein formation. *Genes & development*, 23(3):373–384, 2009.

[54] Shmoolik Mangan, Alon Zaslaver, and Uri Alon. The coherent feedforward loop serves as a sign-sensitive delay element in transcription networks. *Journal of molecular biology*, 334(2):197–204, 2003.

[55] Shmoolik Mangan, Shalev Itzkovitz, Alon Zaslaver, and Uri Alon. The incoherent feed-forward loop accelerates the response-time of the gal system of escherichia coli. *Journal of molecular biology*, 356(5):1073–1081, 2006.

[56] Lea Goentoro, Oren Shoval, Marc W Kirschner, and Uri Alon. The incoherent feedforward loop can provide fold-change detection in gene regulation. *Molecular cell*, 36(5):894–899, 2009.

[57] Shai Kaplan, Anat Bren, Erez Dekel, and Uri Alon. The incoherent feed-forward loop can generate non-monotonic input functions for genes. *Molecular systems biology*, 4(1):203, 2008.

[58] Ram Kishor Yadav, Thomas Girke, Sumana Pasala, Mingtang Xie, and G Venugopala Reddy. Gene expression map of the arabidopsis shoot apical meristem stem cell niche. *Proceedings of the National Academy of Sciences*, 106(12):4941–4946, 2009.

[59] Matthew R Tucker and Thomas Laux. Connecting the paths in plant stem cell regulation. *Trends in Cell Biol.*, 17:403–10, 2007.

[60] Didier Reinhardt, Martin Frenz, Therese Mandel, and Cris Kuhlemeier. Microsurgical and laser ablation analysis of interactions between the zones and layers of the tomato shoot apical meristem. *Development*, 130:4073–4083, 2003.

[61] RN Stewart and Jen Sheen. Determination of number and mitotic activity of shoot apical initial cells by analysis of mericlinal chimeras. *Am. J. Bot.*, 57:816–826, 1970.

[62] H Schoof, M Lenhard, A Haecker, K F Mayer, G Jürgens, and T Laux. The stem cell population of Arabidopsis shoot meristems in maintained by a regulatory loop between the CLAVATA and WUSCHEL genes. *Cell*, 100:635–44, 2000.

[63] H Jonsson, M Heisler, G. V Reddy, V Agrawal, V Gor, B. E Shapiro, E Mjolsness, and E. M Meyerowitz. Modelling the organisation of the WUSCHEL expression domain in the shoot apical meristem. *Bioinformatics*, 21:i232–i240, 2005.

[64] Tim Hohm, Eckart Zitzler, and Rüdiger Simon. A dynamic model for stem cell homeostasis and patterning in Arabidopsis meristems. *PLoS ONE*, 5(2):e9189, 2010.

[65] Hironori Fujita, Koichi Toyokura, Kiyotaka Okada, and Masayoshi Kawaguchi. Reaction-diffusion pattern in shoot apical meristem of plants. *PloS ONE*, 6(3):e18243, 2011.

[66] Ram Kishor Yadav, Mariano Perales, Jérémy Gruel, Carolyn Ohno, Marcus Heisler, Thomas Girke, Henrik Jönsson, and G Venugopala Reddy. Plant stem cell maintenance involves direct transcriptional repression of differentiation program. *Molecular systems biology*, 9(1), 2013.

[67] Vijay S Chickarmane, Sean P Gordon, Paul T Tarr, Marcus G Heisler, and Elliot M Meyerowitz. Cytokinin signaling as a positional cue for patterning the apical-basal axis of the growing Arabidopsis shoot meristem. *PNAS*, 109:4002–4007, 2012.

[68] Sean P Gordon, Vijay S Chickarmane, Carolyn Ohno, and Elliot M Meyerowitz. Multiple feedback loops through cytokinin signalling control stem cell number within the Arabidopsis shoot meristem. *PNAS*, 106:16529–16534, 2009.

[69] Thomas Berleth and Steve Chatfield. Embryogenesis: pattern formation from a single cell. *The Arabidopsis Book*, 7(1):1–88, 2002.

[70] Bert De Rybel, Ari Pekka Mähönen, Yrjö Helariutta, and Dolf Weijers. Plant vascular development: from early specification to differentiation. *Nature reviews. Molecular cell biology*, 17(1):30, 2016.

[71] Ben Scheres, Harald Wolkenfelt, Viola Willemsen, Maarten Terlouw, Emily Lawson, Caroline Dean, and Peter Weisbeek. Embryonic origin of the arabidopsis primary root and root meristem initials. *Development*, 120(9):2475–2487, 1994.

[72] Bert De Rybel, Milad Adibi, Alice S Breda, Jos R Wendrich, Margot E Smit, Ondřej Novák, Nobutoshi Yamaguchi, Saiko Yoshida, Gert Van Isterdael, Joakim Palovaara,

et al. Integration of growth and patterning during vascular tissue formation in arabidopsis. *Science*, 345(6197):1255215, 2014.

[73] M.K Barton. Twenty years on: The inner workings of the shoot apical meristem, a developmental dynamo. *Dev. Biol.*, 341:95–113, 2010.

[74] Ram Kishor Yadav, Mariano Perales, Jérémy Gruel, Thomas Girke, Henrik Jönsson, and G Venugopala Reddy. Wuschel protein movement mediates stem cell homeostasis in the arabidopsis shoot apex. *Genes & development*, 25(19):2025–2030, 2011.

[75] Michael Lenhard and Thomas Laux. Stem cell homeostasis in the arabidopsis shoot meristem is regulated by intercellular movement of clavata3 and its sequestration by clavata1. *Development*, 130(14):3163–3173, 2003.

[76] Andrea Leibfried, Jennifer P. C To, Wolfgang Busch, Sandra Stehling, Andreas Kehle, Monika Demar, Joseph J Kieber, and Jan U Lohmann. WUSCHEL controls meristem function by direct regulation of cytokinin-inducible response regulators. *Nature*, 438:1172–1175, 2005.

[77] J. P.C To. Type-a arabidopsis response regulators are partially redundant negative regulators of cytokinin signalling. *Plant Cell*, 16:658–671, 2004.

[78] Klaus FX Mayer, Heiko Schoof, Achim Haecker, Michael Lenhard, Gerd Jürgens, and Thomas Laux. Role of WUSCHEL in regulating stem cell fate in the Arabidopsis shoot meristem. *Cell*, 95:805–815, 1998.

[79] Junko Kyozuka. Control of shoot and root meristem function by cytokinin. *Current opinion in plant biology*, 10(5):442–446, 2007.

[80] Raffaele Dello Ioio, Francisco Scaglia Linhares, Emanuele Scacchi, Eva Casamitjana-Martinez, Renze Heidstra, Paolo Costantino, and Sabrina Sabatini. Cytokinins determine arabidopsis root-meristem size by controlling cell differentiation. *Current Biology*, 17(8):678–682, 2007.

[81] Osnat Yanai, Eilon Shani, Karel Dolezal, Petr Tarkowski, Robert Sablowski, Goran Sandberg, Alon Samach, and Naomi Ori. Arabidopsis knoxi proteins activate cytokinin biosynthesis. *Current Biology*, 15(17):1566–1571, 2005.

[82] Annie Jacqmard, Nathalie Detry, Walter Dewitte, Harry Van Onckelen, and Georges Bernier. *In situ* localisation of cytokinins in the shoot apical meristem of *Sinapis alba* at floral transition. *Planta*, 214:970–973, 2002.

[83] Takashi Kurakawa, Nanae Ueda, Masahiko Maekawa, Kaoru Kobayashi, Mikiko Kojima, Yasuo Nagato, Hitoshi Sakakibara, and Junko Kyozuka. Direct control of shoot meristem activity by a cytokinin-activating enzyme. *Nature*, 445:652–655, 2007.

[84] I Hwang and J Sheen. Two component circuitry in Arabidopsis cytokinin signal transduction. *Nature*, 413:383–389, 2001.

[85] J. P.C To, J Deruere, B. B Maxwell, V. F Morris, C. E Hutchison, F. J Ferreira, G. E Schaller, and J. J Kieber. Cytokinin regulates type-A Arabidopsis response regulator activity and protein stability via two-component phosphorelay. *Plant Cell*, 19:3901–3914, 2007.

[86] Jennifer P C To and Joseph J Kieber. Cytokinin signaling: two-components and more. *Trends Plant Sci*, 13:85–92, 2008.

[87] M. G Mason. Multiple type-B response regulators mediate cytokinin signal transduction in Arabidopsis. *Plant cell*, 17:3007–3018, 2005.

[88] Steven Dodsworth. A diverse and intricate signalling network regulates stem cell fate in the shoot apical meristem. *Deve. l Biol.*, 336(1):1–9, 2009.

[89] Jennifer PokChun To. *Arabidopsis Response Regulators in Cytokinin Signaling and Development*. ProQuest, 2007.

[90] Ram Kishor Yadav, Mariano Perales, Jérémy Gruel, Thomas Girke, Henrik Jönsson, and G Venugopala Reddy. WUSCHEL protein movement mediates stem cell homeostasis in the Arabidopsis shoot apex. *Genes and Dev*, 25:2025–2030, 2011.

[91] Steffen Knauer, Anna L Holt, Ignacio Rubio-Somoza, Elise J Tucker, Annika Hinze, Melanie Pisch, Marie Javelle, Marja C Timmermans, Matthew R Tucker, and Thomas Laux. A protodermal mir394 signal defines a region of stem cell competence in the Arabidopsis shoot meristem. *Dev. Cell*, 24:125–132, 2013.

[92] Hans Meinhardt and Alfred Gierer. Pattern formation by local self-activation and lateral inhibition. *Bioessays*, 22(8):753–760, 2000.

[93] Debbie Winter, Ben Vinegar, Hardeep Nahal, Ron Ammar, Greg V Wilson, and Nicholas J Provart. An "electronic fluorescent pictograph" browser for exploring and analyzing large-scale biological data sets. *PloS one*, 2(8):e718, 2007.

[94] Hideki Goda, Eriko Sasaki, Kenji Akiyama, Akiko Maruyama-Nakashita, Kazumi Nakabayashi, Weiqiang Li, Mikihiro Ogawa, Yukika Yamauchi, Jeremy Preston, Ko Aoki, et al. The atgenexpress hormone and chemical treatment data set: experimental design, data evaluation, model data analysis and data access. *The Plant Journal*, 55(3):526–542, 2008.

[95] Henrik Jönsson, Bruce E Shapiro, ELLIOT M Meyerowitz, and Eric Mjolsness. Signalling in multicellular models of plant development. *On growth, form and computers*, pages 156–161, 2003.

[96] Henrik Jönsson, Marcus Heisler, G Venugopala Reddy, Vikas Agrawal, Victoria Gor, Bruce E Shapiro, Eric Mjolsness, and Elliot M Meyerowitz. Modeling the organization of the wuschel expression domain in the shoot apical meristem. *Bioinformatics*, 21(suppl 1):i232–i240, 2005.

[97] Ulrike Brand, Margit Grünewald, Martin Hobe, and Rüdiger Simon. Regulation of clv3 expression by two homeobox genes in arabidopsis. *Plant physiology*, 129(2):565–575, 2002.

[98] Ildoo Hwang, Jen Sheen, and Bruno Müller. Cytokinin signalling networks. *Ann Rev. Plant Biol.*, 63:353–380, 2012.

[99] Patrick Laufs, Olivier Grandjean, Claudia Jonak, Kiên Kiêu, and Jan Traas. Cellular parameters of the shoot apical meristem in Arabidopsis. *Plant Cell*, 10:1375–1389, 1998.

[100] Gabor Daum, Anna Medzihradszky, Takuya Suzaki, and Jan U Lohmann. A mechanistic framework for noncell autonomous stem cell induction in arabidopsis. *Proceedings of the National Academy of Sciences*, 111(40):14619–14624, 2014.

[101] Ari Pekka Mähönen, Anthony Bishopp, Masayuki Higuchi, Kaisa M Nieminen, Kaori Kinoshita, Kirsi Törmäkangas, Yoshihisa Ikeda, Atsuhiro Oka, Tatsuo Kakimoto, and Ykä Helariutta. Cytokinin signaling and its inhibitor ahp6 regulate cell fate during vascular development. *Science*, 311(5757):94–98, 2006.

[102] Zhong Zhao, Stig U Andersen, Karin Ljung, Karel Dolezal, Andrej Miotk, Sebastian J Schultheiss, and Jan U Lohmann. Hormonal control of the shoot stem-cell niche. *Nature*, 465:1089–1092, 2010.

[103] P Graf, A Dolzblasz, and T Würschum. . . . MGOUN1 encodes an Arabidopsis type iB DNA topoisomerase required in stem cell regulation and to maintain developmentally regulated gene silencing. *Plant Cell*, 22:716–728, 2010.

[104] James D Murray. *Mathematical biology: I. An introduction*, volume 2. Springer, 2002.

[105] L Williams. Regulation of Arabidopsis shoot apical meristem and lateral organ formation by microRNA miR166g and its AtHD-ZIP target genes. *Development*, 132:3657–3668, 2005.

[106] Toru Kudo, Takatoshi Kiba, and Hitoshi Sakakibara. Metabolism and long-distance translocation of cytokinins. *J. of Integr. Plant Biol.*, 52:53–60, 2010.

[107] Joseph J Kieber and G Eric Schaller. Cytokinins. *The Arabidopsis book / American Society of Plant Biologists*, 12:e0168, 2014.

[108] Eric M Kramer, Nicholas L Frazer, and Tobias I Baskin. Measurement of diffusion within the cell wall in living roots of *Arabidopsis thaliana*. *J. Exp. Bot.*, 58:3005–3015, 2007.

[109] Anja Nenninger, Giulia Mastroianni, and Conrad W Mullineaux. Size dependence of protein diffusion in the cytoplasm of *Escherichia coli*. *J. Bacteriol*, 192:4535–4540, 2010.

[110] Tomasz Kalwarczyk, Marcin Tabaka, and Robert Holyst. Biologistics–diffusion coefficients for complete proteome of *Escherichia coli*. *Bioinformatics*, 28:2971–2978, 2012.

[111] Gong-Ke Zhou, Minoru Kubo, Ruiqin Zhong, Taku Demura, and Zheng-Hua Ye. Overexpression of mir165 affects apical meristem formation, organ polarity establishment and vascular development in arabidopsis. *Plant and Cell Physiology*, 48(3):391–404, 2007.

[112] Alicja Banasiak. Putative dual pathway of auxin transport in organogenesis of arabidopsis. *Planta*, 233(1):49–61, 2011.

[113] Kaare H Jensen, Kirstine Berg-Sørensen, Søren MM Friis, and Tomas Bohr. Analytic solutions and universal properties of sugar loading models in münch phloem flow. *Journal of theoretical biology*, 304:286–296, 2012.

[114] Hélène Bauby, Fanchon Divol, Elisabeth Truernit, Olivier Grandjean, and Jean-Christophe Palauqui. Protophloem differentiation in early arabidopsis thaliana development. *Plant and cell physiology*, 48(1):97–109, 2007.

[115] Fabrice Besnard, Frédérique Rozier, and Teva Vernoux. The ahp6 cytokinin signaling inhibitor mediates an auxin-cytokinin crosstalk that regulates the timing of organ initiation at the shoot apical meristem. *Plant signaling & behavior*, 9(6):e28788, 2014.

[116] Fabrice Besnard, Yassin Refahi, Valérie Morin, Benjamin Marteaux, Géraldine Brunoud, Pierre Chambrier, Frédérique Rozier, Vincent Mirabet, Jonathan Legrand, Stéphanie Lainé, et al. Cytokinin signalling inhibitory fields provide robustness to phyllotaxis. *Nature*, 505(7483):417–421, 2014.

[117] Annelie Carlsbecker, Ji-Young Lee, Christina J Roberts, Jan Dettmer, Satu Lehesranta, Jing Zhou, Ove Lindgren, Miguel A Moreno-Risueno, Anne Vatén, Siripong Thitamadee, et al. Cell signalling by microrna165/6 directs gene dose-dependent root cell fate. *Nature*, 465(7296):316–321, 2010.

[118] Jane R McConnell, John Emery, Yuval Eshed, Ning Bao, John Bowman, and M Kathryn Barton. Role of phabulosa and phavoluta in determining radial patterning in shoots. *Nature*, 411(6838):709–713, 2001.

[119] Leor Williams, Stephen P Grigg, Mingtang Xie, Sioux Christensen, and Jennifer C Fletcher. Regulation of arabidopsis shoot apical meristem and lateral organ formation by microrna mir166g and its athd-zip target genes. *Development*, 132(16):3657–3668, 2005.

[120] Tomáš Werner and Thomas Schmülling. Cytokinin action in plant development. *Current opinion in plant biology*, 12(5):527–538, 2009.

[121] Claire E Hutchison and Joseph J Kieber. Cytokinin signaling in arabidopsis. *The Plant Cell*, 14(suppl 1):S47–S59, 2002.

[122] Saiko Yoshida, Pierre Barbier de Reuille, Brendan Lane, George W Bassel, Przemyslaw Prusinkiewicz, Richard S Smith, and Dolf Weijers. Genetic control of plant development by overriding a geometric division rule. *Developmental cell*, 29(1):75–87, 2014.

[123] Anthony Bishopp, Hanna Help, Sedeer El-Showk, Dolf Weijers, Ben Scheres, Jiří Friml, Eva Benková, Ari Pekka Mähönen, and Ykä Helariutta. A mutually inhibitory interaction between auxin and cytokinin specifies vascular pattern in roots. *Current Biology*, 21(11):917–926, 2011.

[124] Bert De Rybel, Barbara Möller, Saiko Yoshida, Ilona Grabowicz, Pierre Barbier de Reuille, Sjef Boeren, Richard S Smith, Jan Willem Borst, and Dolf Weijers. A bhlh complex controls embryonic vascular tissue establishment and indeterminate growth in arabidopsis. *Developmental cell*, 24(4):426–437, 2013.

[125] Takeshi Kuroha, Hiroki Tokunaga, Mikiko Kojima, Nanae Ueda, Takashi Ishida, Shingo Nagawa, Hiroo Fukuda, Keiko Sugimoto, and Hitoshi Sakakibara. Functional analyses of lonely guy cytokinin-activating enzymes reveal the importance of the direct activation pathway in arabidopsis. *The Plant Cell Online*, 21(10):3152–3169, 2009.

[126] Takashi Kurakawa, Nanae Ueda, Masahiko Maekawa, Kaoru Kobayashi, Mikiko Kojima, Yasuo Nagato, Hitoshi Sakakibara, and Junko Kyozuka. Direct control of shoot meristem activity by a cytokinin-activating enzyme. *Nature*, 445(7128):652–655, 2007.

[127] Shunsuke Miyashima, Jose Sebastian, Ji-Young Lee, and Yka Helariutta. Stem cell function during plant vascular development. *The EMBO journal*, 32(2):178–193, 2013.

[128] Alexandra Schlereth, Barbara Möller, Weilin Liu, Marika Kientz, Jacky Flipse, Eike H Rademacher, Markus Schmid, Gerd Jürgens, and Dolf Weijers. Monopteros controls embryonic root initiation by regulating a mobile transcription factor. *Nature*, 464(7290):913–916, 2010.

[129] Hans-Michael Rupp, Markus Frank, Tomás Werner, Miroslav Strnad, and Thomas Schmülling. Increased steady state mrna levels of the stm and knat1 homeobox genes in cytokinin overproducing arabidopsis thaliana indicate a role for cytokinins in the shoot apical meristem. *The Plant Journal*, 18(5):557–563, 1999.

[130] Ari Pekka Mähönen, Martin Bonke, Leila Kauppinen, Marjukka Riikonen, Philip N Benfey, and Ykä Helariutta. A novel two-component hybrid molecule regulates vascular morphogenesis of the arabidopsis root. *Genes & development*, 14(23):2938–2943, 2000.

[131] Hiroki Tokunaga, Mikiko Kojima, Takeshi Kuroha, Takashi Ishida, Keiko Sugimoto, Takatoshi Kiba, and Hitoshi Sakakibara. Arabidopsis lonely guy (log) multiple mutants reveal a central role of the log-dependent pathway in cytokinin activation. *The Plant Journal*, 69(2):355–365, 2012.

[132] Kyoko Ohashi-Ito and Dominique C Bergmann. Regulation of the arabidopsis root vascular initial population by lonesome highway. *Development*, 134(16):2959–2968, 2007.

[133] Anthony Bishopp, Satu Lehesranta, Anne Vatén, Hanna Help, Sedeer El-Showk, Ben Scheres, Kerttuli Helariutta, Ari Pekka Mähönen, Hitoshi Sakakibara, and Ykä Helariutta. Phloem-transported cytokinin regulates polar auxin transport and maintains vascular pattern in the root meristem. *Current Biology*, 21(11):927–932, 2011.

[134] Daniele Muraro, Nathan Mellor, Michael P Pound, Mikaël Lucas, Jérôme Chopard, Helen M Byrne, Christophe Godin, T Charlie Hodgman, John R King, Tony P Pridmore, et al. Integration of hormonal signaling networks and mobile micrornas is required for vascular patterning in arabidopsis roots. *Proceedings of the National Academy of Sciences*, 111(2):857–862, 2014.

[135] Anthony Bishopp, Eva Benková, and Ykä Helariutta. Sending mixed messages: auxin-cytokinin crosstalk in roots. *Current opinion in plant biology*, 14(1):10–16, 2011.

[136] Peter Marhav ỳ, Agnieszka Bielach, Lindy Abas, Anas Abuzeineh, Jerome Duclercq, Hirokazu Tanaka, Markéta Pařezová, Jan Petrášek, Jiří Friml, Jürgen Kleine-Vehn, et al. Cytokinin modulates endocytic trafficking of pin1 auxin efflux carrier to control plant organogenesis. *Developmental cell*, 21(4):796–804, 2011.

[137] Jiří Friml, Anne Vieten, Michael Sauer, Dolf Weijers, Heinz Schwarz, Thorsten Hamann, Remko Offringa, and Gerd Jürgens. Efflux-dependent auxin gradients establish the apical–basal axis of arabidopsis. *Nature*, 426(6963):147–153, 2003.

[138] Bert De Rybel, Alice S Breda, and Dolf Weijers. Prenatal plumbing—vascular tissue formation in the plant embryo. *Physiologia plantarum*, 151(2):126–133, 2014.

[139] Ben Scheres, Laura Di Laurenzio, Viola Willemsen, Marie-Therès Hauser, Kees Janmaat, Peter Weisbeek, and Philip N Benfey. Mutations affecting the radial organisation of the arabidopsis root display specific defects throughout the embryonic axis. *Development*, 121(1):53–62, 1995.

[140] Didier Reinhardt, Eva-Rachele Pesce, Pia Stieger, Therese Mandel, Kurt Baltensperger, Malcolm Bennett, Jan Traas, Jiří Friml, and Cris Kuhlemeier. Regulation of phyllotaxis by polar auxin transport. *Nature*, 426(6964):255–260, 2003.

[141] Hanna Help, Ari Pekka Mähönen, Ykä Helariutta, and Anthony Bishopp. Bisymmetry in the embryonic root is dependent on cotyledon number and position. *Plant signaling & behavior*, 6(11):1837–1840, 2011.

[142] Clive W Lloyd. How does the cytoskeleton read the laws of geometry in aligning the division plane of plant cells? *Development*, 113(Supplement 1):55–65, 1991.

[143] Christian S Hardtke and Thomas Berleth. The arabidopsis gene monopteros encodes a transcription factor mediating embryo axis formation and vascular development. *The EMBO journal*, 17(5):1405–1411, 1998.

[144] William H Press. *Numerical recipes 3rd edition: The art of scientific computing*. Cambridge university press, 2007.

[145] Michael D McKay, Richard J Beckman, and William J Conover. Comparison of three methods for selecting values of input variables in the analysis of output from a computer code. *Technometrics*, 21(2):239–245, 1979.

[146] F Skoog and CO Miller. *Chemical regulation of growth and organ formation in plant tissues cultured in vitro.*, volume 11. In vitro. Symp. Soc. Exp. Biol., 1957.

[147] Eva Benková, Marta Michniewicz, Michael Sauer, Thomas Teichmann, Daniela Seifertová, Gerd Jürgens, and Jiří Friml. Local, efflux-dependent auxin gradients as a common module for plant organ formation. *Cell*, 115(5):591–602, 2003.

[148] Alexandria Saulsberry, Paula R Martin, Tim O'Brien, Leslie E Sieburth, and F Bryan Pickett. The induced sector arabidopsis apical embryonic fate map. *Development*, 129(14):3403–3410, 2002.

[149] Hirofumi Katayama, Kuninori Iwamoto, Yuka Kariya, Tomohiro Asakawa, Toshiyuki Kan, Hiroo Fukuda, and Kyoko Ohashi-Ito. A negative feedback loop controlling bhlh complexes is involved in vascular cell division and differentiation in the root apical meristem. *Current Biology*, 25(23):3144–3150, 2015.

[150] Kamil ů žička, Mária Šimášková, Jerome Duclercq, Jan Petrášek, Eva Zažímalová, Sibu Simon, Jiří Friml, Marc CE Van Montagu, and Eva Benková. Cytokinin regulates root meristem activity via modulation of the polar auxin transport. *Proceedings of the National Academy of Sciences*, 106(11):4284–4289, 2009.

[151] Marketa Pernisova, Tomas Prat, Peter Grones, Danka Harustiakova, Martina Matonohova, Lukas Spichal, Tomasz Nodzynski, Jiri Friml, and Jan Hejatko. Cytokinins influence root gravitropism via differential regulation of auxin transporter expression and localization in arabidopsis. *New Phytologist*, 2016.

[152] Peter Marhavỳ, Jérôme Duclercq, Benjamin Weller, Elena Feraru, Agnieszka Bielach, Remko Offringa, Jiří Friml, Claus Schwechheimer, Angus Murphy, and Eva Benková. Cytokinin controls polarity of pin1-dependent auxin transport during lateral root organogenesis. *Current Biology*, 24(9):1031–1037, 2014.

[153] Hongchang Cui, Mitchell P Levesque, Teva Vernoux, Jee W Jung, Alice J Paquette, Kimberly L Gallagher, Jean Y Wang, Ikram Blilou, Ben Scheres, and Philip N Benfey. An evolutionarily conserved mechanism delimiting shr movement defines a single layer of endodermis in plants. *Science*, 316(5823):421–425, 2007.

[154] Ranjan Swarup, Eric M Kramer, Paula Perry, Kirsten Knox, HM Ottoline Leyser, Jim Haseloff, Gerrit TS Beemster, Rishikesh Bhalerao, and Malcolm J Bennett. Root gravitropism requires lateral root cap and epidermal cells for transport and response to a mobile auxin signal. *Nature cell biology*, 7(11):1057–1065, 2005.

[155] Verônica A Grieneisen, Jian Xu, Athanasius FM Marée, Paulien Hogeweg, and Ben Scheres. Auxin transport is sufficient to generate a maximum and gradient guiding root growth. *Nature*, 449(7165):1008–1013, 2007.

[156] Victoria V Mironova, Nadezda A Omelyanchuk, Guy Yosiphon, Stanislav I Fadeev, Nikolai A Kolchanov, Eric Mjolsness, and Vitaly A Likhoshvai. A plausible mechanism for auxin patterning along the developing root. *BMC Systems Biology*, 4(1):1, 2010.

[157] Leah R Band, Darren M Wells, John A Fozard, Teodor Ghetiu, Andrew P French, Michael P Pound, Michael H Wilson, Lei Yu, Wenda Li, Hussein I Hijazi, et al. Systems analysis of auxin transport in the arabidopsis root apex. *The Plant Cell*, 26(3):862–875, 2014.

[158] Géraldine Brunoud, Darren M Wells, Marina Oliva, Antoine Larrieu, Vincent Mirabet, Amy H Burrow, Tom Beeckman, Stefan Kepinski, Jan Traas, Malcolm J Bennett, et al. A novel sensor to map auxin response and distribution at high spatio-temporal resolution. *Nature*, 482(7383):103–106, 2012.

[159] Benjamin Péret, Alistair M Middleton, Andrew P French, Antoine Larrieu, Anthony Bishopp, Maria Njo, Darren M Wells, Silvana Porco, Nathan Mellor, Leah R Band, et al.

Sequential induction of auxin efflux and influx carriers regulates lateral root emergence. *Molecular systems biology*, 9(1):699, 2013.

[160] Daniele Muraro, Helen Byrne, John King, and Malcolm Bennett. The role of auxin and cytokinin signalling in specifying the root architecture of arabidopsis thaliana. *Journal of theoretical biology*, 317:71–86, 2013.

[161] Daniele Muraro, Helen Byrne, John King, Ute Voß, Joseph Kieber, and Malcolm Bennett. The influence of cytokinin–auxin cross-regulation on cell-fate determination in arabidopsis thaliana root development. *Journal of theoretical biology*, 283(1):152–167, 2011.

[162] Sedeer el Showk, Tiina Blomster, Riccardo Siligato, Athanasius FM Marée, Ari Pekka Mähönen, Verônica A Grieneisen, et al. Parsimonious model of vascular patterning links transverse hormone fluxes to lateral root initiation: Auxin leads the way, while cytokinin levels out. *PLoS Comput Biol*, 11(10):e1004450, 2015.

[163] Christophe Pradal, Samuel Dufour-Kowalski, Frédéric Boudon, Christian Fournier, and Christophe Godin. Openalea: a visual programming and component-based software platform for plant modelling. *Functional plant biology*, 35(10):751–760, 2008.

[164] Marta Laskowski, Verônica A Grieneisen, Hugo Hofhuis, A Colette, Paulien Hogeweg, Athanasius FM Marée, and Ben Scheres. Root system architecture from coupling cell shape to auxin transport. *PLoS Biol*, 6(12):e307, 2008.

[165] Przemyslaw Prusinkiewicz and Adam Runions. Computational models of plant development and form. *New Phytologist*, 193(3):549–569, 2012.

[166] P Van Liedekerke, MM Palm, N Jagiella, and D Drasdo. Simulating tissue mechanics with agent-based models: concepts, perspectives and some novel results. *Computational Particle Mechanics*, 2(4):401–444, 2015.

[167] Julien Lavenus, Tatsuaki Goh, Ianto Roberts, Soazig Guyomarc'h, Mikael Lucas, Ive De Smet, Hidehiro Fukaki, Tom Beeckman, Malcolm Bennett, and Laurent Laplaze. Lateral root development in arabidopsis: fifty shades of auxin. *Trends in Plant Science*, 18(8):450–458, 2013.

[168] Hélène S Robert and Jiří Friml. Auxin and other signals on the move in plants. *Nature Chemical Biology*, 5(5):325–332, 2009.

[169] John Gutknecht and Anne Walter. Transport of auxin (indoleacetic acid) through lipid bilayer membranes. *The Journal of membrane biology*, 56(1):65–72, 1980.

[170] Shigeru Kondo. The reaction-diffusion system: a mechanism for autonomous pattern formation in the animal skin. *Genes to Cells*, 7(6):535–541, 2002.

[171] Shigeru Kondo and Rihito Asai. A reaction-diffusion wave on the skin of the marine angelfish pomacanthus. *Nature*, 376(6543):765–768, 1995.

[172] Jonathan BL Bard. A model for generating aspects of zebra and other mammalian coat patterns. *Journal of Theoretical Biology*, 93(2):363–385, 1981.

[173] Amarendra Badugu, Conradin Kraemer, Philipp Germann, Denis Menshykau, and Dagmar Iber. Digit patterning during limb development as a result of the bmp-receptor interaction. *Scientific reports*, 2, 2012.

[174] Julien Lefèvre and Jean-François Mangin. A reaction-diffusion model of the human brain development. In *Biomedical Imaging: From Nano to Macro, 2010 IEEE International Symposium on*, pages 77–80. IEEE, 2010.

[175] Bruno Müller and Jen Sheen. Cytokinin and auxin interaction in root stem-cell specification during early embryogenesis. *Nature*, 453(7198):1094–1097, 2008.

[176] Olivier Grandjean, Teva Vernoux, Patrick Laufs, Katia Belcram, Yuki Mizukami, and Jan Traas. In vivo analysis of cell division, cell growth, and differentiation at the shoot apical meristem in arabidopsis. *The Plant Cell Online*, 16(1):74–87, 2004.

[177] Daniel Kierzkowski, Naomi Nakayama, Anne-Lise Routier-Kierzkowska, Alain Weber, Emmanuelle Bayer, Martine Schorderet, Didier Reinhardt, Cris Kuhlemeier, and Richard S Smith. Elastic domains regulate growth and organogenesis in the plant shoot apical meristem. *Science Signaling*, 335(6072):1096–1099, 2012.

[178] Bert De Rybel, Willy van den Berg, Annemarie S Lokerse, Che-Yang Liao, Hilda van Mourik, Barbara Möller, Cristina I Llavata-Peris, and Dolf Weijers. A versatile set of ligation-independent cloning vectors for functional studies in plants. *Plant physiology*, 156(3):1292–1299, 2011.

[179] Cristina Llavata-Peris, Annemarie Lokerse, Barbara Möller, Bert De Rybel, and Dolf Weijers. Imaging of phenotypes, gene expression, and protein localization during embryonic root formation in arabidopsis. In *Plant Organogenesis*, pages 137–148. Springer, 2013.

[180] Ive De Smet, Peter Chaerle, Steffen Vanneste, Riet De Rycke, Dirk Inzé, and Tom Beeckman. An easy and versatile embedding method for transverse sections. *Journal of microscopy*, 213(1):76–80, 2004.

[181] Elisabeth Truernit, Hélène Bauby, Bertrand Dubreucq, Olivier Grandjean, John Runions, Julien Barthélémy, and Jean-Christophe Palauqui. High-resolution whole-mount imaging of three-dimensional tissue organization and gene expression enables the study of phloem development and structure in arabidopsis. *The Plant Cell Online*, 20(6):1494–1503, 2008.

[182] Jana Svačinová, Ondřej Novák, Lenka Plačková, René Lenobel, Josef Holík, Miroslav Strnad, and Karel Doležal. A new approach for cytokinin isolation from arabidopsis

tissues using miniaturized purification: pipette tip solid-phase extraction. *Plant methods*, 8(1):17, 2012.

[183] Klára Hoyerová, Alena Gaudinová, Jiří Malbeck, Petre I Dobrev, Tomáš Kocábek, Blanka Šolcová, Alena Trávníčková, and Miroslav Kamínek. Efficiency of different methods of extraction and purification of cytokinins. *Phytochemistry*, 67(11):1151–1159, 2006.

[184] Petre Ivanov Dobrev and Miroslav Kamínek. Fast and efficient separation of cytokinins from auxin and abscisic acid and their purification using mixed-mode solid-phase extraction. *Journal of Chromatography A*, 950(1):21–29, 2002.

[185] Nobutoshi Yamaguchi, Cara M Winter, Miin-Feng Wu, Chang Seob Kwon, Dilusha A William, and Doris Wagner. Protocols: Chromatin immunoprecipitation from arabidopsis tissues. *The Arabidopsis book/American Society of Plant Biologists*, 12, 2014.

[186] Jan Hellemans, Geert Mortier, Anne De Paepe, Frank Speleman, and Jo Vandesompele. qbase relative quantification framework and software for management and automated analysis of real-time quantitative pcr data. *Genome biology*, 8(2):R19, 2007.

[187] Siobhan M Brady, David A Orlando, Ji-Young Lee, Jean Y Wang, Jeremy Koch, José R Dinneny, Daniel Mace, Uwe Ohler, and Philip N Benfey. A high-resolution root spatiotemporal map reveals dominant expression patterns. *Science*, 318(5851):801–806, 2007.

[188] Ke Lin, Harrie Kools, Philip J de Groot, Anand K Gavai, Ram K Basnet, Feng Cheng, Jian Wu, Xiaowu Wang, Arjen Lommen, GJ Hooiveld, et al. Madmax-management and analysis database for multiple omics experiments. *J Integr Bioinform*, 8(2):160, 2011.

[189] Benjamin M Bolstad, Rafael A Irizarry, Magnus Åstrand, and Terence P. Speed. A comparison of normalization methods for high density oligonucleotide array data based on variance and bias. *Bioinformatics*, 19(2):185–193, 2003.

[190] Rafael A Irizarry, Benjamin M Bolstad, Francois Collin, Leslie M Cope, Bridget Hobbs, and Terence P Speed. Summaries of affymetrix genechip probe level data. *Nucleic acids research*, 31(4):e15–e15, 2003.

[191] Manhong Dai, Pinglang Wang, Andrew D Boyd, Georgi Kostov, Brian Athey, Edward G Jones, William E Bunney, Richard M Myers, Terry P Speed, Huda Akil, et al. Evolving gene/transcript definitions significantly alter the interpretation of genechip data. *Nucleic acids research*, 33(20):e175–e175, 2005.

[192] Maureen A Sartor, Craig R Tomlinson, Scott C Wesselkamper, Siva Sivaganesan, George D Leikauf, and Mario Medvedovic. Intensity-based hierarchical bayes method improves testing for differentially expressed genes in microarray experiments. *BMC bioinformatics*, 7(1):538, 2006.

[193] John D Storey and Robert Tibshirani. Statistical significance for genomewide studies. *Proceedings of the National Academy of Sciences*, 100(16):9440–9445, 2003.

ACKNOWLEDGEMENTS

I would like to thank my PhD supervisor, dr. Christian Fleck, for his support for my PhD studies. His extensive knowledge and meticulous approach to theoretical research has had a lasting effect on me as a researcher. I would also like to thank Prof. dr. Vitor Dos Santos, he provided me with a welcoming and motivating environment in Wageningen and without his help completion of this thesis would have been impossible.

I would like to thank my colleague and fellow PhD student, Michael Volpers, who greatly helped me in both research and with settling in Germany. Without his help settling in Germany, with my limited knowledge of German, would have been a daunting task. I would like to thank my colleague and friend dr. Filippo Venezia for his help and good memories from our friendship in Freiburg.

My sincere thanks goes to prof. dr. Dolf Weijers, dr. Bert DeRybel and dr. Saiko Yoshida, my experimental collaborators in Wageningen university. Having the opportunity to work with them was a key to the success of my PhD and it showed me how fun and productive a research collaboration can be. Dolf and Bert, I will never forget our enjoyable discussion and the great impact you have had on my career as a researcher. Saiko, your skill, dedication and hard work has set up an example for me on how to be a successful researcher, and working together with you in the confocal room was the most enjoyable part of my PhD studies.

My thanks goes to members of Fleck and Lebeidz research groups, at ZBSA in Freiburg, many of whom were friends as well as colleges; Bettina Greese, Joe Hamsted, Marcel Rehberg, Jochen Siehr, Dominik Skanda, Marc Fein, Junas Ungar, Allister Middleton, Phillip Best and others. I would like to thank people that I shared a house with during my stay in Freiburg; Maximillian Traber, Collin Schmitchen and Konrad Feldmeier. You guys were kind and friendly house mates and I couldn't have managed my affairs in Germany without your help. Special thanks to my lovely neighbors Sarah and Ilka, I have not had neighbors as nice as you guys before or ever since! I would also like to thank Benoit Carreres, Bastian Hornung (aka Sea Bass), Theresita Gonzales, Robert Smith, Dorett Odoni, Ruben van Heck, Marteen Reijnders, Niels Zondervan, Javier Ramiro-Garcia, Siavash Atashgahi, Kal Subramanian, Rico Hagelaar, Nikolas Strepis, Jasper Koeherst, Mark Davids and others. These were my friends and colleagues in Systems and synthetic biology laboratory and Microbiology department at Wageningen university. I miss our fun coffee breaks, the friendly and welcoming atmosphere and all the memorable time we spent together.

I like to extend my thanks to others who were a part of my life during my PhD studies, Stephen, Reiner, Simon, Michael, Rafael, Marin, Kun and others for the wonderful times we shared.

Last but not least, I would like to thank my family, words cannot express how grateful I am to my father, mother and brother, for all the sacrifices you have made on my behalf. All the

support they have give me is the greatest gift I have ever received and I owe to them all that I have achieved in my studies, and life in general.

About the author

Milad Adibi was born on February 19th in Tehran, Iran. In 2006 he completed his bachelor's degree in Biotechnology at the University of Nottingham, Nottingham-UK. In 2007 he obtained his Master's degree in Integrative Biology from the same university. Afterwards he moved back to Tehran and worked at the Pasteur Institute of Iran as a scientific employee. In autumn of 2009 he started his PhD degree at the university of Freiburg, in the group of prof. dr. Jens Timmer, under the supervision dr. Christian Fleck. During this time he studied mechanism of spatial pattern formation in plant morphogenesis, with a focus on Turing reaction-diffusion systems. In 2013, together with dr. Fleck's research group, he relocated to the Laboratory of systems and synthetic biology in Wageningen university. In 2015 he started his PhD at the laboratory of systems and synthetic biology at Wageningen university. As a PhD students he has been involved in interdisciplinary collaborations aimed at studying spatial and temporal coordination of plant developmental processes, specifically during early plant embryogenesis.

Publications

Bert De Rybel*, **Milad Adibi***, Alice S Breda, Jos R Wendrich, Margot E Smit, Ondřej Novák, Nobutoshi Yamaguchi, Saiko Yoshida, Gert Van Isterdael, Joakim Palovaara, et al. Integration of growth and patterning during vascular tissue formation in arabidopsis. Science, 345(6197):1255215, 2014.

Nathan Mellor*,**Milad Adibi***, Sedeer El-Showk, Bert De Rybel, John King, Ari Pekka Mähönen, Dolf Weijers, and Anthony Bishopp. Theoretical approaches to understanding root vascular patterning: a consensus between recent models. Journal of Experimental Botany 68(1):5-16, 2017

Milad Adibi, Saiko Yoshida, Dolf Weijers and Christian Fleck. Centering the organizing center in the Arabidopsis thaliana shoot apical meristem by a combination of cytokinin signaling and self-organization. PloS one, 11(2):e0147830, 2016.

* equal contribution

The research decribed in this thesis was financially supported by LifeGlimmer GmbH.

Financial support from Wageningen University, the laboratory of systems and synthetic biology for printing this thesis is gratefully acknowledged.